Stony Brook University

Observation of ν_e appearance from an off-axis ν_μ beam utilizing the neutrino energy spectrum

A Dissertation Presented

by

Joshua Hignight

to

The Graduate School

in Partial Fulfillment of the Requirements

for the Degree of

Doctor of Philosophy

in

Physics

Stony Brook University

May 2014

Stony Brook University

The Graduate School

Joshua Hignight

We, the dissertation committee for the above candidate for the Doctor of Philosophy degree, hereby recommend acceptance of this dissertation.

Chang Kee Jung – Dissertation Advisor
Professor, Department of Physics and Astronomy

Alan C. Calder – Chairperson of Defense
Professor, Department of Physics and Astronomy

Dmitri Tsybychev
Professor, Department of Physics and Astronomy

Brett Viren
Physicist, Brookhaven National Laboratory

This dissertation is accepted by the Graduate School.

Charles Taber
Dean of the Graduate School

Abstract of the Dissertation

Observation of ν_e appearance from an off-axis ν_μ beam utilizing the neutrino energy spectrum

by

Joshua Hignight

Doctor of Philosophy

in

Physics

Stony Brook University

2014

T2K (Tokai to Kamiokande) is a long baseline neutrino experiment located in Japan. It uses a 30 GeV proton beam at the J-PARC accelerator in Tokai to produce an intense off-axis muon neutrino beam that travels 295 km through the Earth to Super-Kamiokande. One of its primary goals is to measure neutrino oscillation parameters by directly detecting ν_e at Super-Kamiokande that have oscillated from the ν_μ beam. The measurement of $\nu_\mu \rightarrow \nu_e$ oscillations are of a particular interest because this mode is sensitive to both mixing angle θ_{13} and CP phase δ_{CP} of the PMNS matrix. Precise measurement of $\nu_\mu \rightarrow \nu_e$ allows us to explore the possibility of CP violation in the lepton sector.

This dissertation will describe the recent 2013 ν_e appearance oscillation analysis using the reconstructed neutrino energy spectrum by means of a maximum likelihood fit. The data used for this analysis corresponds to 6.57×10^{20} POT. A total of 28 ν_e candidate

events were observed, corresponding to a 7.2 σ significance of ν_e appearance by non-zero θ_{13}. These results are then combined with the world average value of θ_{13} from reactor experiments and some values of δ_{CP} are disfavored at the 90% CL.

I dedicate this dissertation to my loving wife, Dr. Karin Gilje, without whom I could have never finished. Her patience, help, and love during this process was beyond reproach.

Contents

List of Figures

List of Tables

List of Abbreviations

AGS	Alternating Gradient Synchrotron
BANFF	Beam And Neutrino Flux task Force
BNL	Brookhaven National Laboratory
CCQE	Charged Current Quasi Elastic
CP	Charge Parity
ECal	Electromagnetic Calorimeter
FGD	Fine Grained Detector
FPN	Front-end Processing Node
OD	Inner Detector
INGRID	Interactive Neutrino GRID
J-PARC	Japan Proton Accelerator Research Complex
MC	Monte Carlo
MIDAS	Maximum Integrated Data Acquisition System
MPPC	Multi-Pixel Photon Counter
NC	Neutral Current
ND280	The near detector complex at 280 m from the target
ND280	The off-axis near detector at T2K
PDF	Probability Distribution Function
PE	Photo-Electron
PID	Particle IDentification
PMT	PhotoMultiplier Tube
POT	Protons on Target
PØD	π^0 detector
OD	Outer Detector
SK	Super Kamiokande
SMRD	Side Muon Range Detector
T2K	A long-baseline neutrino oscillation experiment
TFB	TripT Front End Board
TPC	Time Projection Chamber

Acknowledgements

There are so many people who have helped me throughout my life and career that the list is far too long to mention everyone. I will, however, try to highlight as many people as I can remember and I thought deserved special mention. Inevitably, I will forget someone, and if you are that person, I deeply apologize.

I would like to start by thanking my family. It is needless to say that without my parents none of this would be possible. There is no way to put in words the amount of love and help they have given me through the years. My sister, her husband, and their two adorable children have also given me great joy and encouragement throughout my academic career.

Thanks to the schools and teachers I have had over the years for shaping me into what I have become. Mr. Shawness for showing me even a special-ed kid can succeed and Mrs. Anderson for first introducing me into real science, thank you. Special thanks should go to Dr. Carlos Spaht for starting the LaPREP program at LSU-S, which has helped hundreds of middle-schoolers become interested in and prepared for STEM fields. I would also like to thank the Louisiana School for the Math, Science, and Arts which over-prepared me for an academic career and taught me valuable life lessons.

Thank you to all my friends during the years for all the fun and help you have provided me. Whitney, Matt, T.B., Dr. Lee Sawyer, and so many others helped me make it through high-school and college and remain relatively sane. Paul, David, Cip, Betul, Shawn, and the entire game night crew have also helped keep my sanity during graduate school.

This entire thesis would not be possible without the help from everyone on both the T2K and SuperK experiments. Thanks to the those that helped design, build, and run both experiments and the US Department of Energy whose funding allowed me to work on them. Shiozawa-san, Nakayama-san, Nishimura-san, Mine-san, Nakaya-san, Ichikawa-san, Hiro, Kendall, Roger, Chris, and Okumura-san have all particularly helped with my analysis work and helped me become established at both SuperK and T2K. Josh, Taritree, Roger, Giada, Trk, Thomas, Jeff, Mike, Lili, Kai, Jim, and Mine-san always gave me a reason to want to visit Japan and have provided hours of fun at the

office (or local izakayas).

Thanks to the NNGROUP at Stony Brook where I have meet so many friends and colleagues. James, Ian, Jeanine, Jay, and Xiaoyue have all become good friends. Special thanks goes to Dr. Chang Kee Jung who gave me a chance to join the group and guided me throughout my graduate career. He always gave me enough room to find my own working style and the encouragement (pressure) to finish it.

Finally, I thank my wife, Karin Gilje. She has done so much for me and brought so much joy to me over the last few years. Without her help, encouragement, and love I could have never finished.

Chapter 1

Introduction

1.1 Dissertation Outline

In Chapter 2, I attempt to familiarize the reader with the basic components needed to understand the rest of the dissertation. This includes deriving neutrino oscillation probabilities, reviewing basic neutrino interactions, and discussing the still open questions in neutrino physics. Chapter 3 and Chapter 4 go over the experimental setup and explains the T2K experiment from the production of the neutrino beam to their detection at Super-Kamiokande. None of these chapters are meant to provide in-depth explanations but more of an overview for those not familiar with T2K.

Chapter 5 begins the discussion of the $\nu_\mu \rightarrow \nu_e$ appearance analysis this dissertation is based on. It goes over the inputs and likelihood method used. The systematic error calculations are presented in Chapter 6. The analysis software validation and expected sensitivities are shown in Chapter 7 and Chapter 8, receptively. Finally, the results from the fit and a constraint on CP violation in the lepton sector are presented in Chapter 9 and Chapter 10.

1.2 Author's Contributions

In large collaborations it is often difficult to know who worked on what. It is safe to say that this analysis would not be possible without the contributions from everyone in the collaboration. I feel that it is still important to outline what parts I did and did not work on directly. Apart from actively taking shifts and the general editing of publications, my contributions are listed below.

In my first year at Stony Brook, 2008, I helped build the PØD detector. In the summer of 2009, I helped with the installation of the PØD into the ND280 pit. After finishing classes, I started working at Super-K in 2010.

Since that time, I have worked extensively with the energy-scale calibration (see Section 4.5 for more details.) More specifically, I worked on improvements to the sub-GeV stopping muon sample which is currently the largest error for the energy-scale. I also made all the Monte Carlo (MC) used for the energy scale calculations and edited the MC simulation so all samples can use the same input format.

For T2K, I wrote and automated most of the reduction code for the T2K data gathered at Super-K . This included writing the code to have the reduction done in real time and running daily data quality checks. A web-page was made where reduction shifts could be performed anywhere in the world, allowing for more people to help with reduction checks and reducing the time needed to uncover problems. I also made the official data files used by the oscillation analyzers and most of the official plots that pertain to T2K events at the far detector.

The final part done directly by me was the $\nu_\mu \rightarrow \nu_e$ appearance analysis, and is the primary purpose of this dissertation. The analysis is based on a blind analysis done previously and is often referred to as 2012a results in this dissertation (see [1] for a detailed description and results.) As this is a continuation of a previous analysis, I did not write all of the fitting code myself. I performed many updates to the code to make the analysis compatible with the new data set and new systematic inputs along with extensive validation and sensitivity checks with the fitter. Of the 49 systematic errors used in the analysis, I only directly measured one, the energy-scale correction. All the other systematic error calculations and flux inputs where provided to me by other working groups. However, all the code for measuring δ_{CP} was developed by me as well as the entire data analysis (including the fitting of data, making of plots, documentation and presentations). Because of this, I was also one of five primary authors for T2K's most recent $\nu_\mu \rightarrow \nu_e$ appearance results paper published in PRL [2]. My duties for the aforementioned paper included writing the Super-K section, making plots for the paper, and general editing of the other sections. Finally, it should be noted that because many parts were done by a plethora of people, I cite many internal T2K documents for reference. If a reference could be found in a published paper, however, I tried to cite that instead. For those without a published reference, sufficient information was attempted to be given that the citation is only really needed for completeness.

Chapter 2

A Brief Overview of Neutrino Physics

2.1 A Brief History of Neutrino Oscillations

Neutrinos were first postulated to explain how β-decay could conserve energy, momentum, and spin. Unlike the discrete spectrum of alpha and gamma emissions, the spectrum of β-decay is continuous and broad. In December of 1930, Wolfgang Pauli wrote his infamous "Dear Radioactive Ladies and Gentlemen" letter where he proposed a massless, neutral, spin 1/2 particle that would later come to be known as the neutrino [3]. Though widely criticized by others at the time, Pauli was eventually proven correct. It took over two decades after first being postulated, but Fredrick Reines and Clyde Cowan found preliminary evidence for anti-neutrinos in 1953 [4] and more compelling evidence in 1956 outside the Savannah River nuclear power plant [5].

Over the next few decades, many new neutrino experiments came to pass, most with surprising results. Shortly after the discovery of anti-neutrinos through inverse β-decay, Bruno Pontecorvo proposed an experiment that would detect solar neutrinos [6]. In the 1960's, Ray Davis began one of the most famous neutrino experiments based on Pontecorvo's proposal [7]. He measured a large deficit in the expected number of neutrinos coming from the sun. Shortly after these results where published, Pontecorvo postulated a solution to the problem. As Davis's experiment could only detect electron neutrinos, if neutrinos could oscillate between ν_e and ν_μ (the only two kinds of neutrinos known at that time) it could help explain away the deficit. It would be many years before this theory could be tested and most believed in alternative explanations for the deficit, such as experimental error and errors on the solar neutrino model.

Direct evidence for neutrino oscillations came in 1998 when the Super-Kamiokande experiment released their results on atmospheric neutrinos [8]. They saw a deficit in ν_μ that where coming up through the Earth but not in those coming down. This deficit was only seen in the ν_μ sample, however, as the ν_e sample was the same in both the up going and down going sample. The results where consistent with $\nu_\mu \rightarrow \nu_\tau$ oscillations and showed the first direct evidence of neutrino oscillations. These where of atmospheric neutrino's, however, so the solar neutrino problem still remained.

It was just four years before the Sudbury Neutrino Observatory (SNO) announced they had found direct evidence for solar neutrino oscillations [9]. They did this by looking at charged current interactions (which only ν_e could undergo in their detector) and elastic scattering/neutral current interactions (which all neutrino flavors participate in.) With this they could deduce that all the missing ν_e had oscillated to either ν_μ or ν_τ. The solar neutrino problem was solved and neutrino oscillations were here to stay.

The discovery of neutrino oscillations is an important part of particle physics because it is the first confirmation of physics beyond the standard model, in which neutrinos are considered massless. Neutrino oscillations occur because the neutrino flavor eigenstates (electron, muon, and tau) are not the same as the mass eigenstates (usually labeled 1, 2, and 3.) As we will see in the next section, neutrino oscillations can only occur if neutrinos have mass.

2.2 Theory of Neutrino Oscillations

2.2.1 Two Flavor Neutrino Mixing in a Vacuum

To better understand how neutrino oscillations occur in a vacuum, it is advantageous to look at the simplified version with mixing between only two flavors. Here, states labeled with a numerical subscript will represent our mass eigenstates while those in greek subscript will represent our flavor eigenstates. The two flavor solution uses a simple unitary mixing matrix to relate the flavor eigenstates to the mass eigenstates by

$$\begin{pmatrix} \nu_\alpha \\ \nu_\beta \end{pmatrix} = \begin{pmatrix} \cos\theta & \sin\theta \\ -\sin\theta & \cos\theta \end{pmatrix} \begin{pmatrix} \nu_1 \\ \nu_2 \end{pmatrix} \tag{2.1}$$

The mass states are just eigenstates for the plane wave solution to the Schrödinger equation and each mass state propagates at a different speed. If we let the states evolve over time in a vacuum, we get the well known solution for a plane wave

$$|\nu_j(\overrightarrow{x},t)\rangle = e^{-i(E_j t - \overrightarrow{p_j}\overrightarrow{x})/\hbar}|\nu_j(0)\rangle \tag{2.2}$$

With this solution, we can calculate the probability of a neutrino in one flavor state oscillating into a another flavor state as:

$$P(\nu_\alpha \to \nu_\beta) = |\,\langle\nu_\beta(t)|\nu_\alpha(0)\rangle\,|^2 \tag{2.3}$$

This means the probability is just the square of the matrix element of the pure flavor eigenstate with the propagated state of the initial flavor state. If we use the information that neutrinos are almost massless, we can assume $p >> m$ leading to:

$$E_j = \sqrt{m_j^2 + p_j^2} = p_j\sqrt{1 + \frac{m_j^2}{p_j^2}} \approx p_j + \frac{m_j^2}{2p_j} \tag{2.4}$$

We can also make more simplifications by defining $t = L/v$, where $v \approx c$, and $p \approx E$. If we plug these substitutions into Equation 2.2, we have:

$$|\nu_j(\overrightarrow{x},t)\rangle = e^{-i\frac{m_j^2}{2}\frac{L}{E}}|\nu_j(0)\rangle \tag{2.5}$$

Plugging this into Equation 2.3, using the orthogonality of the flavor states, and converting to more the more useful units of eV and km, we find that

$$P(\nu_\alpha \to \nu_\beta) = \sin^2 2\theta \sin^2\left(\frac{1.27\Delta m^2 L[km]}{E[eV]}\right) \tag{2.6}$$

Here we have introduced a common short hand $\Delta m^2 = m_2^2 - m_1^2$ and is called the mass splitting. Equation 2.6 has several important factors to be pointed out that also hold true when we move to the three flavor case. First, we can see that the amplitude of the oscillation is controlled by the mixing angle θ. When $\theta = \pi/4$, there is maximal mixing between the two flavor states while when $\theta = 0$ there is no mixing. Another thing to notice is that the frequency of the oscillations is controlled by both the mass splitting of the two neutrinos and the L/E. This means for a certain mass splitting, the length of oscillation and energy of the neutrino can be tuned to change the oscillation frequency to best suit the experiment.

2.2.2 Three Flavor Mixing

It is fairly trivial, though much more algebraically intense, to extend this simple two-flavor neutrino model into a three flavor neutrino model. This is done by combing three Euler angles and a phase to make a 3×3 unitary matrix.

If neutrinos are Majorana particles, that is they are their own antiparticles, an extra Majorana phase must also be added. This extra phase shift only occurs in diagonal terms, however, and it can be shown that such on-diagonal phase shifts do not effect neutrino oscillations. This means it is impossible to figure out if a neutrino is a Dirac or Majorana particle simply by looking at oscillations.

$$\begin{pmatrix}\nu_e\\ \nu_\mu\\ \nu_\tau\end{pmatrix} = \begin{pmatrix}1 & 0 & 0\\ 0 & c_{23} & s_{23}\\ 0 & -s_{23} & c_{23}\end{pmatrix}\begin{pmatrix}c_{13} & 0 & s_{13}e^{-i\delta_{CP}}\\ 0 & 1 & 0\\ -s_{13}e^{i\delta_{CP}} & 0 & c_{13}\end{pmatrix}\begin{pmatrix}c_{12} & s_{12} & 0\\ -s_{12} & c_{12} & 0\\ 0 & 0 & 1\end{pmatrix} \times \begin{pmatrix}e^{-i\frac{\alpha_1}{2}} & 0 & 0\\ 0 & e^{-i\frac{\alpha_2}{2}} & 0\\ 0 & 0 & 1\end{pmatrix}\begin{pmatrix}\nu_1\\ \nu_2\\ \nu_3\end{pmatrix} \tag{2.7}$$

where $c_{jk} = \cos\theta_{jk}$ and $s_{jk} = \sin\theta_{jk}$. If we multiply the three rotation matrices together, we get the unitary mixing matrix:

$$U = \begin{pmatrix} c_{12}c_{13} & s_{12}c_{13} & s_{13}e^{-i\delta_{CP}}\\ -s_{12}c_{23} - c_{12}s_{23}s_{13}e^{\delta_{CP}} & c_{12}c_{23} - s_{12}s_{23}s_{13}e^{\delta_{CP}} & s_{23}c_{13}\\ s_{12}s_{23} - c_{12}c_{23}s_{13}e^{\delta_{CP}} & -c_{12}s_{23} - s_{12}c_{23}s_{13}e^{\delta_{CP}} & c_{23}c_{13}\end{pmatrix} \times \begin{pmatrix}e^{-i\frac{\alpha_1}{2}} & 0 & 0\\ 0 & e^{-i\frac{\alpha_2}{2}} & 0\\ 0 & 0 & 1\end{pmatrix} \tag{2.8}$$

This unitary mixing matrix was first postulated by Maki, Nakagawa, and Sakata to describe neutrino oscillations that were predicted by Pontecorvo. Because of this, it is named the PMNS matrix.

In the three flavor case, the equivalence to Equation 2.5 is:

$$|\nu_\alpha(\overrightarrow{x}, t)\rangle = \sum_j U^*_{\alpha j} e^{-i\frac{m_j^2}{2}\frac{L}{E}} |\nu_j(0)\rangle \tag{2.9}$$

Using a method similar to that used in Section 2.2.1, the oscillation probabilities can be written as:

$$
\begin{aligned}
P(\nu_\alpha \to \nu_\beta) =& \delta_{\alpha\beta} \\
&- 4\sum_{j>k} \mathbb{R}(U^*_{\alpha j} U_{\beta j} U_{\alpha k} U^*_{\beta k} \sin^2\left(\frac{1.27\Delta m^2_{jk} L}{E}\right)) \\
&+ 2\sum_{j>k} \mathbb{I}(U^*_{\alpha j} U_{\beta j} U_{\alpha k} U^*_{\beta k} \sin\left(\frac{2.54\Delta m^2_{jk} L}{E}\right))
\end{aligned} \tag{2.10}
$$

where $\mathbb{R}$ and $\mathbb{I}$ are the real and imaginary parts of the formula in parentheses, and $\Delta m^2_{jk} = m^2_j - m^2_k$. For the $\nu_\mu \to \nu_e$ appearance channel, one will often see the probability written out as:

$$
P(\nu_\mu \to \nu_e) \approx \sin^2\theta_{23} \sin^2 2\theta_{13} \sin^2\left(\frac{\Delta m^2_{32} L}{4E}\right) \tag{2.11}
$$

which is correct to the first order. However, this equation is still too simplified to do a precise measurement of oscillation parameters and is missing several effects. One effect is that δ_{CP} has been taken out meaning no measurement on CP violation could be made. The other is that matter effects still have not been taken into account and is the subject of the next section.

2.2.3 Matter Effects

So far we have only included oscillations that occur in a vacuum and have had no potential in our Schrödinger equation. Lincoln Wolfenstein pointed out in 1978, though, that when electron neutrinos travel through matter they would be affected by coherent elastic forward scattering [10]. This would only happen with charged current (CC) interactions that include the $W^\pm$ boson. As CC interactions only act on particles of the same lepton flavor and normal matter only has electrons in it, this only plays a role in how ν_e oscillate. Later on in 1984, Smirnov and Mikheyev also discovered this process independently, so it is commonly referred to as the MSW effect.

The MSW effect is seen in the oscillation formula by adding in a potential to the Hamiltonian that only effects the ν_e component. Here, the potential is:

$$
V = \pm\sqrt{2} G_F N_e \tag{2.12}
$$

where G_F is the Fermi coupling constant and N_e is the electron density per unit volume. The potential takes a positive sign for ν_e interactions and negative for $\overline{\nu}_e$. Like done in the last two sections, this extra potential can be added into our Hamiltonian and solve the Schrödinger equation to find the new oscillation

properties. It is possible to solve this analytically, but the mathematics of doing so are rather involved and has been kept out of this dissertation for brevity's sake.

2.2.4 Probability of $\nu_\mu \rightarrow \nu_e$ oscillations

Now we finally have everything needed to look at the probability of $\nu_\mu \rightarrow \nu_e$ oscillations.

$$\begin{aligned} P(\nu_\mu \rightarrow \nu_e) =& 4c_{13}^2 s_{13}^2 s_{23}^2 \sin^2 \Phi_{31} \\ &+ 8c_{13}^2 s_{12} s_{13} s_{23} (c_{12} c_{23} \cos \delta_{CP} - s_{12} s_{13} s_{23}) \cos \Phi_{32} \sin \Phi_{31} \sin \Phi_{21} \\ &- 8c_{13}^2 c_{12} c_{23} s_{12} s_{13} s_{23} \sin \delta_{CP} \sin \Phi_{32} \sin \Phi_{31} \sin \Phi_{21} \\ &+ 4s_{12}^2 c_{13}^2 (c_{12}^2 c_{23}^2 + s_{12}^2 s_{23}^2 s_{13}^2 - 2c_{12} c_{23} s_{12} s_{13} \cos \delta_{CP}) \sin^2 \Phi_{21} \\ &- 8c_{13}^2 c_{13}^2 s_{23}^2 \frac{aL}{4E} (1 - 2s_{13}^2) \cos \Phi_{32} \sin \Phi_{31} \\ &+ 8c_{13}^2 s_{13}^2 s_{23}^2 \frac{a}{\Delta_{31}^2} (1 - 2s_{13}^2) \sin \Phi_{31} \end{aligned} \tag{2.13}$$

where the substitutions of Φ_{ij} and a have been made and are defined as:

$$\Phi_{ij} \equiv \frac{\Delta_{ij}^2 L}{4E} = 1.27 \frac{\Delta m_{ij}^2 [eV^2] L[km]}{E[GeV]} \tag{2.14}$$

$$a \equiv 2\sqrt{2} G_F N_e E = 7.56 \times 10^{-5} \times \rho[g/cm^3] \times E \tag{2.15}$$

Here, a represents the factor associated with the MSW effect and ρ represents the density of the medium the neutrinos are traveling through. $P(\overline{\nu_\mu} \rightarrow \overline{\nu_e})$ can be found by replacing $\delta_{CP} \rightarrow -\delta_{CP}$ and $a \rightarrow -a$ in Equation 2.13. This probability has been arranged in such a manner that it is easier to extract useful information. The first term is the leading order effect and is equivalent to Equation 2.11. The second term has $\cos \delta_{CP}$ in it and is called the CP conserving term while the third term has $\sin \delta_{CP}$ and is called the CP violating term. The fourth term is dominated by s_{12}^2 and is therefore called the solar term. The final two terms are the corrections that are added from the matter effects. For this dissertation, when $P(\nu_\mu \rightarrow \nu_e)$ is used for any calculations or measurement, Equation 2.13 is always used instead of the often seen simplified version Equation 2.11.

2.3 Neutrino Interactions

2.3.1 Neutral Current

Neutral current (NC) interactions are any interactions that are mediated through the Z boson. Because the Z^0 is neutral, it is called neutral current. The simplest neutrino interaction to understand is that of NC elastic scattering. This occurs when an incoming neutrino scatters off of an electron (see Section 2.2.3 or nucleon. The scattering causes the electron/nucleon to recoil, but no other experimental signatures are left by this process.

$$\nu + N \rightarrow \nu + N \tag{2.16}$$

Because there is no change in mass, this is a threshold-less interaction.

At higher energies, sufficient energy may be transferred to create other particles, usually pions. One of the largest backgrounds for T2K is NCπ^0 interactions at Super-K due to their ability to mimic CCQE ν_e interactions (see next section.) In these interactions, the neutrino scatters off the nucleus and creates an intermediate particle like Δ or N^*. This intermediate particle then decays into a neutral pion [11].

In all neutral current interactions, no charge is transferred. The incoming neutrino remains unchanged after the interaction and only the energy and momentum is transferred. Because of this, NC interactions are not dependent on the incoming neutrino's flavor and are usually a background for the T2K.

2.3.2 Charged Current Quasi-elastic

Charged current (CC) interactions are those mediated through the $W^{\pm}$ boson. As the $W^{\pm}$ has a charge, these interaction are called charged current. In these interactions, the neutrinos interact with the nucleus and are converted into a lepton.

The most important interactions for T2K are charged current quasi-elastic (CCQE) scattering. These are the interaction that are used for signal at Super-K . At energies below 1 GeV, CCQE interactions usually take the form:

$$\nu_l + n \rightarrow p + l^- \tag{2.17}$$

$$\overline{\nu}_l + p \rightarrow n + l^+ \tag{2.18}$$

This simple interaction allows for easy energy reconstruction and a clean channel for detecting ν_e and ν_μ. They take the name quasi-elastic because a massive particle is created in the interaction [11].

Like with NC interactions, at higher energies resonance production can occur usually with a charged pion in the final state. At even higher energies (above 10 GeV) deep inelastic scattering (DIS) dominates neutrino interactions. Here, neutrinos have enough energy that they scatter of the quarks inside the nucleon and can break up the nucleus. These interactions can be very hard to classify due to the large amount of energy transfer that can produce a wide variety of multi-particle final states.

2.4 Unanswered Questions

As mentioned at the beginning of this chapter, neutrino oscillations have only been confirmed for the last 16 years. In that short span of time, though, there have been large leaps in our understanding of neutrino oscillations. Despite all of the knowledge we have gained recently, there are still a number of large number open questions in neutrino physics that current and future experiments are trying to answer.

One question is exactly how many species of neutrinos are there? So far only three neutrino flavors have been observed, ν_e, ν_μ, and ν_τ, and the PMNS matrix can describe their oscillations. It is possible for there to be more than just three mass eigenstates, however. If this is the case, then there is a linear combination of mass eigenstates that do not couple with the Z and $W^{\pm}$ bosons. These are called sterile neutrinos because they would only couple to gravity and are not directly detectable.

Another current question is if neutrinos are their own antiparticles. It was discussed briefly in Section 2.2.2 that neutrinos could be Majorana instead of Dirac particles. The Majorana phase cannot be directly measured by oscillation experiments, though, and can only be found through neutrino-less double beta decay experiments.

The fact that neutrinos have mass is why they oscillate. The exact mass of neutrinos is still not known, though limits set it to be less than 2 eV [12]. The exact masses do not appear in the PMNS matrix, only the mass splittings. Because the mass splitting is the difference of the squared masses the exact sign of the mass differences is still not known for Δm_{31}. This can lead to two possible solutions: one where $\nu_1 < \nu_3$ (normal hierarchy) and one where $\nu_1 > \nu_3$ (inverted hierarchy.) Figure 2.1 shows a pictorial representation of the mass hierarchy and the flavor component for each mass eigenstate. Determining the mass hierarchy is very important in the field as most oscillation results differ depending whether the mass hierarchy is normal or inverted.

The final big questions in neutrino physics are the purpose of this dissertation. Until just recently, the exact value of θ_{13} was not known. There were

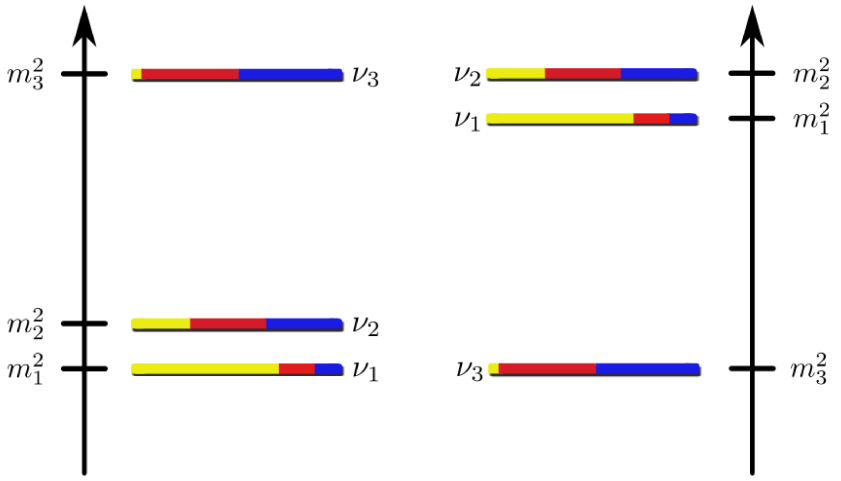

Figure 2.1: A pictorial representation of the neutrino mass eigenstates with their flavor eigenstate composition for both normal hierarchy (left) and inverted hierarchy (right). Yellow indicates ν_e, red ν_μ, and blue is ν_τ.

upper limits, but whether θ_{13} was finite or zero was still unknown. As δ_{CP} is coupled with θ_{13}, if θ_{13} is zero then there could be no CP violation in the leptonic sector. Precise measurements of θ_{13} now exist and such a measurement forms the primary analysis upon which this dissertation is based on. Now that these measurements do exist, the determination if CP violation exist in the lepton sector is possible. In this dissertation, a constraint on δ_{CP} is made and is the topic of Chapter 10.

Chapter 3

T2K Overview

3.1 Introduction

The T2K experiment was first proposed in 2001 as the JHF-Kamioka neutrino project and is a second generation long baseline neutrino oscillation experiment[13]. The primary goal was set to make a more precise measurement on $\delta(\Delta m^2_{32}) \sim 10^{-4} eV$ and $\delta(\sin^2(2\theta_{23}))\sim 0.01$ via ν_μ disappearance studies, thus allowing for a factor of 20 more sensitive search in the $\nu_\mu \rightarrow \nu_e$ appearance channel of θ_{13} [14]. Apart from this primary goal, T2K is also designed to set limits on sterile neutrinos through NC measurements, on δ_{CP} and the mass hierarchy if results are combined with other experiments, and on neutrino cross sectional measurements.

The T2K experiment itself consists of a neutrino beam, a near detector, and a far detector. The neutrino beam and near detector are explained in detailed in this chapter. The far detector, Super-Kamiokande, deserves more attention than a single section and will be discussed in Chapter 4.

3.2 J-PARC Accelerator and Beamline

The Japan Proton Accelerator Complex (J-PARC), was a newly constructed facility in Tokai, Ibaraki, and consists of three accelerators: a linear accelerator (LINAC), a rapid-cycling synchrotron (RCS), and the main ring (MR) synchrotron. A H^- beam is accelerated up to 400 MeV (181 MeV for the data-set this dissertation is based on) by the LINAC and is then converted to a H^+ beam by charge-stripping foils at the RCS injection. The RCS further accelerates the beam to 3 GeV with a 25 Hz cycle. About 5% of the beam is then supplied to the MR with the rest going to the muon and neutron beamline in the Material and Life Science Facility at J-PARC. The protons that

Table 3.1: The machine design parameters for the J-PARC MR.

Circumference	1567 m
Beam Power	$\sim$ 750 kW
Beam Kinetic Energy	30 GeV
Beam Intensity	$\sim 3 \times 10^{14}$ p/spill
Spill Cycle	$\sim$ 0.5 Hz
Number of Bunches	8/spill
RF Frequency	1.67-1.72 Hz
Spill Width	$\sim$ 5 μsec

do make it to the MR are accelerated to 30 GeV. The harmonic number of the MR is nine, but there are only eight bunches in it at a time (six for T2K Run1.) The machine design parameters for the J-PARC MR can be found in Table 3.1.

The neutrino beamline is made up of two parts: the primary beamline and the secondary beamline. The purpose of the primary beam is to guide the protons extracted from the MR to point toward Super-K . The secondary beamline have the protons hit a fixed target where secondary pions are produced and decay into neutrinos. A schematic overview of the neutrino beamline can be seen Figure 3.1. The primary beamline section is labeled in red while the secondary beamline is shown in blue.

The primary beamline consist of three different sections: the preparation section, the arc section, and the final focusing section labeled as 1, 2, and 3 in Figure 3.1. The preparation section is 147 meters long and is where the proton beam is tuned for acceptance in the arc section. This is done with 11 normal conducting magnets: four steering, two dipole, and five quadrupole magnets. The arc section bends the beam towards Super-K with 14 doublets of superconducting combined function magnets and corrects the beam's orbit with three pairs of superconducting steering magnets. In the final section of the primary beamline, the final focusing section guides the beam onto a fixed carbon target while pointing the beam downwards by 3.637^o with respect to the horizon. This is accomplished with four steering, two dipole, and four quadrupole normal conducting magnets.

The secondary beamline also consists of three different sections: the target station, the decay volume, and the beam dump. The target station itself is comprised of: a beam window separating the primary beamline from the target station, a baffle which is a collimator to protect the magnetic horns, an optical transition radiation monitor (OTR) to monitor the proton beam

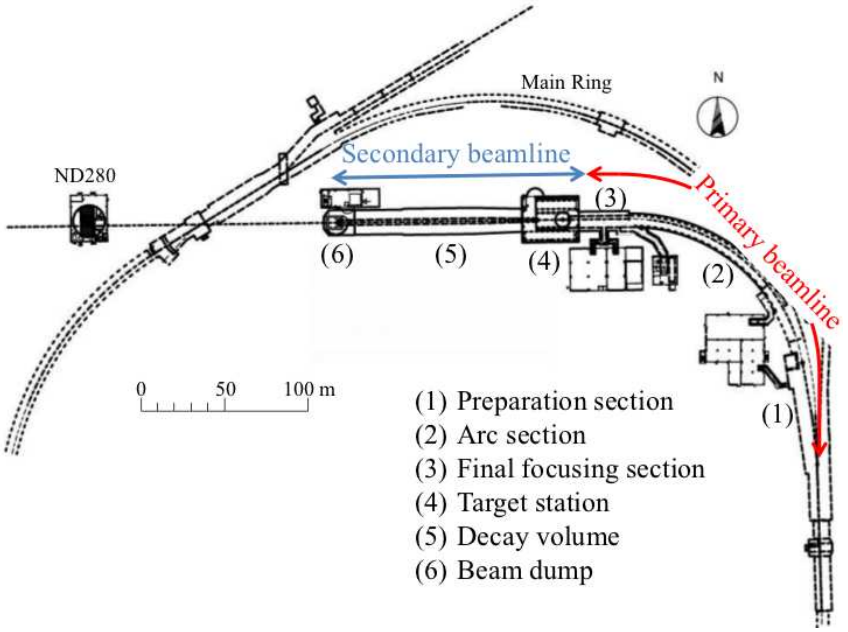

Figure 3.1: This figure hows a schematic overview of the neutrino beamline. The sections of the primary beamline are indicated in red while the secondary beamline is in blue. The preparation section (1), arc section (2), final focusing section (3), target station (4), decay volume (5), and beam dump (6) are all labeled and described in Section 3.2.

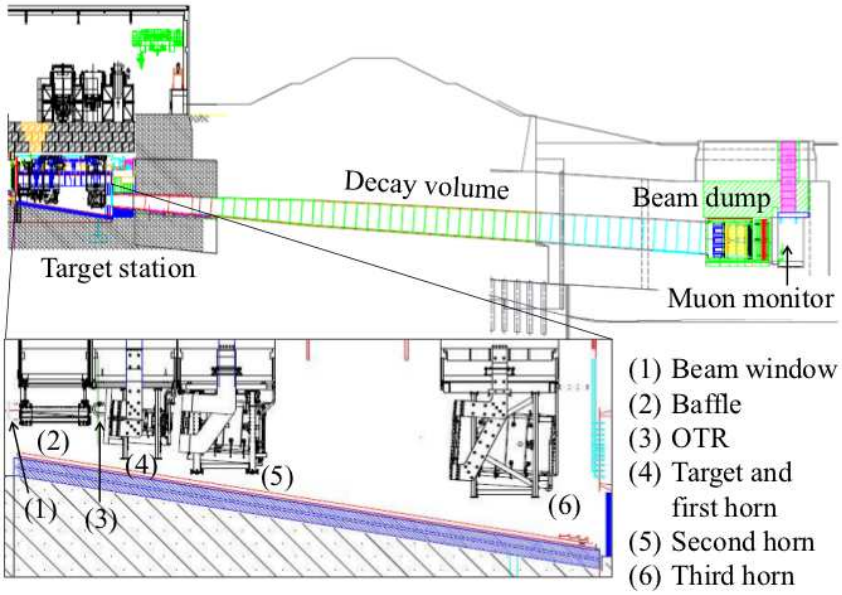

Figure 3.2: The secondary beamline with a detailed view of the target station.

profile, a graphite target to generate secondary pions, and three magnetic horns to focus the pions. The pions then enter a ∼1500 m^3 decay volume that is filled with helium gas and kept at 1 atm. The decay volume is filled with helium to help reduce pion absorption and to suppress the production of tritium and NO_x. Within the decay volume, almost all pions decay into muons and muon neutrinos. At the end of the decay volume is the beam dump. The beam dump is made of 75 tons of graphite (3.174 meters long, 1.94 meters, and 4.69 meters high) and 15 iron plates with a total thickness of 2.40 meters. All hadrons, and muons below 5 GeV/c are stopped by the beam dump and only the neutrinos continue on. All muons that do pass are monitored at the end of the beam dump and help to characterize the neutrino beam. A detailed view of the entire secondary beamline and components of the target station are shown in Figure 3.2.

3.3 Off-Axis Beam

T2K is the first neutrino oscillation experiment to utilize the off-axis method [15] which generates a narrow band neutrino beam. This method exploits the unique kinematics of a two-body decay that involves a neutrino. This is because we can treat neutrinos as a massless particle, greatly simplifying the equations. For a pion decaying along a direction defined by the axis of

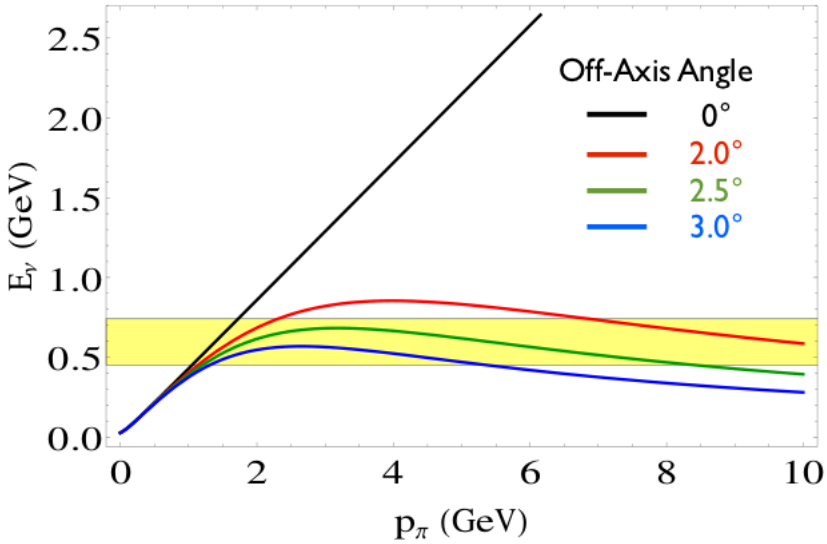

Figure 3.3: The neutrino energy as a function of pion momenta. The yellow band highlights the T2K oscillaton maximum. T2K uses an off-axis angle of 2.5^o, which corresponds to a peak neutrino energy of about 600 MeV

the tunnel, we can work out from the basic four-momentum that the neutrino energy will be

$$E_\nu = \frac{m_\pi^2 - m_\mu^2}{2(E_\pi - p_\pi \cos\theta_\nu)} \tag{3.1}$$

where m_π and m_μ are the pion and muon rest mass, E_π is the pion energy, p_π is the pion momentum, and θ_ν is the angle at which the neutrino is emitted. Figure 3.3 shows a plot of E_ν as a function of p_π after the pion's energy is writen in terms of its momentum. You can see from the figure that for an on-axis beam ($\theta_\nu = 0$) that the neutrino's energy is proportional to the pions momentum. As the angle is increased, though, the neutrino energy begins to decouple from the pion's momentum and we can get a very narrow band of neutrinos from a large range of pion momenta. Further more, the peak of the neutrino energy spectrum shifts down as the angle increases, allowing us to tune the neutrino energy to peak where we expect the largest oscillaton signal. This is what T2K has done. For a baseline of 295 km, an off-axis angle of 2.5^o was chosen to maximize the ν_e appereance signal at Super-K .

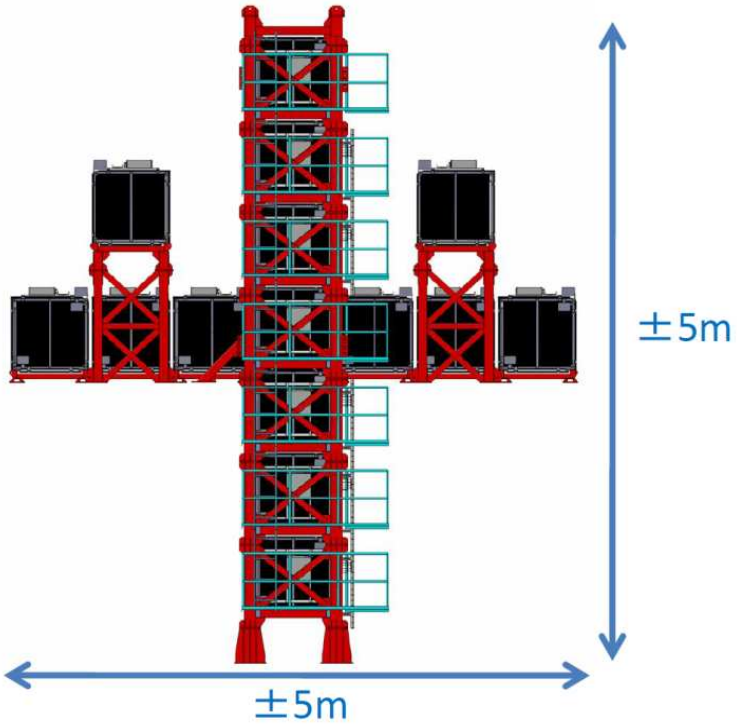

Figure 3.4: The on-axis detector, INGRID.

3.4 ND280

The Near Detector Complex (ND280) measures the unoscillated neutrino energy spectrum, flavor content, and interaction rates with a series of detectors located 280 meters from the production target. It is used to predict the neutrino interactions in Super-K and reduce all interaction and beam uncertainties. ND280 itself is made up of two detectors, an on-axis detector called INGRID to measure the on-axis beam profile and an off-axis detector surrounded 0.2T magnet. These detectors are housed in a pit 37 meters deep and 17.5 meters in diameter. The complex was designed to accommodate off-axis angles ranging from 2.0 to 2.5^o which is constrained only by the requirement that the beam axis pass through the central area of INGRID [14]

3.4.1 INGRID

The on-axis detector is called the Interactive Neutrino GRID (INGRID). Its purpose is to directly monitor the neutrino beam interactions to provide daily measurements of the beam position. It has the ability to measure the center

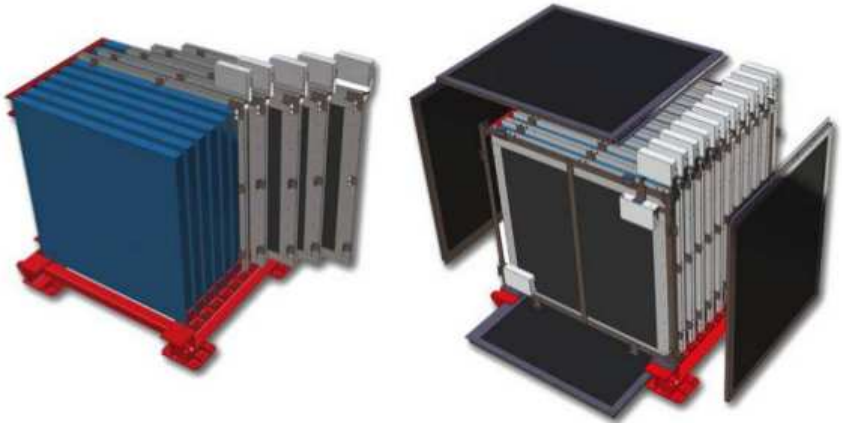

Figure 3.5: The left figure shows the tracking planes (blue) and iron plates (grey/black) of an INGRID module. The figure on the right shows the veto planes (black).

of the beam to better than 10 cm, or about 0.4 mrad. INGRID consists of 14 identical modules arranged in a cross configuration: 7 vertical and 7 horizontal with the center of the cross having two overlapping modules. The center of the cross corresponds to the center of the neutrino beam with respect to the primary proton beamline. Apart from the 14 modules making up the cross, INGRID has two more off-axis modules that are used to check the axial symmetry of the neutrino beam. The INGRID detector can be seen in Figure 3.4 where the z-axis is defined by the beam direction [14].

Each of the INGRID modules has 11 tracking scintillator planes with 9 iron plates sandwiched between each one. The iron plates themselves are 124 cm×124 cm and 6.5 cm thick for a total mass of 7.1 tons per module. The 11 tracking planes are made up of 48 scintillator bars, 24 in the x direction and 24 in y. Each bar is 1.0 cm×5.0 cm × 120.3 cm. The entire module is covered by veto scintillator planes that reject any interactions that started outside the module. These veto scintillator planes are made up of 22 scintillator bars that are each 1.0 cm×5.0 cm × 111.9 cm for the bottom veto planes and 1.0 cm×5.0 cm × 129.9 cm for all others. Figure 3.5 shows a drawing of a INGRID module and how it is constructed.

Each extruded scintillator bar has a hole with a diameter of 3 mm in the center of it. A wavelength shifting fiber with a diameter of 1 mm is feed through each hole. The extruded plastic scintillator was produced at Fermilab and has an emission peak at 420 nm [16]. The wavelength shifting fibers absorption spectrum is centered around 430 nm while its emission spectrum is centered at 476 nm. Each fiber is connected to a multi-pixel photon counter

(MPPC) and are readout by the front-end electronic boards, the Trip-T front-end boards (TFBs) [14].

3.4.2 Multi-Pixel Photon Counter

All of the detectors in ND280, except the TPC, use scintillator detectors with wavelength shifting fibers connected to photosensors. In past neutrino experiments, multi-anode PMTs have been used for the photosensors, but these cannot operate inside of a magnet and are therefore not well suited for ND280. Instead, a multi-pixel avalanche photodiode was selected to be used for the photosensor. The multi-pixel avalanche photodiodes are made of many independent Geiger micro-counters that have about the same gain as vacuum PMTs. These are well suited for use inside of ND280 as they are insensitive to magnetic fields and have a peak detection efficiency matched to the emission of wavelength shifting fibers [17].

The exact multi-pixel avalanche photodiode chosen to be used are the Hamamatsu Multi-Pixel Photon Counter (MPPC). It has a sensitive area of 1.3×1.3 mm^2 with a total of 667 pixels [18]. The pixels are arranged in a 26×26 array with nine pixels missing in the corner which is occupied by an electrode. In total, Hamamatsu produced 64,000 MPPCs for the T2K experiment. An overview of some of the MPPCs properties are listed in Table 3.2.

Table 3.2: Overview of parameters for the MPPCs used in ND280.

Number of pixels	667
Active area	1.3×1.3 mm^2
Pixel size	50×50 μm^2
Operational voltage	68-71 V
Gain	$\sim 10^6$
Photon detection efficiency at 525 nm	26-36%
Dark rate (threshold=0.5 p.e., T=25^{0}C	$\leq$ 1.35 MHz

3.4.3 Off-axis Detector

The ND280 off-axis detector is critical to reduce uncertainties in the beam's properties and neutrino production rates. It was designed to determine the ν_μ flux expected at Super-K, measure the ν_e content of the beam over all energies, and measure ν_μ interactions to constrain the backgrounds to the ν_e appearance at Super-K. To accomplish these goals, the off-axis detector is made up of: the

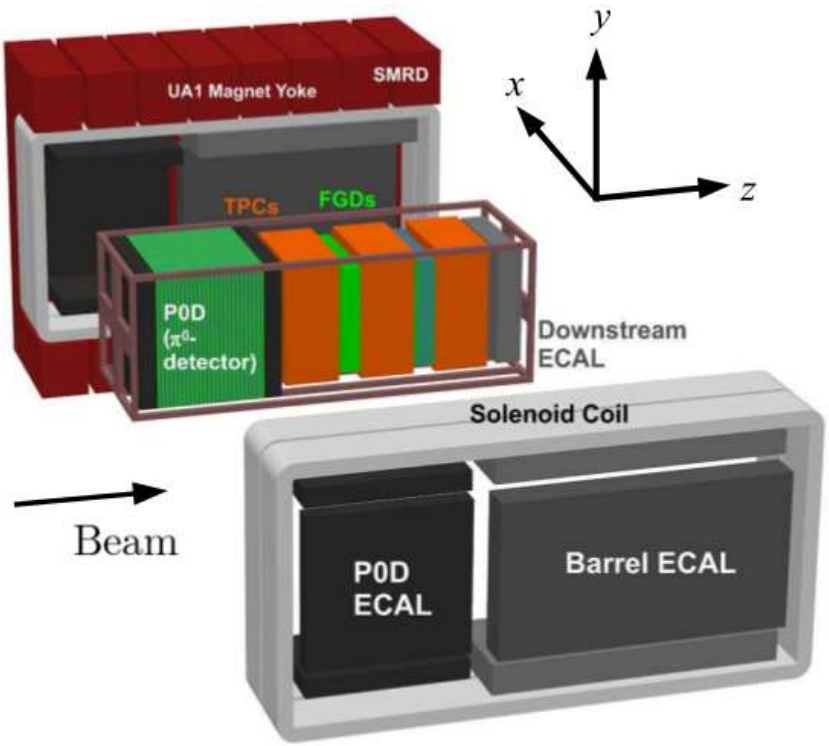

Figure 3.6: The ND280 off-axis detector.

PØD and the TPC/FGD sandwich (tracker), an electromagnetic calorimeter (ECal) that surrounds them, and the recycled UA1 magnet instrumented with scintillator to perform as a side muon range detector (SMRD). Figure 3.6 shows all parts of the ND280 off-axis detector [14].

UA1 Magnet

The ND280 off-axis detector uses an upcycled magnet from the old CERN UA1 experiment to measure the sign of charged particles produced in neutrino interactions and help measure their momenta. It provides a dipole magnetic field with a strength of 200 G. In total it weighs 850 tons and measures 7.6 m $\times$ 5.6 m $\times$ 6.1 m on the outside. Its internal cavity is 7.0 m $\times$ 3.5 m $\times$ 3.6 m and houses all of the off-axis detector except for the SMRD.

The magnet was refurbished at CERN before being shipped to Japan and installed in the ND280 pit. It is made of two identical halves that are mounted on tracks. This allows the magnet to be opened and closed easily when work needs to be done. Detailed measurement were performed to map the magnet field strength inside the magnet. A total magnetic field uncertainty of 2 G was achieved allowing for a momentum determination below 2% for charged particles below 1 GeV [14].

Pi-zero Detector

As mentioned previously, one of the largest backgrounds to the ν_e appearance search are π^0s. With this in mind, the PØD (Pi-zero Detector) was designed specifically to precisely measure the neutral current process $\nu_\mu + N \rightarrow \nu_\mu + N + \pi^0 + X$ on water. Because the PØD measure the NCπ^0 on water, it must have a large water mass that can be filled and emptied, allowing for a subtraction method to determine the neutrino's cross sections on water. It also helps constrain the ν_e contamination in the beam, which is an irreducible background to the ν_e appearance search. The PØD was constructed at Stony Brook University before being shipped off to J-PARC.

Figure 3.7 shows the primary features of the PØD . The central section is made of the "upstream water target" and "central water target", and alternated scintillator planes, water bags, and brass sheets. In the front and back are the "upstream ECal" and "central ECal" that use alternating scintillator planes and lead sheets. By having an ECal section upstream and downstream of the central water target, a veto can be set up to reject any charged particles coming from outside the PØD [19].

Each PØD module, or PØDule , has 134 horizontal and 126 vertical triangular scintillator bars. Each bar has a wavelength shifting fiber running through

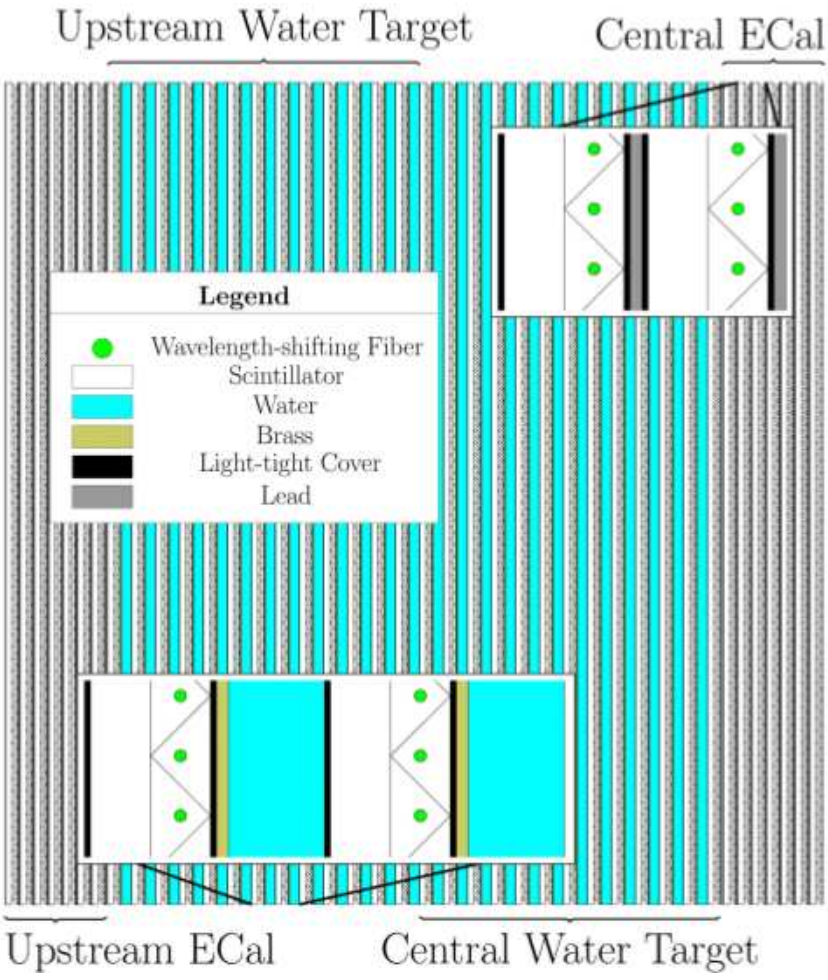

Figure 3.7: A schematic of the four Super-PØDules that make up the PØD .

it that are coupled with a MPPC. In total, there are 40 PØDules in the PØD , 7 in each ECal and 13 in each of the water target. These four sections of the PØD are each called a Super-PØDule . The two ECal Super-PØDules each have seven stainless steel clad lead sheets, 4.5 mm thick, sandwiched between its PØDules . The upstream (central) water target Super-PØDule has 13 (12) water bag layers (each of which is 28 mm thick) and 13 (12) brass sheets (1.28 mm thick) alternating with its PØDules . In total the PØD is 2103 mm $\times$ 2239 mm $\times$ 2400 mm and has a mass of 15,800 kg with water and 12,900 kg without [19].

Time Projection Chamber and Fine Grained Detector

The Time Projection Chamber (TPC) and Fine Grained Detector (FGD) are the main tracking detectors for the ND280 off-axis detector. The TPC is particularly useful at being able to select high purity samples of different neutrino interactions due to its excellent imaging capabilities. In all there are three TPCs with two FGDs placed in between each one. One downstream most FGD is a water rich detector allowing the FGD to both have good target mass for neutrino interactions and good tracking abilities.

Each TPC is 2.3 m $\times$ 2.4 m $\times$ 1.0 m and contains an inner and out section. The outer box contains CO_2 as an insulating gas. The inner gas mixture is 95% Argon with 3% CF_4 and 2% iC_4H_{10}. This ratio was chosen for its high speed and low diffusion. Each TPC contains 3000 liters of gas and have a flow rate of 10 L/min. The ionization left behind from the charge particle is read out with bulk micromegas detectors [20]. There are twelve 342 mm $\times$ 359 mm micromegas modules that tile each of the readout planes. In total there are 72 modules which provide 9 m^2 of active surface for all three TPCs.

The FGDs are made of extruded polystyrene scintillator bars that are each 9.61 mm $\times$ 9.61 mm $\times$ 1846.3 mm. Each FGD is 2300 mm $\times$ 2400 mm $\times$ 365 mm and has 1.1 tons of target material. The upstream FGD has 5,760 scintillator bars arranged into 30 layers alternating in the x and y direction. The downstream FGD has a total of 2,688 scintillator bars in 7 layers that alternate with six 2.5 cm thick layers of water. Each of the scintillator bars has a wavelength shifting fiber in each and are read out by MPPCs like most of the other detectors in ND280 [14].

Electromagnetic Calorimeter

Electromagnetic calorimeters (ECal) surround the PØD , TPCs, and FGDs to provide almost complete coverage for all particles exiting the inner detectors. One of the key functions of the ECal is to reconstruct π^0 that are produced

inside the trackers. The PØD -ECal fully complements the PØD reconstruction by measuring any energy that may of escaped the PØD . There are a total of 13 independent ECal modules: six Barrel-ECal modules that surround the tracker volume, one downstream module (Ds-ECal) that covers the downstream side of the tracker, and six PØD -ECal that surround the PØD .

All the ECals use scintillator bars that have a cross section of 4.0 cm $\times$ 1.0 cm. Each bar has a 2.0 mm $\times$ 3.0 mm elliptical hole running along the length of it. Inside each hole a wavelength shifting fiber collects all scintillation light an it is read out by MPPCs. Each of the ECals consist of scintillator layered with 1.75 mm thin lead sheets.

Side Range Muon Detector

The Side Range Muon Detector (SMRD) consists of many scintillator modules which are inserted into gaps in the UA1 magnet. It triggers on cosmic rays that enter the ND280 detector, allowing the other detectors to have a veto. It also records muons escaping at high angles with respect to the beam and can measure the momenta. Finally, it helps identify beam related event interactions that occur in the surrounding wall and the iron of the magnet.

There are a total of 440 scintillator modules placed inside 1.7 cm air gaps that exist inside the UA1 magnet. The spacing and size of each individual detector is determined by the geometry of the magnetic yoke spacing. Each module has an S shaped groove, with a radius of curvature of 2.9 cm machined, into it. A wavelength shifting fiber is positioned into each groove and connected to an MPPC to be read out.

Chapter 4

The Far Detector

Super-Kamiokande (Super-K) is a large water Cherenkov detector located 295 km west of beam source and is used for the far detector of T2K. It was built 1 km deep within the center of Mt. Ikenoyama in the Mozumi mine of the Kamioka Mining and Smelting Company near the village of Higashi-Mozumi, Gifu, Japan. Super-K started running in 1996 and has produced world leading limits on the proton lifetime and the measurement of flavor oscillations in atmospheric, solar, and accelerator produced neutrinos. During its almost 20 years of service, Super-K has had four running periods: SK-I, SK-II, SK-III, and SK-IV. SK-IV is still in progress and is the period in which the T2K experiment takes place.

4.1 Super-Kamiokande Detector Overview

The Super-K detector is made up of two major volumes, the inner (ID) and outer detector (OD), which are separated by a cylindrical stainless steel structure. Figure 4.1 shows a schematic view of the Super-K detector. The ID is a cylindrical space 33.8 meters in diameter and 36.2 meters in height which contains 32 ktons of water. It has 11,129 50 cm PMTs facing inwards that provide 40% photo-cathode coverage of the tank. The ID is enclosed by the OD, which is a cylindrical space 2 meters outside the ID. The OD consists of 1,885 outward facing 20 cm PMTs. The OD and ID boundary is defined by a cylindrical stainless steel scaffold structure that is 50 cm wide and is the only "dead-space" within the detector. All together, this makes Super-K a total of 39 meters in diameter and 42 meters in height [21].

Super-K is a large water Cherenkov detector and uses the Cherenkov light produce by charged particles as they travel faster than light in water. When the photons from the Cherenkov light reach the PMTs on the detector walls,

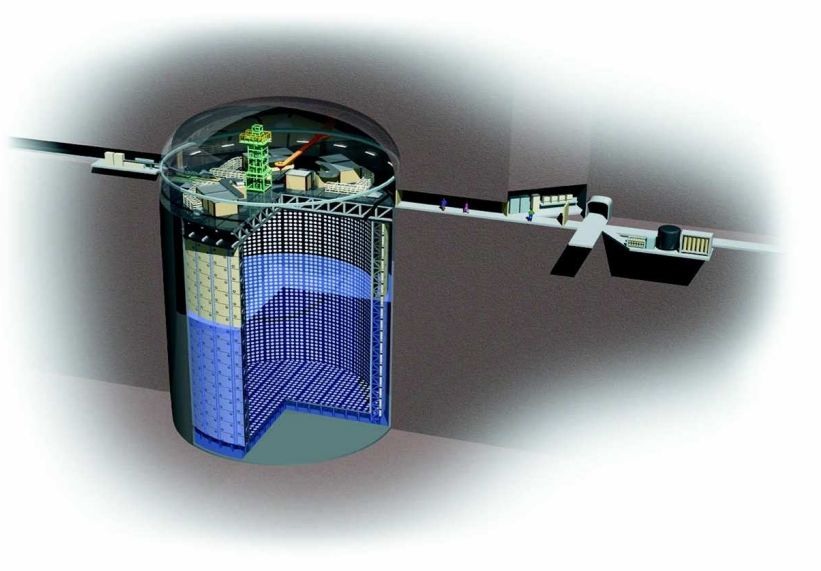

Figure 4.1: A schematic view of the Super-K detector.

they produce a ring-shaped hit pattern which is used to extract information about the interaction such as the event vertex position and momenta of product particles. To measure the flavor of the neutrino interaction in Super-K is to count charged current quasi-elastic (CCQE) interactions for muon and electron neutrinos, both of which produce leptons of their respective flavor. Muons are counted to measure the ν_μ disappearance in the T2K beam. Due to their high mass, muons that travel through the detector produce a well-defined cone of Cherenkov radiation which leads to a clear, sharp ring of PMT hits seen on the detector wall. Electrons, however, used to search for ν_e appearance, scatter more easily because of their smaller mass and pair-produce to induce electromagnetic showers. The result of this is a fuzzy ring pattern seen by the PMTs, and is like many overlapping Cherenkov light cones.

4.2 Super-K Electronics and DAQ

In 2008, Super-K completed a major upgrade to the detector's electronic readout that uses a new scheme in the acquisition of hits from the detector's PMTs. Previously, a hardware trigger would trip and send data off to be saved if the total number of PMT hits was within a 200 ns time window exceeded some threshold. This system was not adequate enough for low energy neutrinos searches because the front-end electronics data throughput was too low to accommodate a lower threshold of triggering. To over come this, the new elec-

tronic system has front-end boards capable of much higher data processing rate. The system was further improved by changing from the old hardware triggers to a new software triggering system. With the new system, the arrival time and charge of each PMT hit is sent to a cluster of online PCs. These PCs search for neutrino event candidates based off of any number of software triggers. This new system allows Super-K to accommodate a larger range of neutrino searches and even has the capabilities of implementing a coincidence trigger with a beam arrival time as is used by the T2K experiment.

The new front-end boards are named QTC Based Electronics with Ethernet, or QBEE boards. The names comes from the start and end of the boards signal processing chain. The Charge to Time Converter (QTC) is a custom built application-specific integrated circuit (ASIC) that produce a square-wave pulse from the input of the PMT signal. The leading edge of the square-wave coincides with the arrival time of the PMT signal and the length of the pulse is proportional to the integrated charge of the PMT pulse. This data is then digitized with a Time to Digital Converted (TDC) before being sent to readout PCs using Ethernet. The QBEE boards are able of transferring up to 11.8 MB/s of data. This corresponds to an input pulse rate of 80 kHz/channel, and order of magnitude improvement over the old system which could only handle 1.4 kHz/channel. All together, the Super-K DAQ system uses 550 QBEE boards which read out all 13,014 PMTs.

The data from the QBEE boards is sent to a cluster of online PCs whose role is to organize the PMT hit information and produce data files of candidate events which can be processed more offline. To complete this task, the online PCs are split up into three different groups. The first group consists of "front-end" PCs that sort the PMT hit information by time. The second group, "Merger" PCs, collect all hits into a time-ordered list and apply a set of software triggers to select different event candidates. Each of these candidate events has a time window defined around the event trigger and hit information. These candidate events with their time windows are then sent to the final "Organizer" PC. This machine collects all of the candidate events, eliminates any overlap of events, and writes them to disk. On a typical day, Super-K collects about 470 MB/s of raw data. With a software trigger rate of 3 kHz, about 9 MB/s worth of candidate event data is saved to disk [14].

4.3 Water and Air Purification

The Super-K tank is filled with some of the purest water in the world. Maintaining a higher purity of water is crucial for several reasons. The first is that any impurities will lower the transparency of the Super-K water, therefor

lowering the light collection and worsening the event reconstruction. Another reason is if the water transparency changes over time, this will lead to energy-scale calibration problems and misreconstructed momenta. Finally, the water must be radioisotope-free as gamma-rays from radioactivity can mimic the signal of a low energy neutrino event. To keep these contaminants low, Super-K uses a multi-step water purification system including filtration, reverse osmosis (RO), and degasification. Additionally, to help with the relatively high radon background present in the mine, the experimental hall is supplied with fresh air pumped in from a site outside the mine entrance.

The water in Super-K is continuously filtered at a rate of 30 tons/hour in a closed system. The water starts by passing through μm mesh filters that removes all large particles. It then passes through a heat exchanger to cool down the water to 12.9^o C. This both reduces PMT dark noise and suppresses the growth of bacteria. Any surviving bacteria are killed by a UV sterilizer stage.

The water continues on to a cartridge polisher (CP) that is used to eliminate any heavy ions, thus lowering the radioactivity even further. In total, 1500 L of CP resin is used. After the CP the typical resistivity of the water goes from 11 MΩcm to 18.24 MΩcm, approaching the chemical limit for water at 13^o C.

A RO system is then used to remove any additional particulates before moving on to a tank to dissolve radon reduced air into the water. The radon reduced air is dissolved in the water to increase the efficiency of radon removal during the vacuum degasifier stage. The vacuum degasifier removes any dissolved gas in the water, removing 96% of the radon gas and lowering the dissolved oxygen content, which can encourage bacterial growth, to 0.06 mg/L.

Finally, the water goes through an ultra filter and a membrane degasifier. The ultra filter can remove particles with diameters of about 10 nm and reduces the number of particles greater than 0.2 μm from 1000 particles/cc to just 6 particles/cc. The membrane degasifier is the last step before the water in circulated back into the Super-K tank and tries to remove any remaining gases in the water. After the membrane degasifier, the dissolved oxygen is reduced to only 0.3 mg/L and the rest of the radon is removed with a 83% efficiency [21].

As mentioned previously, radioactivity within the tank and experimental hall must be kept to a minimum to ensure no "fake" neutrino events are detected. The primary radioactive material of concern is naturally occurring radon from the mine. The typical radioactivity near the Super-K tank varies from 2000-3000 Bq/m^3 in the warm months to 100-300 Bq/m^3 during the winter. This seasonal variation is due to a chimney effect in the ventilation

system. During the cooler months, fresh air flows into the tunnel entrance and does not have to travel through much rock to reach the experimental hall. However, during the warm months, the air flows out of the tunnel entrance causing radon-rich air from deep within the mountain to travel through the experimental hall. To keep the radon levels as low as possible, an air purification system is used.

The air purification system consists of three compressors, a buffer tank, dryers, filters, and several activated charcoal filters. The last charcoal filters are cooled to -40^o C to increase the removal efficiency for radon. At the end of the purification cycle, the air contains only a few mBq/m^3 of radon. This air is used during the water purification as explained previously, for all space inside the Super-K tank, and in the experimental hall. The space between the top of the water and top of the tank, and the space around the Super-K tank (the dome) are kept at a slight over-pressure to help radon laden air from entering the detector. With this system, the radioactivity inside the dome can be kept below the required 100 Bq/m^3 and usually does not surpass 40 Bq/m^3. The radioactivity in the tank is typically much lower with recent readings being as low as a few mBq/m^3 [21].

4.4 Reconstruction

Event reconstruction at Super-K is performed using a program called APfit. The overall principle is that the PMT timing is used to find the event vertex, a Hough transformation algorithm is used to find the number of rings in the event, the particle identification (PID) of each ring is determined by its "fuzziness", and look-up tables are used to find the momentum based off of the total corrected charge measured. A brief overview of the reconstruction algorithms is described in this section, with more detailed descriptions described in [22] and [23].

4.4.1 Vertex Fitting

The vertex position is reconstructed by using the timing information of the PMTs, and is split up into three different steps. In the first step, the vertex position is estimated with the assumption that all the photons are emitted at the same time from a single point source. After subtracting the time of flight to each PMT, a distribution of residual PMT hit times is constructed. The test vertex is varied, and the residual timing distribution which best fits a Gaussian is selected as the event vertex.

In the second step, the direction and Cherenkov ring opening angle are

determined. A preliminary direction is computed by taking the vector sum of the vectors to each PMT, weighted by the PMT charge. By looking at the observed charge as a function of opening angle, the direction and open angle are then varied to find an optimal fit to the Cherenkov ring edge. In the final step, the results of the particle's direction and Cherenkov opening angle are used to refit the vertex, but this time the photons are assumed to be produced along the track of the particle.

4.4.2 Ring Counting

After the initial Cherenkov ring and vertex are determined, additional rings are searched for using a Hough transform technique [24]. A fixed vertex and Cherenkov opening angles of 42^o is assumed, and the PMT space is converted in to a (θ,ϕ) space. Peaks in this distribution correspond to different ring candidates, which are evaluated one at a time in order of their peak height. A likelihood for single ring case and a two ring case are constructed based off of the expected ring parameters and PMT charge. If the likelihood for the one ring case is better, the event is classified as a single ring event. However, if the likelihood for the two ring case is better, a second ring is considered found and the process is repeated again for a third ring. This will continue until up to five rings are found, at which point the the search is stopped.

4.4.3 Particle Identification

For each ring found, the ring will either be classified as e-like or μ-like based off of the charge pattern. Electrons, and gamma rays, produce a diffused "fuzzy" ring pattern due to electromagnetic showers and the fact low energy electrons undergo multiple scattering. Muons, and charged pions, produce rings with a sharp edge. Figure 4.2 shows an example event display for μ-like event (left) and an e-like event (right).

For single ring events, once the PID is known the vertex is refined once again. This new fit not only takes into account the timing information as done previously, but also the expected light patterns produced from either a e-like or μ-like event. The fit adjust the vertex position parallel to the particle direction and iterativly modifies the vertex and direction until a new best fit is found.

4.4.4 Momentum Reconstruction

The momentum of each particle is calculated by the total observed photo-electrons in the event. For multi-ring events, the charge pattern for each ring

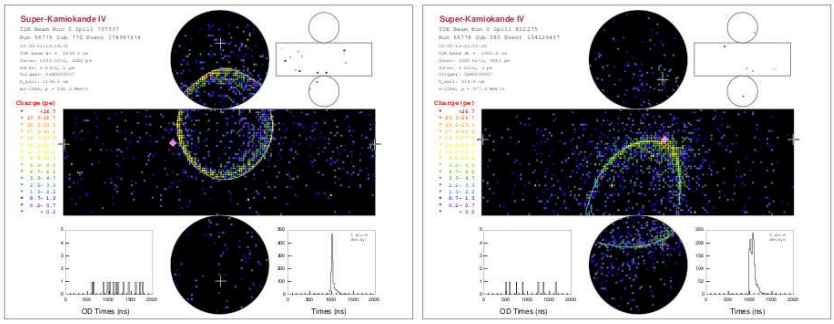

Figure 4.2: Example event displays for a μ-like event (left) and an e-like event (right). The displays show the cylindrical detector unrolled, with each color dot representing a PMT. The color shows the amount of charge while the crosses show the event vertex. Notice the crisp edge to the μ-like ring while the e-like event is more diffuse, or "fuzzy".

must first be separated in case any of the rings overlap. The total charge in each PMT is divided into a fraction from each ring based off of the expected charge distribution from each ring. The expected charge distribution is made assuming that the distribution of light should be uniform along the particles direction azimuthally and the charge is only a function of the opening angle.

Once the total charge for each ring is calculated, the charge is corrected for a number of effects. The light attenuation length, PMT acceptance as a function of angle, PMT gain, reflection off of PMTs, and water scattering are all used in the correction. As the PMT gain and water quality change over time, they are measured frequently with through going muons and energy scale calibration (please see 4.5 for more details.) The corrected charge is then simply converted to momentum based off of a look-up table produced with MC and verified with the energy-scale calibration.

4.5 Energy Scale Calibration

4.5.1 Decay Electrons

Electrons produced from the decay of muons are plentiful within the Super-K detector. They are useful for lower energy calibrations, ≈20-50 MeV/c, due to their well defined Michel spectrum [25]. Figure 4.3 shows the predicted Michel spectrum in red and the measured in black. The MC simulation takes into account effects from the nucleon Coulomb field caused by the atomic capture of the parent muon [26] and the μ^+/μ^- ratio of cosmic rays [27] along

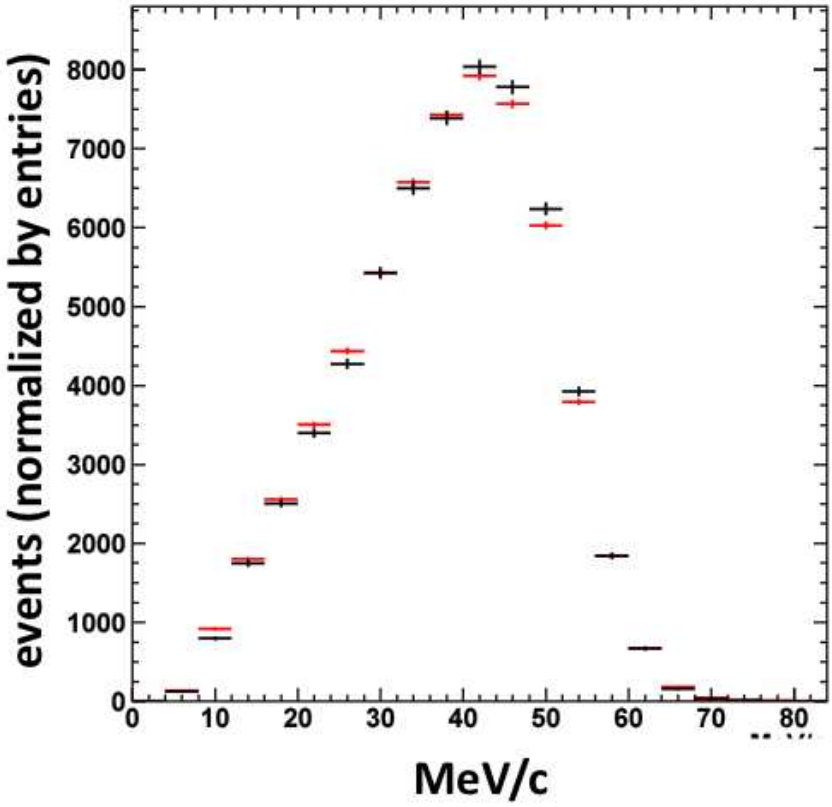

Figure 4.3: The Michel electron spectrum for SK-IV. The black histogram represents data while the red histogram is MC. The fitted peak of the spectrum is 37.96±0.05 MeV/c and 37.71±0.03 MeV/c for the data and MC, respectively, which corresponds to an error of -0.7±0.2%.

with the standard detector and water responses used in all MC. By comparing the mean of the two distributions, the error is calculated to be -0.7±0.2%.

4.5.2 Neutral Pions

When atmospheric neutrinos interact in Super-K via the weak neutral current, they often produce single π^0 in the final state. These interactions are another well calibrated source for the energy scale as the π^0's invariant mass can easily be reconstructed and is a well know quantity. The peak of both the data (black) and MC (red), as seen in Figure 4.4 are shifted to slightly higher values than the nominal 135 MeV/c^2 mostly due to de-excitation γs from the oxygen nucleus [21]. Difference in the mean of the data and MC is only 0.5±0.70% and the width of the distributions is similar showing there is good agreement

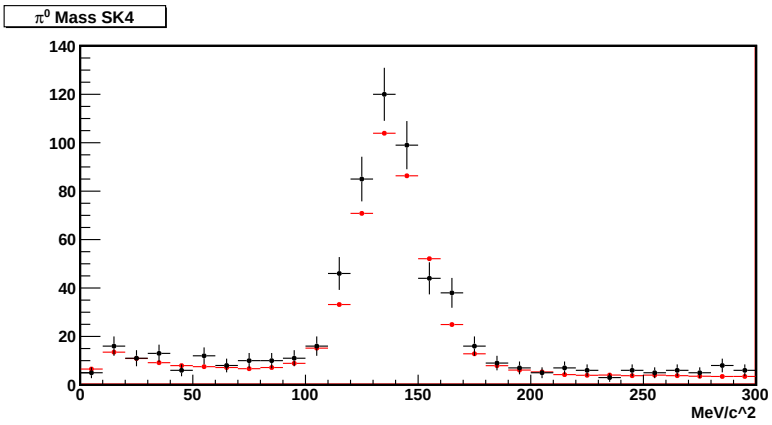

Figure 4.4: The reconstructed invariant π^0 mass. The black histogram represents data while the red histogram is MC. The fitted peak of the spectrum is 137.20±0.95 MeV/c and 137.92±0.08 MeV/c for the data and MC, respectively, which corresponds to an error of 0.52±0.70%.

in the two. Because this sample is from atmospheric neutrinos and not cosmic ray muons, it has the lowest statistics of all the energy scale samples.

As most single ring π^0 events that can be reconstructed have momenta less than 1 GeV. Also, as the momentum increases, the efficiency to tag single ring π^0s decreases. This is due primarily for two reasons. The first is that for highly boosted π^0s, symmetric decays results in a small opening angle. If the two Cherenkov rings overlap too much, they can appear as a single e-like ring instead of two e-like rings. The second reason is because when a highly asymmetric decay of a π^0 occurs, one of the rings can be too low in energy to be reconstructed. Taking into account the tagging efficiency and production rate, most of these events have a visible energy between 150-600 MeV.

4.5.3 Multi-GeV Stopping Muons

For multi-GeV cosmic muons (defined as 1.33 GeV/c for Super-K analysis) the total momentum is divided by the total path length. This gives a roughly constant value for all high energy muons in the Super-K tank and is equivalent to dE/dx, another well defined parameter [28]. The momentum is calculated in the typical manner and the total length traveled is calculated as the length from where the muon entered the tank to the vertex of its decay-electron. The sample is split up into six different total path lengths, and the results can be seen in Figure 4.5. The data MC agreement is roughly the same across all bins, ranging from -0.2±0.3% for the lowest error and 1.3±0.3% for the

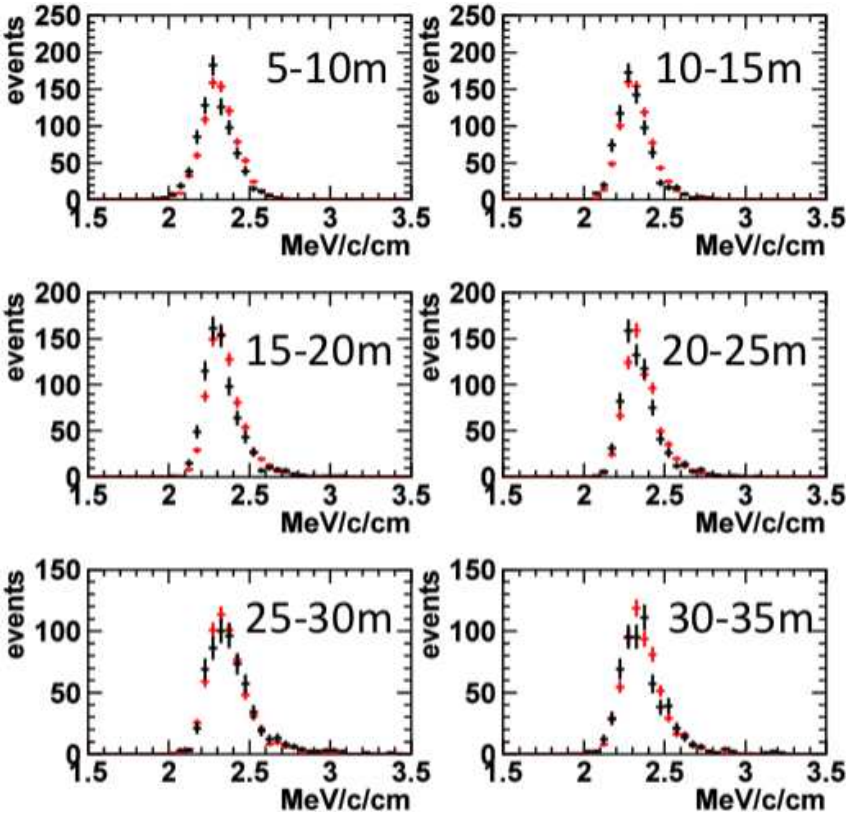

Figure 4.5: The multi-GeV stopping muon sample during SK-IV for six different ranges. The black histograms represents data while the red histograms are MC. The largest error is from 5-10 meter range with an error of 1.3±0.3%

highest error.

4.5.4 Sub-GeV Stopping Muons

The same method used for the energy-scale calculation at high energy cannot be used for lower energy stopping muons. This is because the vertex resolution inside Super-K tanks FV is only about 20-30 cm. For sub-GeV stopping muons, those less than 440 MeV/c, the maximum travel length in the tank is only 3 meters with most being much shorter. This means even small errors in the vertex reconstruction can lead to large errors in the energy-scale. Because of this, the sub-GeV stopping muon sample must use some other rubric to calculate the energy-scale error. In this case we use its Cherenkov opening angle.

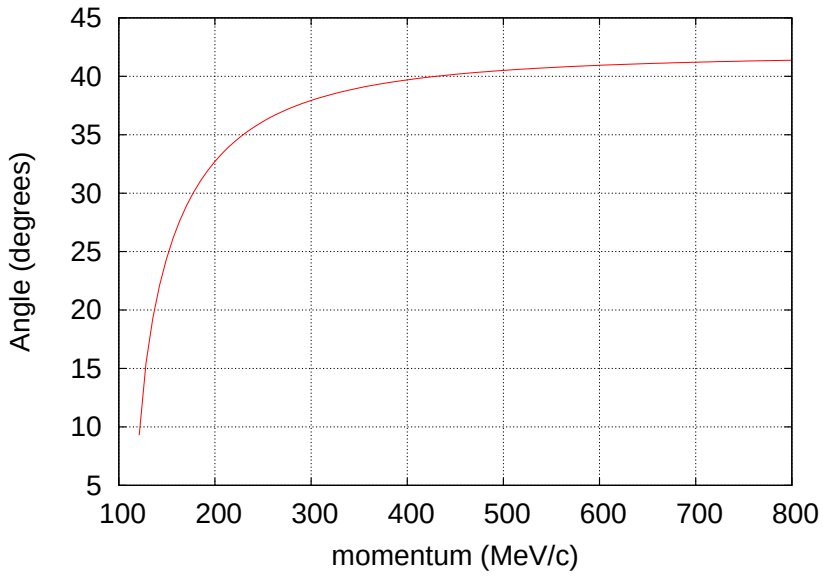

Figure 4.6: This figure shows the Cherenkov opening angle as a function of the muons momentum. Notice that for higher momenta muons, the opening angle approached 42^o.

The Cherenkov opening angle is defined as

$$\cos(\theta_c) = -\frac{1}{\beta n} \tag{4.1}$$

where θ_c is the Cherenkov angle, n is the index of refraction, and β is defined as

$$\beta = \frac{1}{\sqrt{1 + \frac{m^2}{p^2}}} \tag{4.2}$$

where m is the mass of the charged particle and p is its momentum. By plugging Equation 4.2 into Equation 4.1 and solving for p we get

$$p(\theta_c) = \frac{m}{\sqrt{\cos^2(\theta_c)n^2 - 1}} \tag{4.3}$$

Now we have a way to calculate the momentum only using the Chernekov opening angle. The results of Equation 4.3 can be seen in Figure 4.6 for n=1.33, the index of refraction for pure water, and m=105.7 MeV/c^2, the mass of the muon.

As can be seen in Figure 4.6, for high momentum muons, the Cherenkov

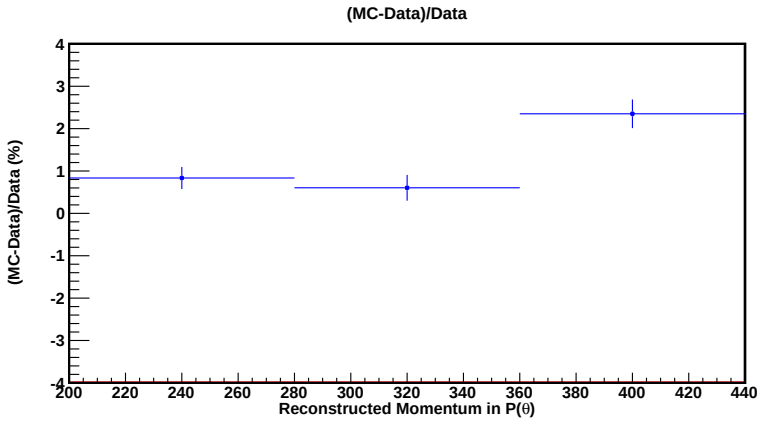

Figure 4.7: The sub-GeV stopping muon sample during SK-IV for three different momentum ranges. This sample has the largest error of all energy-scale samples at 2.3±0.3%.

angle is roughly constant and approaches ≈42^o. This, along with the cutoff momentum for muons to Cherenkov, sets the momentum range for this study to 200-440 MeV/c. Unlike the other studies mentioned so far, this one uses a double ratio to calculate the energy-scale error. This is because there is slight bias in the Cherenkov angle reconstruction. By taking the ratio of the momentum reconstructed from charge and the momentum reconstructed from the Chernekov angle for both data and MC, and than taking the ratio of these ratios, the systematic shift the Cherenkov angle reconstruction can be canceled out. Figure 4.7 shows the results for the sub-GeV stopping muon sample that is split up into three bins. The max error for this study is 2.4±0.3% and has the largest error of all the energy-scale samples.

4.5.5 Time Variation

Apart from just measuring the error on the momentum reconstruction, the time variation is also studied. The multi-GeV stopping muon sample and decay-electron sample both have large enough statistics to be checked on a daily basis. Figure 4.8 shows the change in these two studies over time. Each bin roughly corresponds to 10 days worth of a data. The time variation itself is calculated by taking the RMS/mean for each sample. Overall, the energy-scale has been very stable during SK-IV with a variation of only 0.4%.

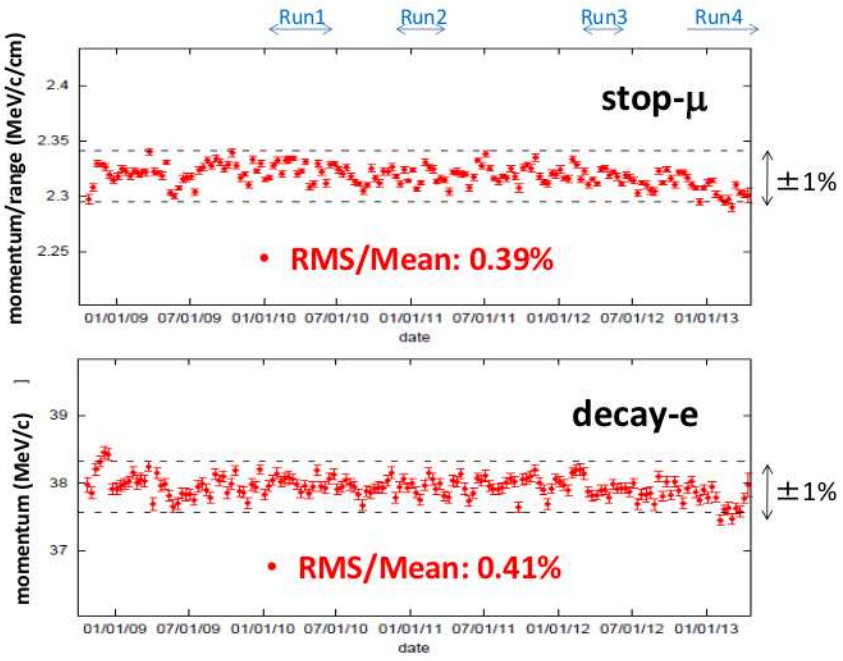

Figure 4.8: These figures represent the time variation of the energy-scale since the beginning of SK-IV. The top figure is for the multi-GeV stopping muon sample while the bottom is for the decay-electron sample. The ±1% lines are shown as dashed black lines and the different T2K run periods are labeled on top. All together the energy-scale has a time variation of 0.4%.

4.5.6 Absolute Energy Scale

The purpose of the absolute energy-scale is to try and keep the data and MC matching with each other along with matching well know quantities like the π^0 mass. If the data and MC do not agree, several steps can be taken to rectify the situation. For instance, a general scaling factor for all energies can be applied or the global PMT gain can be adjusted. If there is severe disagreement, the MC photon production rate can be changed, usually by adding in a new physics process that was not taken into account before.

The systematic error due to the energy-scale is calculated in a very conservative manner. The study with the highest error is added in quadrature with the time variation of the energy scale. This number is than used for all systematic error calculations that include momentum and energy reconstruction. For SK-IV this error is calculated to be 2.4%. All the results from the energy scale studies are summarized in Figure 6.3 and each study is color coded for easy readability.

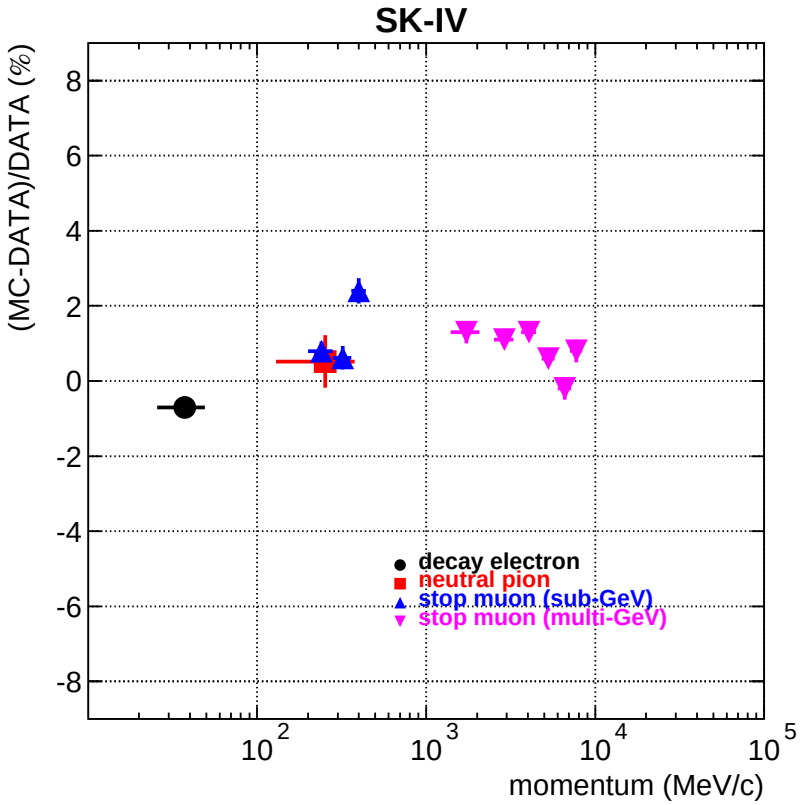

Figure 4.9: This figure shows the absolute energy scale error for all of SK-IV. The black dot shows the decay-electron sample, the red square shows the π^0 invariant mass, the blue triangles show the sub-GeV stopping muon sample, and the magenta upside down triangles is the multi-GeV stopping muon sample. Using these results along with those of the time variation, the absolute energy scale error is calculated to be 2.4%.

Chapter 5

Analysis Method

This analysis uses both the number and spectrum shape of candidate events selected by a predetermined criteria. The method was developed for the 2012a result using Run1+2+3b+3c [1] and we optimized the analysis and error inputs for Run1-4 data in 2013.

At first, the ν_e candidate events are divided into 25 bins with a 50 MeV range for each, and a probability density function (PDF) is constructed for ν_e appearance signal and others. A likelihood is defined using the number of ν_e events in each E^{rec} bin and the best-fit point of θ_{13} is obtained by searching for a maximum likelihood alongside of θ_{13} with varying systematic uncertainties, a so-called extended maximum likelihood fit. The systematic uncertainty considers the following sources: flux and cross section according to past experiments, normalization, interaction uncertainties and so on by the near detector measurement and selection uncertainties at Super-K detector. To obtain a confidence level (CL), a delta of the negative log likelihood curve is calculated as a function of θ_{13} and its width is taken. A sensitivity of the θ_{13} measurement is calculated by taking the average of many toy Monte Carlo (MC) generations. The ν_e appearance significance is evaluated by p-value based on Feldman-Cousins method, where an observation of the ν_e appearance candidate is compared with many toy experiments assuming $\theta_{13} = 0$ [29]. An essential part of this analysis is to improve the sensitivity by separating the ν_e signal from backgrounds using the difference of their E^{rec} spectrum shape, depending on neutrino oscillation parameters. This section describes how to construct the likelihood for the fit.

For the selected ν_e candidate events, assuming quasi-elastic (QE) kinematics, a common binding energy for all the nucleons, and neglecting Fermi

motion, the neutrino energy is reconstructed as

$$E^{rec} = \frac{m_p^2 - (m_n - E_b)^2 - m_e^2 + 2(m_n - E_b)E_e}{2(m_n - E_b - E_e + p_e \cos\theta_e)}, \tag{5.1}$$

where m_p is the proton mass, m_n the neutron mass, and $E_b = 27\,\mathrm{MeV}$ is the binding energy of a nucleon inside a ^{16}O nucleus [1]. E_e, p_e, and θ_e are the reconstructed electron energy, momentum, and angle with respect to the beam direction, respectively.

5.1 Data set of Super-K MC samples

The MC expectation in this analysis is calculated using the Super-K MC set that use the standard Super-K reconstruction alogrithms and the new π^0 algorithm fiTQun. This MC set is composed of the ν_μ, $\overline{\nu}_\mu$, ν_e, $\overline{\nu}_e$ background MC, and $\nu_\mu \rightarrow \nu_e$ signal MC which was produced by using the ν_μ flux and ν_e interaction cross section. The MC samples were generated with the flux predictions that were provided by the beam group, where the version is the same as the previous 2012a except for the Run4 tuning.

Table 5.1 summarizes the parameters used for calculating oscillation probability with three flavor mixing and matter effect. They are the default oscillation parameter values used for the studies presented in this dissertation. The θ_{12} parameter changed to use the value, $\sin^2 2\theta_{12} = 0.8495$[30], which was 0.8704 in 2012a analysis[31–33]. This value is obtained from a global fit including T2K using six ν_e appearance candidates and MINOS without reactor experiments (the Daya Bay and RENO) in the 3-neutrino oscillation parameters as quoted in the 2012 edition of Review of Particle Physics[12]. A recent result of the global fit shows 0.8510[34] and is mostly consistent with the above value.

5.2 Definition of the likelihood

The same likelihood definition is repeated as used in the 2012a analysis. The likelihood is defined as

$$\mathcal{L}(N_{obs}, \boldsymbol{E}^{rec}_{obs}; \boldsymbol{\theta}, \boldsymbol{f}) = \mathcal{L}_{norm}(N_{obs}; \boldsymbol{\theta}, \boldsymbol{f}) \times \mathcal{L}_{shape}(\boldsymbol{E}^{rec}_{obs}; \boldsymbol{\theta}, \boldsymbol{f}) \times \mathcal{L}_{syst}(\boldsymbol{f}), \tag{5.2}$$

[1] The uncertainty on binding energy is not considered in the E^{rec} calculation. This should not affect the analysis results significantly, since the same equation is used for observed events and MC events.

Table 5.1: Default neutrino oscillation parameters and earth matter density used for the MC prediction.

Parameter	Value	
Δm^2_{21}	7.6×10^{-5} eV^2	
Δm^2_{32}	2.4×10^{-3} eV^2	
$\sin^2 2\theta_{12}$	0.8495	($\sin^2\theta_{12} = 0.306$)
$\sin^2 2\theta_{23}$	1.0	($\sin^2\theta_{23} = 0.5$)
$\delta_{\rm CP}$	0 degree	
Mass hierarchy	Normal	
ν travel length	295 km	
Earth matter density	2.6 g/cm^3	

where N_{obs} and $\boldsymbol{E}^{rec}_{obs}$ are, respectively, the number of observed ν_e candidate events and their reconstructed neutrino energies, $\boldsymbol{\theta}$ are the neutrino oscillation parameters to be extracted, and $\boldsymbol{f}$ are the parameters representing systematic uncertainties on the prediction (called "systematic parameters" in this dissertation).

The first term of equation (5.2), $\mathcal{L}_{norm}$, is the normalization likelihood defined as a Poisson probability to observe N_{obs} candidate events:

$$\mathcal{L}_{norm}(N_{obs};\boldsymbol{\theta},\boldsymbol{f}) = \frac{e^{-N_{exp}(\boldsymbol{\theta},\boldsymbol{f})}[N_{exp}(\boldsymbol{\theta},\boldsymbol{f})]^{N_{obs}}}{N_{obs}!}, \tag{5.3}$$

where $N_{exp}(\boldsymbol{\theta},\boldsymbol{f})$ is the expected number of events which depends on oscillation parameters and systematic parameters.

The second term, $\mathcal{L}_{shape}$, is the shape likelihood defined as the product of probabilities that each event has the observed reconstructed neutrino energy:

$$\mathcal{L}_{shape}(\boldsymbol{E}^{rec}_{obs};\boldsymbol{\theta},\boldsymbol{f}) = \prod_{i=1}^{N_{obs}} \rho(E^{rec}_{obs,i};E^{rec},\boldsymbol{\theta},\boldsymbol{f}), \tag{5.4}$$

where ρ is the probability density function (PDF) of the reconstructed neutrino energy. The PDF ρ is produced for given oscillation parameters and systematic parameters. The calculation of ρ and N_{exp} is described in detail in Section .

The third term, $\mathcal{L}_{syst}$, is the probability density function of the systematic

parameters. A multivariate normal distribution is used :

$$\mathcal{L}_{syst}(\boldsymbol{f}) = \frac{1}{(2\pi)^{k/2}\sqrt{|V|}} \exp\left(-\frac{1}{2}\Delta\boldsymbol{f}^{\top}V^{-1}\Delta\boldsymbol{f}\right), \tag{5.5}$$

where k is the number of systematic parameters, V is the covariance matrix of systematic parameters, and $\Delta\boldsymbol{f}$ are the deviations of systematic parameters from their nominal values.

5.3 Prediction of ν_e candidate spectrum

For given oscillation and systematic parameters, the E^{rec} distribution of ν_e candidate events is predicted in the form of a histogram with 50 MeV/binning (25 bins from 0 GeV to 1.25 GeV). The number of events in each E^{rec} bin is calculated as:

$$N_{exp}(E^{rec},\boldsymbol{\theta},\boldsymbol{f}) = f^{e-scale}(E^{rec})\sum_{k=1}^{5}\sum_{i=1}^{7}\Bigg[f^{SK}(F_k,I_i,E^{rec}) \times \sum_{j=1}^{N_{etrue}} f^{beam}(F_k,E_j)f^{xsec}(F_k,I_i,E^{rec},E_j)N^{osc}(F_k,I_i,E^{rec},E_j,\boldsymbol{\theta})\Bigg], \tag{5.6}$$

where

F: Neutrino flavor category. There are five categories : k =ν_e signal, ν_μ background, $\overline{\nu}_\mu$ background, ν_e background, and $\overline{\nu}_e$ background.

I: Neutrino interaction category. Interactions are classified into 7 groups : i =CCQE, CC1π, CC coherent, CC others, NC1π^0, NC coherent, NC1$\pi^{\pm}$+NC others.

E_j: True neutrino energy. Super-K MC samples were generated in the range from 0 GeV to 30 GeV. The binning of true neutrino energy is determined to fit with binnings of beam flux and cross section uncertainties, which are described in the next section (cf. Table 6.2). Therefore, the true energy binning is different among flavor categories.

N^{osc}: The expected number of events in the (E^{rec}, E_j) bin with oscillations calculated by the default Super-K MC. For given oscillation parameters, N^{osc} is calculated in advance of likelihood calculation by looping over all the Super-K MC events and reweighting them event-by-event with the following oscillation probabilities :

- $\nu_\mu \rightarrow \nu_e$ oscillation probability for ν_e CC signal,
- $\nu_\mu \rightarrow \nu_\mu$ survival probability for ν_μ CC background,
- $\overline{\nu}_\mu \rightarrow \overline{\nu}_\mu$ survival probability for $\overline{\nu}_\mu$ CC background,
- $\nu_e \rightarrow \nu_e$ survival probability for ν_e CC background, and
- $\overline{\nu}_e \rightarrow \overline{\nu}_e$ survival probability for $\overline{\nu}_e$ CC background.

The NC events in the background MC samples are not reweighted by oscillations and NC events in the signal ν_e MC are not used. These oscillation probabilities are calculated by the `Prob3++` library in the three flavor neutrino framework including the matter effect[35].

f^{beam}: Systematic parameters for beam flux uncertainty.

f^{xsec}: Systematic parameters for neutrino interaction cross section.

f^{SK}: Systematic parameters for Super-K detector efficiency uncertainty except for the energy scale error. The uncertainty on final state interactions (FSI), pion hadronic secondary interactions in Super-K (SI) and photonuclear effect (PN) is also incorporated.

$f^{e-scale}$: Systematic parameter for Super-K energy scale uncertainty.

Details of systematic parameters (f^{beam}, f^{xsec}, f^{SK}, and $f^{e-scale}$) are described in section 6.

The total number of events, $N_{exp}(\boldsymbol{\theta}, \boldsymbol{f})$ in Equation (5.3), is calculated by integrating the predicted E^{rec} distribution: [2]

$$N_{exp}(\boldsymbol{\theta}, \boldsymbol{f}) = \int N_{exp}(E^{rec}, \boldsymbol{\theta}, \boldsymbol{f})\ dE^{rec}, \tag{5.7}$$

and the PDF of the reconstructed neutrino energy spectrum in equation (5.4) is defined as a normalized E^{rec} distribution:

$$\rho(E^{rec}, \boldsymbol{\theta}, \boldsymbol{f}) = \frac{N_{exp}(E^{rec}, \boldsymbol{\theta}, \boldsymbol{f})}{N_{exp}(\boldsymbol{\theta}, \boldsymbol{f})}. \tag{5.8}$$

[2]Though the equation is described in a form of integral, the total number of events, $N_{exp}(\boldsymbol{\theta}, \boldsymbol{f})$, is just the sum of number of events in each E^{rec} bin, $N_{exp}(E^{rec}, \boldsymbol{\theta}, \boldsymbol{f})$.

5.4 Extraction of oscillation parameters

At each oscillation parameter point, the likelihood $\mathcal{L}(\boldsymbol{\theta}, \boldsymbol{f})$ is maximized by varying the systematic parameters $\boldsymbol{f}$. In practice, a negative log likelihood $-2\ln\mathcal{L}(\boldsymbol{\theta}, \boldsymbol{f})$ is minimized with respect to vartion of $\boldsymbol{f}$. The Minuit2 package is employed for the minimization. Then, the best-fit oscillation parameter point which gives the global minimum of $-2\ln\mathcal{L}(\boldsymbol{\theta})$ is searched for. Thus, the systematic parameters $\boldsymbol{f}$ work as nuisance parameters in the fit. The difference from the global minimum is calculated (described as $-2\Delta\ln\mathcal{L}$ in this dissertation) and used for extracting allowed regions of oscillation parameters at a certain confidence level.

Most of the studies in this disertation are done with a one dimensional scan, where only $\sin^2 2\theta_{13}$ is scanned and the other oscillation parameters are fixed. In a one dimensional scan, confidence intervals at 68 % C.L. and 90 % C.L. are determined by $-2\Delta\ln\mathcal{L} < 1.00$ and < 2.71, respectively.

Chapter 6

Systematic Errors

6.1 Inputs to neutrino oscillation analysis

The systematic uncertainty on the expected number of ν_e candidate events and the reconstructed neutrino energy spectrum is introduced into the likelihood calculation via systematic parameters, f^{beam}, f^{xsec}, f^{SK}, and $f^{e-scale}$, as shown in Equation (5.6). Each of these reweighting parameters is further sub-divided into basic systematic parameters listed in Table 6.1. Since the 2012a analysis, 1π E_ν shape error is merged into the ND280 fit result and therefore removed from one of the response functions. In the SK error, there is one bin for π^0 selected sample and two bins for a high E^{rec} region above 1250 MeV for each mode of four interactions, but these errors are not used in this analysis and keep the same binning as used in the 2012a. In total, 49 systematic parameters are used in this analysis.

Among the 49 systematic parameters, all the beam flux parameters and some of the ν interaction cross section parameters are extrapolated from the ND280 fit result[36][37]. The extrapolation method has been studied by the Beam And ND280 Flux measurement task Force (BANFF), and these parameters are called "BANFF parameters" in this dissertation. The initial values of BANFF systematic parameters prior to the likelihood fit are determined by the ND280 data fit as well as their errors and correlation. The rest of the systematic parameters give no correlation between the ND280 data fit and the SK data oscillation fit.

6.1.1 Beam flux systematics

As described in section 5.1, the default SK MC expectation is based on the 11b tuned version 3.2 flux model. The beam flux systematic uncertainty is

Table 6.1: Systematic parameters in the likelihood calculation. The SK efficiency errors, FSI+SI and PN errors are summed in quadrature and represented by common systematic parameters (indicated by *). Therefore, total number of systematic errors is $22 + 5 + 9 + 12 + 1 = 49$.

Category	Systematic parameter		# of params
Beam flux	Flux normalization		22
ν interaction	(SK/ND corr.)	M_A^{QE}, M_A^{RES}, CCQE norm, CC1π norm, and NC1π^0 norm	5
	(SK/ND uncorr.)	CC other shape, Spectral function, p_F, $\sigma_{\nu_e}/\sigma_{\nu_\mu}$, W shape, etc.	9
SK detector	Detector efficiency		12*
	Energy scale		1
FSI + SI	FSI and π hadronic secondary interactions in SK		12*
PN	Photonuclear effect		12*

simply described by normalization parameters to this 11b-v3.2 flux in bins of true neutrino energy and flavor. The binning for the SK flux systematic parameters summarized in Table 6.2 is determined by the BANFF working group.

Table 6.2: The binning of the systematic parameters for the beam flux uncertainty at SK. Note that the ν_e oscillation signal MC is produced using ν_μ flux and reweighted by ν_μ flux systematic parameters (11 bins). (This table is identical to Table 4 of T2K-TN-109.)

Flavor	Binning (GeV)	# of bins
ν_μ	0-0.4, 0.4-0.5, 0.5-0.6, 0.6-0.7, 0.7-1.0, 1.0-1.5, 1.5-2.5, 2.5-3.5, 3.5-5.0, 5.0-7.0, 7.0-30.0	11
$\overline{\nu}_\mu$	0-1.5, 1.5-30.0	2
ν_e	0-0.5, 0.5-0.7, 0.7-0.8, 0.8-1.5, 1.5-2.5, 2.5-4.0, 4.0-30.0	7
$\overline{\nu}_e$	0-2.5, 2.5-30.0	2

The beam flux uncertainty is initially constrained by a series of external and in-situ measurements such as proton beam monitor measurements and NA61 hadron production measurements.

6.1.2 Cross section systematics

Neutrino cross section parametrization for the 2013a oscillation analysis has been studied by the Neutrino Interaction Working Group (NIWG)[39]. As previously described, cross section systematic parameters in this analysis are classified into two groups. One of them is a group of the cross section parameters constrained by the ND280 data fit prior to the oscillation fit. This group consists of the 5 systematic parameters: M_A^{QE}, M_A^{RES}, normalizations for CCQE, CC1π and NC1π^0 interactions, as listed in Table 6.3. There are expected to be partial error cancellations between ND280 and SK for these parameters. The prior values, errors and covariances of these parameters are provided by the BANFF as the results of the ND280 data fit. The other group includes the parameters uncorrelated with any parameters. There are 9 such parameters as listed in Table 6.4, that is, cross section shape of CC other interactions, spectral function [1], Fermi momentum (p_F), overall normalizations of CC/NC coherent and NC other interactions, cross section ratio of ν_eCC to ν_μCC, W shape, and Pionless delta decay. Thus, a total of 14 systematic parameters are used for an implementation of cross section uncertainty into the likelihood calculation.

[1]NEUT uses a Relativistic Fermi Gas model for the nuclear potential. A more complicated model of the nuclear potential is called the "spectral function". The difference between the two models is taken as a $+1\sigma$ error. The response for this systematic parameter is calculated by extrapolating from the 0 and $+1\sigma$ weights.

Table 6.3: Summary of the BANFF systematic parameters. The results of the ND280 fit (Post ND280 fit) are used as prior values and errors for the oscillation fit.

Parameter	Pre ND280 fit		Post ND280 fit		# of params
	Value	Error	Value	Error	
Flux	1	$0.09 \sim 0.19$	$0.93 \sim 1.05$	$0.06 \sim 0.18$	22
(@ osc max.)		($\sim$0.12)	($\sim$0.98)	($\sim$0.08)	
M_A^{QE} (GeV)	1.21	0.45	1.24	0.07	1
M_A^{RES} (GeV)	1.41	0.22	0.96	0.07	1
CCQE norm	1	0.11	0.97	0.08	1
CC1π norm	1.15	0.32	1.26	0.16	1
NC1π^0 norm	0.96	0.33	1.14	0.25	1

Table 6.4: Summary of the neutrino interaction cross section systematic parameters other than the BANFF parameters. These parameters can be varied in the oscillation fit independently of the ND280 data. The values are the same as in the ones in the 2012a analysis.

Parameter	Prior value	Prior error	# of params
CC other shape (GeV)	0	0.4	1
Spectral function	0 (off)	1 (on)	1
p_F (MeV)	225	30	1
CC coherent norm	1	1	1
NC coherent norm	1	0.3	1
NC1$\pi^{\pm}$+NC other norm	1	0.3	1
$\sigma_{\nu_e \mathrm{CC}}/\sigma_{\nu_\mu \mathrm{CC}}$	1	0.03	1
W shape (MeV)	87.7	45.3	1
Pionless delta decay	0.2	0.2	1

Among these cross section systematic parameters, 6 normalization parameters (labeled $\sim$ norm in Tables 6.3 and 6.4) and the $\sigma_{\nu_e \mathrm{CC}}/\sigma_{\nu_\mu \mathrm{CC}}$ parameter work as simple reweighting factors for a specific interaction category or flavor category. The CCQE (CC1π) normalization parameter reweights only bins in $E_\nu < 1.5$ (2.5) GeV, while the other normalization parameters (NC1π^0, CC coherent, NC coherent, and NC1$\pi^{\pm}$+NC other) are applied in the whole energy range. In fact, there are three additional normalization parameters ($1.5 < E_\nu < 3.5$ GeV and $E_\nu > 3.5$ GeV for CCQE, and $E_\nu > 2.5$ GeV for CC1π) which are used in the ND280 data fit, but these parameters have a negligible impact on the ν_e analysis so are therefore ignored. The cross section ratio parameter $\sigma_{\nu_e \mathrm{CC}}/\sigma_{\nu_\mu \mathrm{CC}}$ changes overall normalizations of ν_e CC signal, ν_e background, and $\overline{\nu}_e$ background.

The other parameters, i.e. M_A^{QE}, M_A^{RES}, CC other shape, Spectral function, p_F, W shape and Pionless delta decay, can change the cross section in a non-trivial way. These uncertainties are represented by response functions, which provide the fractional change in a given bin under a change to a cross section parameter.

In practice, the effect of the bin is calculated by an event-by-event reweighting, first for 7 points, corresponding to $(-3\sigma, -2\sigma, -1\sigma, 0\sigma, +1\sigma, +2\sigma, +3\sigma)$ variations of each parameter. Then, for an arbitrary change to the parameter, a spline function through the 7 calculated points is used.

For each cross section systematic parameter, such a spline response function is made for bins of flavor category, interaction category, true neutrino energy,

and reconstructed neutrino energy. The binning for response functions in true neutrino energy is identical to that for flux systematic parameters described in Table 6.2 with the exception that the ν_e signal binning is common to the ν_e background, not to the ν_μ background. The binning in reconstructed neutrino energy is the same as that of the PDF in the likelihood, namely 50 MeV/bin. As an example, a spline response function for M_A^{QE} variation representing the relative weight for one of (E_ν, E^{rec}) bins in the signal ν_e CCQE event category is shown in Figure 6.1.

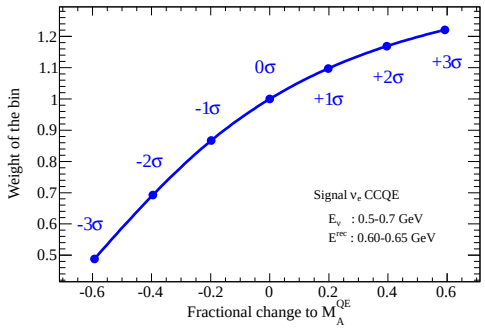

Figure 6.1: An example spline response function, E_ν^{rec} distributions of signal ν_e CCQE.

The response function for the W shape systematic parameter is calculated in a different way. This parameter is introduced to provide a way to modify the shape of the pion momentum distribution in resonance interactions. The 1σ error of the W shape parameter derived from a fit to the MiniBooNE NC1π^0 spectrum [40] is rather large, and the responses under a 2σ or 3σ change to the parameter cannot be estimated reasonably by an event-by-event reweighting. Actually, under a -2σ or more negative change, the parameter value becomes negative and it is impossible to reweight an event. Therefore, the response under a positive change of the W shape parameter is given by a linear interpolation and extrapolation through the 0σ and $+1\sigma$ points, while the response under a negative change is calculated by a linear interpolation and extrapolation through the 0σ and -1σ points.

The Pionless delta decay (PDD) and $1\pi\, E_\nu$ shape parameters are implemented in the final 2012a analysis, but the $1\pi\, E_\nu$ shape error is removed because BANFF considers it in other errors (M_A^{RES}, CC1π norm) accompanied with the BANFF error update. In NEUT, 20 % of all Δ may decay to produce no pions. The changes in the prediction when reducing the fraction of Δ which can decay with no pions from 20 % to 0 % are defined as a $+1\sigma$ response of the PDD systematic parameter. This response is given in the same way as the

W shape error (linear interpolation and extrapolation through the 0σ and 1σ points).

6.1.3 SK detector systematics

The systematic uncertainty on the SK detector efficiency has been provided from the T2K-SK group [41, 42]. Among all criteria for selection of T2K ν_e candidate events, the number of rings, PID and π^0 rejection cuts are the primary sources of the uncertainty. There are two sets of these errors because a new π^0 rejection criteria (fiTQun) is ready for this analysis as well as a POLfit π^0 cut used in past analyses. fiTQun also calculates the number of rings and PID, but the fiTQun reconstruction is applied only for the π^0 cut part in the ν_e candidate selection and the ring counting/PID parts use APfit with the default cut criteria. The SK detector error and ν_e candidate data set are provided for these two cut criteria called "(APfit +) fiTQun π^0 cut" and "APfit + POLfit π^0 cut, or APfit". The former selection and the error with fiTQun are used as a primary analysis in 2013, and the latter with POLfit is analyzed for a check on an equivalent analysis to the 2012a.

The ν_e selection by fiTQun using parameters of π^0 mass and likelihood parameters (a likelihood ratio of single-ring e-like to π^0 like) show a significant decrease of ν_μ background from 10% to 5% fraction in $\sin^2 2\theta_{13} = 0.1$, compared to the ν_e candidate using the cut by POLfit π^0 mass less than 105 MeV/c^2. Therefore, the use of fiTQun π^0 cut is expected to improve a result even if its error is comparable to or a little lager than that of POLfit π^0 cut.

The systematic uncertainty on these 3 cuts for ν_e CC events is estimated by using the SK atmospheric neutrino control sample [42], while the uncertainty for events accompanied by a π^0 is estimated using the hybrid π^0 control sample [41]. In order to evaluate dependence of the uncertainties on electron momentum and direction, these control samples are divided into 19 bins in (p_e, θ_{beam}) and compared between data and MC in each bin.

The 19 bins are composed of 5 momentum bins (100-300, 300-700, 700-1250, 1250-2000, 2000-5000 MeV/c), among which the first 2 momentum bins are divided into 7 bins in θ_{beam}, the highest two momentum bins are 1 bin, and the middle momentum bin (700-1250 MeV/c) is divided into 3 bins in θ_{beam}. For higher energy momentum region the scattering and multi-particle generation become large and the event statistic is low. Update from the 2012a is a fine binning between 700 and 5000 MeV/c, where 1 bin of that momentum region and 3 bins in θ_{beam} are used. Thus 2 bins are added to consider a possibility to include a high energy region above 1250 MeV E^{rec} . The two error sets were evaluated for the two new candidate selections of fiTQun π^0 cut and POLfit π^0 cut.

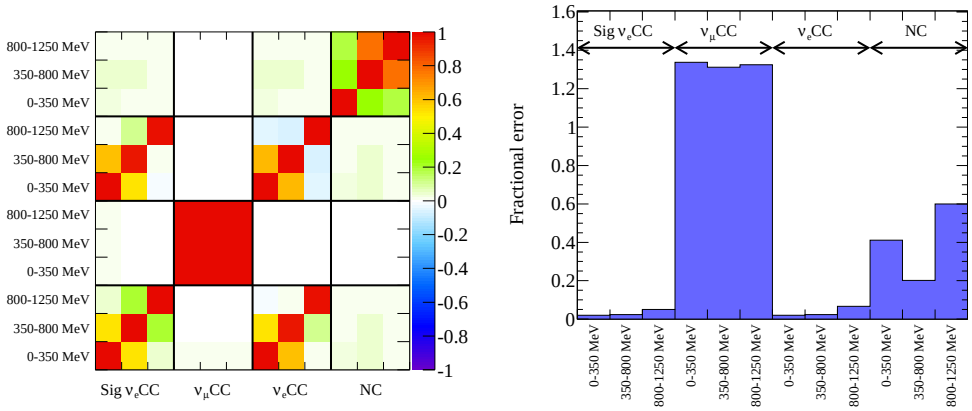

Figure 6.2: The correlation matrix (left) and diagonal fractional errors (right) of the SK detector systematic parameters with the fiTQun π^0 cut and adopted E^{rec} binning : 0-350, 350-800, 800-1250 MeV. The 2 bins above E^{rec} higher than 1250 MeV are also provided but not shown in the figures.

Then, all SK detector systematic errors on the T2K ν_e event selection except the energy scale error are compiled into a covariance matrix by utilizing a toy MC method [42]. This matrix gives the covariance of normalization parameters in bins of event category and reconstructed neutrino energy. In light of dependence on oscillation parameters, the systematic error is calculated for the following 4 event categories : ν_e CC signal, $\nu_\mu(\overline{\nu}_\mu)$ CC background, $\nu_e(\overline{\nu}_e)$ CC background, and NC.

The binning of the SK detector systematic parameter is chosen based on the study of binning optimization in the 2012a analysis as follows :

E^{rec} (MeV) : `0-350, 350-800, 800-1250`.

Figure 6.2 shows the size of correlation among bins and diagonal fractional errors, i.e. the square root of the diagonal elements from the covariance matrix, using the fiTQun π^0 cut. This matrix is an input into the oscillation analysis and gives the covariance of normalization parameters (f^{SK} in Equation (5.6)) in bins of event category and reconstructed neutrino energy.

The SK detector energy scale uncertainty is implemented into the likelihood calculation separately from the other detector efficiency uncertainties. Though $f^{e-scale}$ is described in Equation (5.6) as a single parameter just scaling the number of events in each bin, the uncertainty is implemented more correctly in reality. Figure 6.3 illustrates the actual method. The bin edges of the predicted reconstructed neutrino energy distribution are scaled by the energy scale systematic parameter $f^{e-scale}$, then the numbers of events gained from

and lost to other bins are computed by assuming that the event distribution inside a bin is flat. The 1σ error of this energy scale systematic parameter is updated from the 2012a oscillation analysis from 2.3 % to 2.4 %, taken from the error of the SK momentum scale.

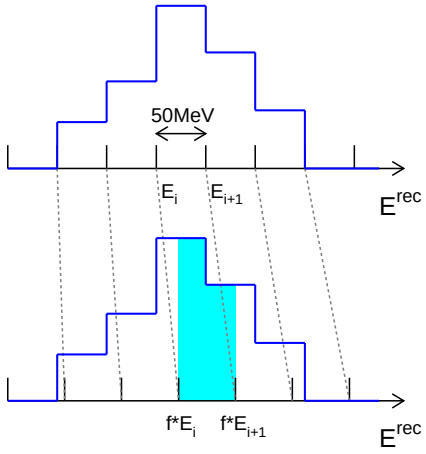

Figure 6.3: An illustration of the implementation of SK energy scale uncertainty. The blue portion in the bottom figure represents the entries in the i-th E^{rec} bin after scaling the energy scale by f.

Thus, the SK detector efficiency uncertainty is represented by the 13 systematic parameters, as summarized in Table 6.1.

6.1.4 Interaction systematics (FSI+SI and PN)

Uncertainty of final state interaction (FSI) The systematic uncertainty of the final state interaction (FSI) has been updated by the NIWG for the 2013a oscillation analysis [39].To propagate the uncertainties on several FSI modeling parameters to the oscillation analysis, the SK MC samples are reweighted. Then, a covariance matrix of the normalization parameters for reconstructed neutrino energy bins can be built. The FSI systematic uncertainty is implemented according to the same event categorization as that for the detector efficiency uncertainty.

Uncertainty of secondary interaction (SI) The systematic error due to uncertainty of the pion hadronic secondary interactions (SIs) in the SK

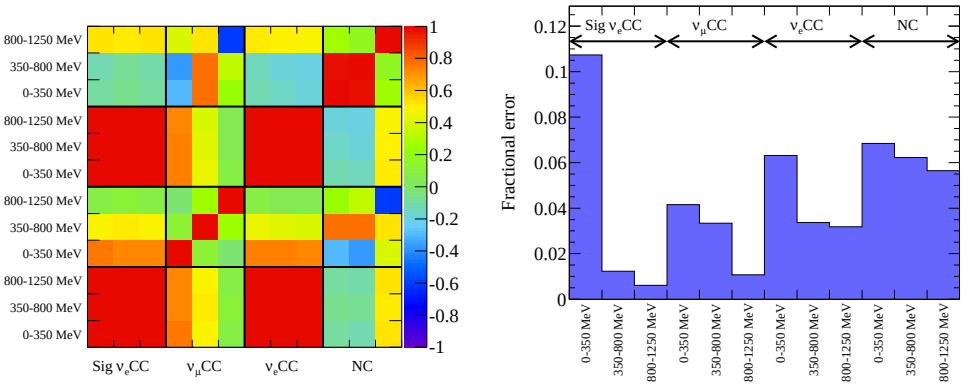

Figure 6.4: The correlation matrix (left) and diagonal fractional errors (right) of the FSI+SI systematic parameters using the fiTQun π^0 cut and adopted E^{rec} binning : 0-350, 350-800, 800-1250 MeV.

detector is estimated based on varying the interaction probabilities in the NEUT microscopic cascade model for pion interactions. To implement the correlation between the FSI and SI properly, the SK MC sample is reweighted by varying the FSI and SI parameters simultaneously, then the final covariance matrix is produced. Figure 6.4 shows the size of correlation among bins and the square root of diagonal elements of the covariance matrix for the FSI and SI uncertainty using the fiTQun π^0 cut.

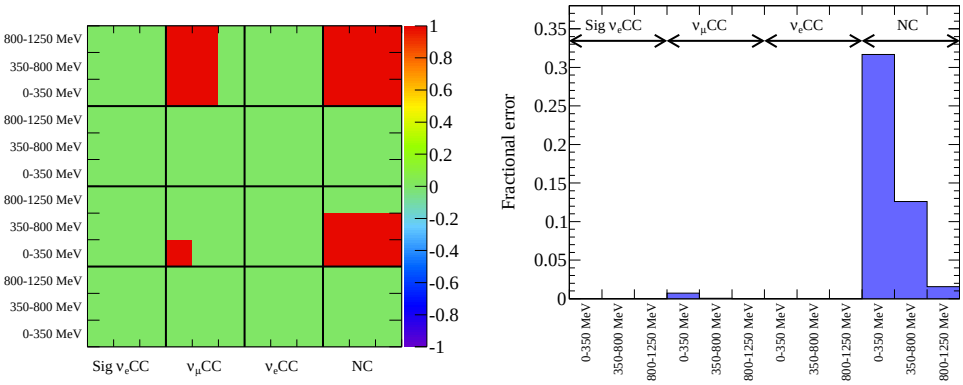

Figure 6.5: The correlation matrix (left) and diagonal fractional errors (right) of the PN systematic parameters using the fiTQun π^0 cut with the adopted E^{rec} binning : 0-350, 350-800, 800-1250 MeV.

Uncertainty of photonuclear interaction (PN) Photonuclear interactions are a mechanism in which a photon may interact prior to producing Cherenkov radiation [43]. These interactions in the SK detector are a potential error source on the prediction of NC1π^0 background. The matrix is made with the same binning as those for the SK detector and FSI+SI systematics. Figure 6.5 shows the size of correlation among bins and the square root of diagonal elements of the covariance matrix for the PN uncertainty using the fiTQun π^0 cut. As shown in the Table 6.5, the effect of photonuclear interactions are negligibly small for the moment. This systematics is newly implemented in the 2013a oscillation fit.

Since the systematic errors due to the SK detector efficiency, the FSI+SI and the PN share the same binning by common systematic parameters, all the three errors are added in quadrature (f^{SK} in Equation (5.6)). In practice, the three covariance matrices for the SK detector errors, the FSI+SI and PN errors are added linearly among the same bins, then the summed matrix is used as the covariance matrix of f^{SK}.

The systematic parameters for implementing the uncertainties of the SK detector efficiency, FSI, SI and PN are summarized in Table 6.5.

Table 6.5: Summary of the systematic parameters for the uncertainties of the SK detector efficiency, FSI and SI. These parameters can be varied in the oscillation fit independently of the ND280 data. Note that the SK efficiency error (other than the energy scale error), FSI+SI and PN error are summed in quadrature in each bin and represented by common systematic parameters (indicated by *).

Parameter	Prior value	Prior error		# of params
		fiTQun π^0	POLfit π^0	
SK detector efficiency	1	$0.020 \sim 1.34$	$0.020 \sim 1.29$	12*
SK energy scale	1	0.024		1
FSI+SI	1	$0.006 \sim 0.11$	$0.006 \sim 0.11$	12*
Photo-nuclear (PN)	1	$0.000 \sim 0.32$	$0.000 \sim 0.20$	12*

6.2 Summary of the systematic parameters

In summary, as listed in Table 6.6, a total of 49 parameters are introduced into the likelihood calculation for representing the systematic uncertainties and used as nuisance parameters in the oscillation fit. Figure 6.6 shows the size of correlation among bins and the square root of diagonal elements of the final covariance matrix (i.e. V in Equation (5.5)).

Table 6.6: List of all 49 systematic parameters used in the likelihood calculation. The parameters from No. 0 to No. 26 are so-called BANFF parameters. The results of the ND280 fit are used as prior values and errors in the oscillation fit. (* The systematic parameters for the binding energy uncertainty, E_b, and 1π E_ν shape were removed but these remain in the table to keep the present parameter numbering of the error inputs.) (** The systematic parameter for the SK efficiency has 20 bins in the provided matrix, where 8 of 20 bins are the high momentum bins larger than 1250 MeV and removed because these are not used in the analysis. The FSI+SI and PN error matrices have 24 total bins with 4 bins being the π^0 selected errors for NCπ^0 enriched (2-ring π^0). Only 12 bins are used for the analysis as the 8 high energy bins and the π^0 sample are removed.)

No.	Parameter	Pre ND280 fit		Post ND280 fit	
		Value	Error	Value	Error
0-21	Flux	1	$0.09 \sim 0.19$	$0.93 \sim 1.05$	$0.06 \sim 0.18$
22	M_A^{QE} (GeV)	1.21	0.45	1.24	0.07
23	M_A^{RES} (GeV)	1.41	0.22	0.96	0.07
24	CCQE norm ($E_\nu < 1.5\,\mathrm{GeV}$)	1	0.11	0.97	0.08
25	CC1π norm ($E_\nu < 2.5\,\mathrm{GeV}$)	1.15	0.32	1.26	0.16
26	NC1π^0 norm	0.96	0.33	1.14	0.25
27	CC other shape (GeV)	0	0.4	same as prefit	
28	Spectral function	0 (off)	1 (on)	same as prefit	
29	E_b (MeV)		REMOVED* in 2012		
30	p_F (MeV)	225	30	same as prefit	
31	CC coherent norm	1	1	same as prefit	
32	NC coherent norm	1	0.3	same as prefit	
33	NC1$\pi^\pm$+NC other norm	1	0.3	same as prefit	
34	$\sigma_{\nu_e\mathrm{CC}}/\sigma_{\nu_\mu\mathrm{CC}}$	1	0.03	same as prefit	
35	W shape (MeV)	87.7	45.3	same as prefit	
36	Pionless delta decay	0.2	0.2	same as prefit	
37	1π E_ν shape		REMOVED* in 2013		
38-49	SK eff. and FSI+SI+PN** fiTQun π^0 /(POLfit π^0)	1	$0.046 \sim 1.34$ /$(0.030 \sim 1.29)$	same as prefit	
50	SK energy scale	1	0.024	same as prefit	

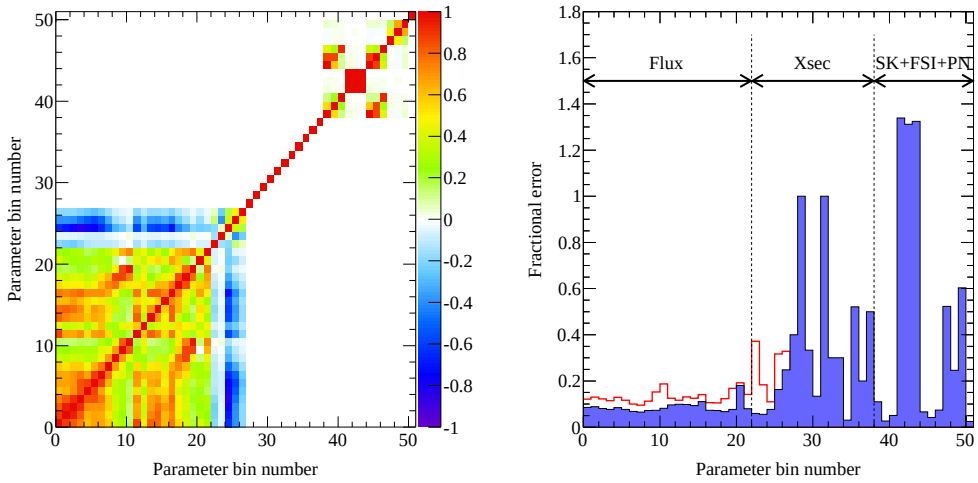

Figure 6.6: The correlation matrix (left) and diagonal fractional errors (right) of all systematic parameters for the likelihood calculation using the fiTQun π^0 cut. The red histogram in the right figure represents the fractional error size of the BANFF parameters (bin number 0-26) before the ND280 data fit.

Table 6.7 (6.8) give a comparison among the predicted numbers of ν_e candidate events using the fiTQun π^0 rejection (POLfit π^0 rejection) for the Run1-4 POT with the 3 different sets of systematic parameter values. The numbers are obtained using the prediction section of the oscillation fit program, which is based on Equations (5.6) and (5.7). The first set, "Nominal" in the table, uses the nominal values for all systematic parameters, and gives the prediction by the default 13a SK MC with the 11b tuned version 3.2 flux reweighting.

The second one, "Pre ND280 fit", uses the central values provided by the NIWG for some of the cross section systematic parameters. Specifically, M_A^{RES} ($1.21 \rightarrow 1.41$ GeV), CC1π normalization ($1 \rightarrow 1.15$), and NC1π^0 normalization ($1 \rightarrow 0.96$) is changed from the nominal values as a result of the fit to the MiniBooNE CC1π^0, CC1π^+ and NC1π^0 data (the fit is reconsidered after the 2012a analysis).

The last one, "Post ND280 fit", uses the best fit values from the ND280 data fit by the BANFF. Only the values of the BANFF parameters are different from the nominal or prefit values as shown in Table 6.6. The main reason of the decrease in the predicted number of events (10 % decrease in case of $\sin^2 2\theta_{13} = 0.1$, 13 % decrease in case of $\sin^2 2\theta_{13} = 0.0$) is the decrease of flux normalizations after the ND280 fit.

As can be seen in Table 6.7, fiTQun gives a lower number on the total expected events. This is mostly due to its ability to constrain NC background better than POLfit, especially in the ν_μ beam component.

Table 6.7: The predicted number of ν_e candidate events using the fiTQun π^0 rejection for the Run1-4 POT until May 8^{th}, 2013 (6.57×10^{20} POT) obtained by the likelihood calculation program (Equations (5.6) and (5.7)) with the 3 different sets of the systematic parameter values : "Nominal" by the default 13a SK MC with the 11b tuned version 3.2 flux reweighting, "Pre ND280 fit" using the NIWG central values for cross section systematic parameters, and "Post ND280 fit" using the fitted values by the BANFF.

$\sin^2 2\theta_{13} = 0.1$

	Nominal	Pre ND280 fit	Post ND280 fit
ν_e CC signal	17.8	18.4	17.3
ν_μ background	1.1	1.2	0.9
$\overline{\nu}_\mu$ background	0.1	0.1	0.1
ν_e background	3.1	3.4	3.1
$\overline{\nu}_e$ background	0.2	0.2	0.2
Total	22.3	23.2	21.6

$\sin^2 2\theta_{13} = 0.0$

	Nominal	Pre ND280 fit	Post ND280 fit
ν_e CC signal	0.4	0.4	0.4
ν_μ background	1.1	1.2	0.9
$\overline{\nu}_\mu$ background	0.1	0.1	0.1
ν_e background	3.4	3.6	3.4
$\overline{\nu}_e$ background	0.2	0.2	0.2
Total	5.1	5.5	4.9

6.3 Effect of systematic uncertainties

How much the systematic uncertainty affects the prediction is checked by throwing the systematic parameters. Specifically, a total of 20,000 sets of the systematic parameters following the multivariate normal distribution and covariance matrix are generated, and then the reconstructed neutrino energy distribution and total number of events are calculated for each set by using Equations (5.6) and (5.7). The central values of the systematic parameters in the multivariate normal distribution are set at the "Post ND280 fit" values. As for the error size and correlation among parameters, the covariance matrices both before and after the ND280 fit are tested for checking the improvement by the ND280 fit.

Table 6.8: The predicted number of ν_e candidate events using the POLfit π^0 rejection for the Run1-4 POT until May 8^{th}, 2013 (6.57×10^{20} POT) obtained by the likelihood calculation program (Equations (5.6) and (5.7)) with the 3 different sets of the systematic parameter values : "Nominal" by the default 13a SK MC with the 11b tuned version 3.2 flux reweighting, "Pre ND280 fit" using the NIWG central values for cross section systematic parameters, and "Post ND280 fit" using the fitted values by the BANFF.

$\sin^2 2\theta_{13} = 0.1$

	Nominal	Pre ND280 fit	Post ND280 fit
ν_e CC signal	18.2	18.8	17.7
ν_μ background	2.8	3.0	2.5
$\overline{\nu}_\mu$ background	0.2	0.2	0.1
ν_e background	3.3	3.6	3.3
$\overline{\nu}_e$ background	0.2	0.2	0.2
Total	24.6	25.8	23.8

$\sin^2 2\theta_{13} = 0.0$

	Nominal	Pre ND280 fit	Post ND280 fit
ν_e CC signal	0.4	0.4	0.4
ν_μ background	2.8	3.0	2.5
$\overline{\nu}_\mu$ background	0.2	0.2	0.1
ν_e background	3.6	3.8	3.6
$\overline{\nu}_e$ background	0.2	0.2	0.2
Total	7.1	7.7	6.7

Figures 6.7 and 6.8 show the predicted number of events distributions over the 20,000 throws of systematic parameters for the Run1-4 POT until May 8^{th}, 2013 (6.57×10^{20} POT), for fiTQun and POLfit, respectively. The distribution made with error values before the ND280 fit (blue hatched) and the distribution after the ND280 fit (red solid) are shown together for both $\sin^2 2\theta_{13} = 0.1$ and $= 0$ cases. As seen in both figures, the uncertainty on the predicted number of events is largely reduced after the ND280 fit. The size of error reduction by the ND280 data is larger in $\sin^2 2\theta_{13} = 0.1$ case than that in $\sin^2 2\theta_{13} = 0$ case. The main reason is that the ν_e signal sample is mostly composed of CCQE events, whose uncertainty is well constrained by the ND280 data, while the uncertainty of NC1π^0 events, one of the major backgrounds, cannot be constrained as stringently by ND280 data.

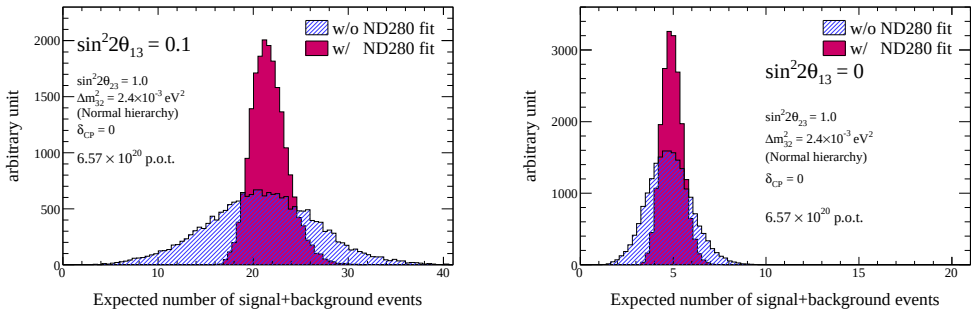

Figure 6.7: The predicted number of events distribution using the fiTQun π^0 rejection for the Run1-4 POT until May 8^{th}, 2013 (6.57×10^{20} POT) with $\sin^2 2\theta_{13} = 0.1$ (left) and $\sin^2 2\theta_{13} = 0$ (right).

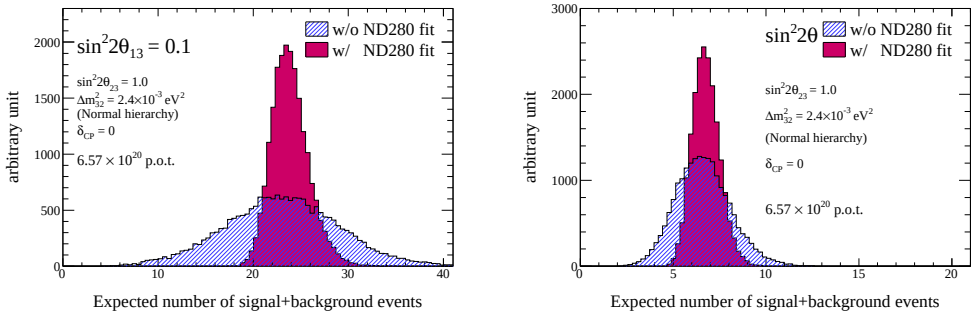

Figure 6.8: The predicted number of events distribution using the POLfit π^0 rejection for the Run1-4 POT until May 8^{th}, 2013 (6.57×10^{20} POT) with $\sin^2 2\theta_{13} = 0.1$ (left) and $\sin^2 2\theta_{13} = 0$ (right).

The systematic uncertainty on the predicted number of events due to each individual error source is also estimated by throwing only relevant systematic parameters and fixing the other parameters at their prior values. The results of both cases are summarized in Table 6.9 and Table 6.10, respectively, together with sizes of the total systematic errors. The dominant error sources in $\sin^2 2\theta_{13} = 0.1$ case after the ND280 data fit are the uncertainties on the beam flux prediction, M_A^{QE}, CCQE normalization and Spectral function. You may notice that the total error size is not equal to the quadratic sum of individual errors. This is because some of the systematic parameters can vary in a correlated way.

Table 6.9: The uncertainty (RMS/mean in %) on the predicted number of ν_e candidate events, using the fiTQun π^0 rejection, due to each individual error source.

Error source	$\sin^2 2\theta_{13} = 0.1$		$\sin^2 2\theta_{13} = 0$	
	Pre ND280 fit	Post ND280 fit	Pre ND280 fit	Post ND280 fit
Flux only	11.6	7.5	10.8	7.2
M_a^{QE} (GeV)	20.6	3.1	15.2	2.3
M_a^{res} (GeV)	3.5	1.1	7.4	2.3
CCQE norm. ($E_\nu < 1.5GeV$)	9.0	6.2	6.9	4.7
CC1π norm. ($E_\nu < 2.5GeV$)	4.0	2.0	4.6	2.4
NC1π^0 norm.	0.6	0.4	2.5	1.9
CC-other shape (GeV)	0.1	0.1	0.3	0.3
Spectral Function	6.0	6.0	5.1	5.1
p_f (GeV)	0.1	0.1	0.1	0.1
CC coherent norm.	0.2	0.2	0.3	0.3
NC coherent norm.	0.2	0.2	1.1	1.1
NC1$\pi^\pm$+NC norm.	0.5	0.5	2.2	2.2
$\sigma_{\nu_e CC}/\sigma_{\nu_{mu} CC}$	2.9	2.9	2.4	2.4
W shape (MeV)	0.2	0.2	1.0	1.0
pionless Δ-decay	3.7	3.7	3.4	3.4
SK detector efficiency	2.4	2.4	5.7	5.7
FSI+SI	2.3	2.3	3.1	3.1
Photo-nuclear	0.8	0.8	3.5	3.5
SK Energy	0.5	0.5	1.3	1.3
Total (All)	27.5	8.9	24.4	11.4

Table 6.10: The uncertainty (RMS/mean in %) on the predicted number of ν_e candidate events, using the POLfit π^0 rejection, due to each individual error source.

Error source	$\sin^2 2\theta_{13} = 0.1$		$\sin^2 2\theta_{13} = 0$	
	Pre ND280 fit	Post ND280 fit	Pre ND280 fit	Post ND280 fit
Flux only	11.4	7.4	10.5	6.9
M_a^{QE} (GeV)	19.2	2.9	11.6	1.8
M_a^{res} (GeV)	4.4	1.3	9.4	2.9
CCQE norm. ($E_\nu < 1.5GeV$)	8.4	5.8	5.2	3.6
CC1π norm. ($E_\nu < 2.5GeV$)	3.7	1.9	3.6	1.8
NC1π^0 norm.	1.6	1.2	5.7	4.3
CC-other shape (GeV)	0.1	0.1	0.2	0.2
Spectral Function	5.6	5.6	3.7	3.7
p_f (GeV)	0.1	0.1	0.1	0.1
CC coherent norm.	0.2	0.2	0.3	0.3
NC coherent norm.	0.7	0.7	2.6	2.6
NC1$\pi^\pm$+NC norm.	0.8	0.8	2.9	2.9
$\sigma_{\nu_e CC}/\sigma_{\nu_{mu} CC}$	2.7	2.7	1.8	1.8
W shape (MeV)	0.5	0.5	1.9	1.9
pionless Δ-decay	2.3	2.3	1.1	1.1
SK detector efficiency	2.6	2.6	5.2	5.2
FSI+SI	2.1	2.1	2.8	2.8
Photo-nuclear	0.8	0.8	2.9	2.9
SK Energy	0.6	0.6	1.4	1.4
Total (All)	26.0	8.2	22.2	10.9

The systematic uncertainty on the predicted number of events due to each group of error sources is summarized in Table 6.11 and Table 6.12, for fiTQun and POLfit π^0 rejection, respectively. The table also includes the size of total errors in this analysis and in the 2012 analysis. In addition to constraints on the flux uncertainties given by the BANFF fit, improvements on the SK detector error estimation [41, 42] and the FSI error estimation [39] contribute to the total error reduction in this analysis.

Table 6.11: The uncertainty (RMS/mean in %) on the predicted number of ν_e candidate events due to each group of systematic error sources, using the fiTQun π^0 rejection. The bottom line shows the previous official result by E^{rec} bin analysis with POLfit π^0 rejection as a reference. The results from the 2012 analysis are also present for comparison. The categorization of "Pre ND280 fit" and "Post ND280 fit" means "without the ND correction" (i.e. before taking a ratio between the ND and SK) and "with the ND correction" (i.e. after taking a ratio), respectively.

Error source	$\sin^2 2\theta_{13} = 0.1$		$\sin^2 2\theta_{13} = 0$	
	Pre ND280 fit	Post ND280 fit	Pre ND280 fit	Post ND280 fit
BANFF	26.0	2.9	21.8	4.8
Xsec (other than BANFF)	7.6	7.6	7.1	7.1
SK+FSI+SI+PN	3.5	3.5	7.3	7.3
Total	27.5	8.9	24.4	11.4
Total (2012 Analysis)	24.3	9.8	21.1	13.3

Table 6.12: The uncertainty (RMS/mean in %) on the predicted number of ν_e candidate events due to each group of systematic error sources, using the POLfit π^0 rejection. The bottom line shows the previous official result by E^{rec} bin analysis with POLfit π^0 rejection as a reference. The results from the 2012 analysis are also present for comparison. The categorization of "Pre ND280 fit" and "Post ND280 fit" means "without the ND correction" (i.e. before taking a ratio between the ND and SK) and "with the ND correction" (i.e. after taking a ratio), respectively.

Error source	$\sin^2 2\theta_{13} = 0.1$		$\sin^2 2\theta_{13} = 0$	
	Pre ND280 fit	Post ND280 fit	Pre ND280 fit	Post ND280 fit
BANFF	24.7	3.1	20.0	5.7
Xsec (other than BANFF)	6.7	6.7	6.1	6.1
SK+FSI+SI+PN	3.5	3.5	6.7	6.7
Total	26.0	8.2	22.2	10.9
Total (2012 Analysis)	24.3	9.8	21.1	13.3

Finally, the size of systematic error on the predicted number of events in each bin of the reconstructed neutrino energy distribution are shown in Figure 6.9 and Figure 6.10, for the fiTQun and POLfit π^0 rejection, respectively. The errors are shown for before the ND280 fit and after the ND280 fit. Even though fiTQun gives an overall higher error than POLfit, it is mitigated by the fact it constrains the NC background better. This is one of the leading systematic errors in this analysis.

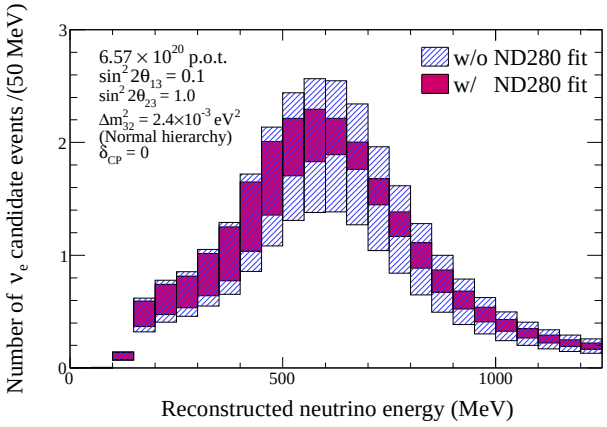

Figure 6.9: The systematic uncertainty on the predicted reconstructed neutrino energy distribution for $\sin^2 2\theta_{13} = 0.1$ and using fiTQun for the π^0 rejection.

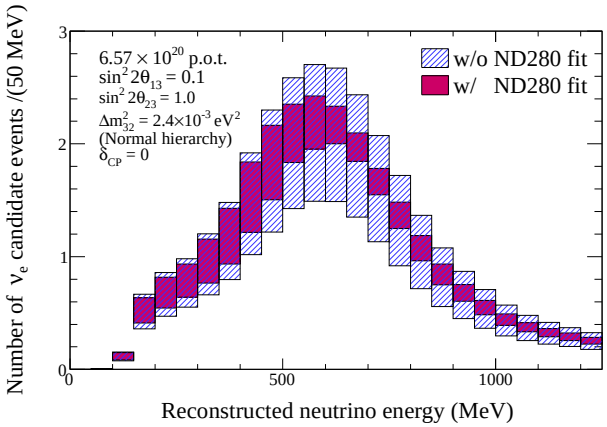

Figure 6.10: The systematic uncertainty on the predicted reconstructed neutrino energy distribution for $\sin^2 2\theta_{13} = 0.1$ and using POLfit for the π^0 rejection.

Chapter 7

Validation

We had several checks before analyzing T2K data. A validation in 2013 is based on the checks done in the 2012a analysis. Because the ν_e candidate selection has the new π^0 rejection cut by fiTQun, a fit bias was checked for both APfit and fiTQun cuts. Also fake data set was prepared to compare results with another ν_e analysis of p-θ bin and described in Appendix A. There was no bias found during the checks.

7.1 Fit bias check

Whether any biases exist on the oscillation parameter measurement or not is checked by using a toy experiment study.

First, a toy data set is generated according to the following procedure :

1. A set of the systematic parameters is randomly generated following the multivariate normal distribution and the final covariance matrix.

2. Calculate the predicted reconstructed neutrino energy spectrum and number of events for an assumed condition of oscillation parameters and data statistics (i.e. POT) by using the generated systematic parameter values.

3. A random number is generated following the Poisson distribution with its mean equal to the predicted number of events and used as the observed number of events in this toy data set.

4. If the number of observed events is not zero, the reconstructed neutrino energy of each event is randomly determined following the predicted energy spectrum.

Then, the number of observed events and their reconstructed neutrino energy for this toy data set are input into the oscillation fit algorithm. Specifically, as described in Section 5.4, the best fit point is searched for and the $-2\Delta \ln \mathcal{L}$ curve is drawn via a one dimensional scan on $\sin^2 2\theta_{13}$.

Finally, the "pull" of this measurement result is calculated as follows :

$$\text{pull} \quad = \quad \begin{cases} (\tau_{\text{fit}} - \tau_{\text{true}})/\sigma_{\text{positive}} & \text{if } \tau_{\text{fit}} > \tau_{\text{true}} \\ (\tau_{\text{fit}} - \tau_{\text{true}})/\sigma_{\text{negative}} & \text{if } \tau_{\text{fit}} < \tau_{\text{true}} \ , \end{cases} \tag{7.1}$$

where τ_{fit} is the best fit $\sin^2 2\theta_{13}$ value, τ_{true} is an assumed $\sin^2 2\theta_{13}$ value, and $\sigma_{\text{positive}}(\sigma_{\text{negative}})$ is the positive (negative) side 1σ error as illustrated by the blue arrows in Figure 7.1. Thus, a pull value is calculated for a toy data set.

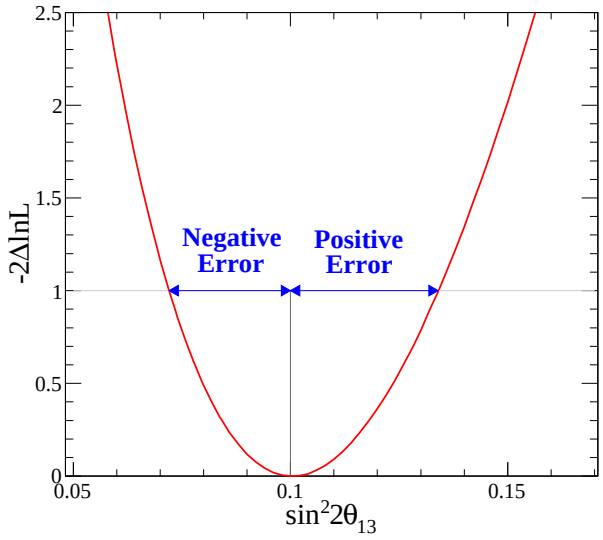

Figure 7.1: This plots shows the $-2\Delta \ln \mathcal{L}$ curve from a toy MC experiment with $\sin^2 2\theta_{13} = 0.1$. The definition of $\sigma_{positive}$ and $\sigma_{negative}$ can be seen by the labeled blue arrows.

If no bias exists on the $\sin^2 2\theta_{13}$ measurement in this analysis, the pull distribution derived from many toy experiments should be the standard normal distribution (mean=0, sigma=1). In this study, 4000 toy experiments are performed for each of several true $\sin^2 2\theta_{13}$ assumptions to check possible biases via the pull distribution. Figures 7.2 and 7.3 show the pull distributions with the Run1-4 using fiTQun and POLfit for the π^0 rejection, respectively. The mean and sigma of each pull distribution estimated by a Gaussian fitting are compiled in Figure 7.4. The pull mean values are mostly consistent with zero,

with a maximum deviation of about -0.1. This indicates the parameter biases are at most 10 % of the fitted uncertainties. So, there appears to be no need for a correction of the fitted values. Further more, the pull sigma values show very small deviations from the unity for all tested true $\sin^2 2\theta_{13}$ points. Due to both the large increase in POT since Run1+2+3b+3c and the change of π^0 rejection from POLfit to fiTQun, there appears to be no bias in the pull distributions.

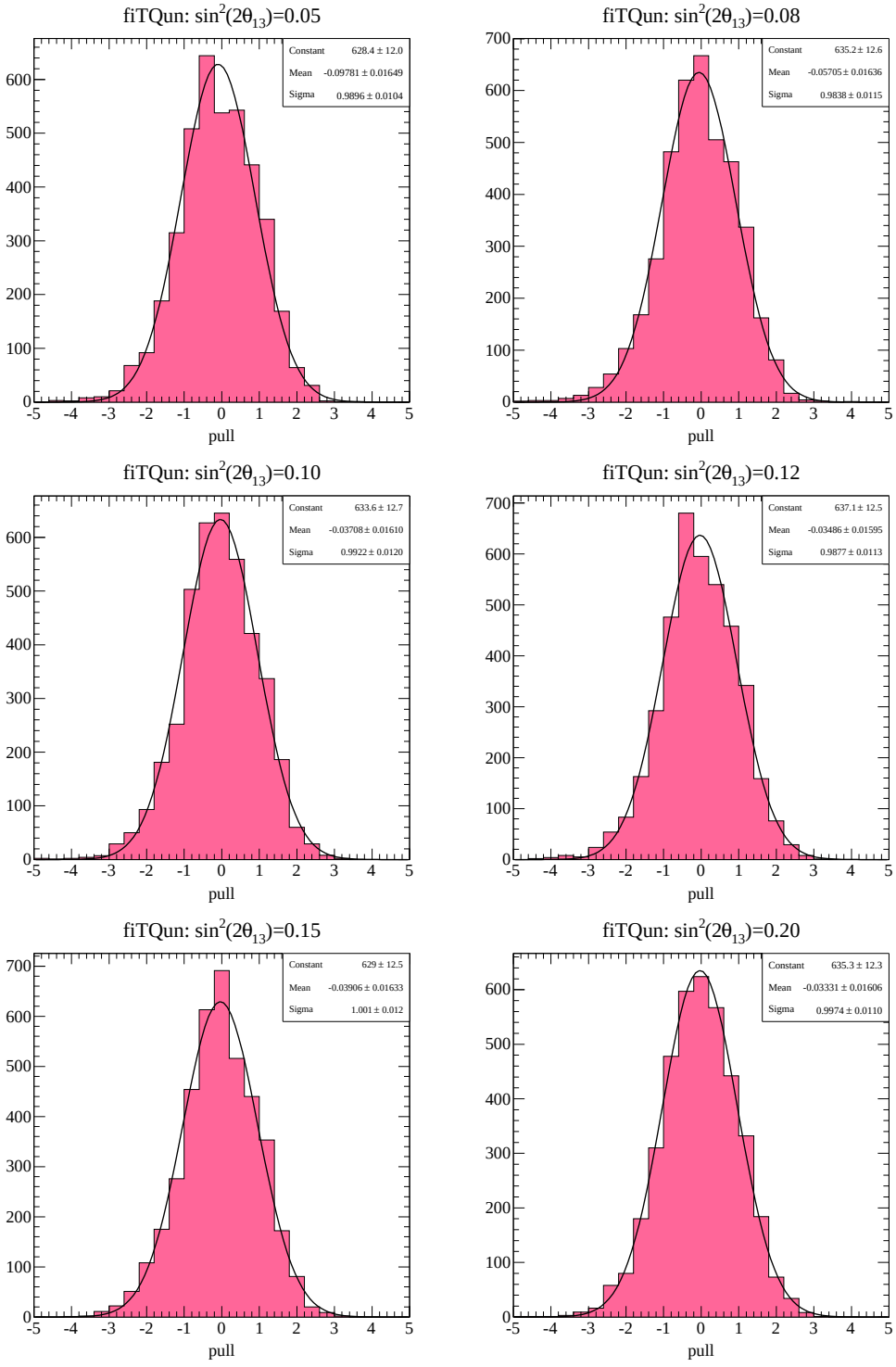

Figure 7.2: The pull distributions for the $\sin^2 2\theta_{13}$ measurement using fiTQun for the π^0 rejection. 4000 toy experiments were performed with the Run1-4 POT.

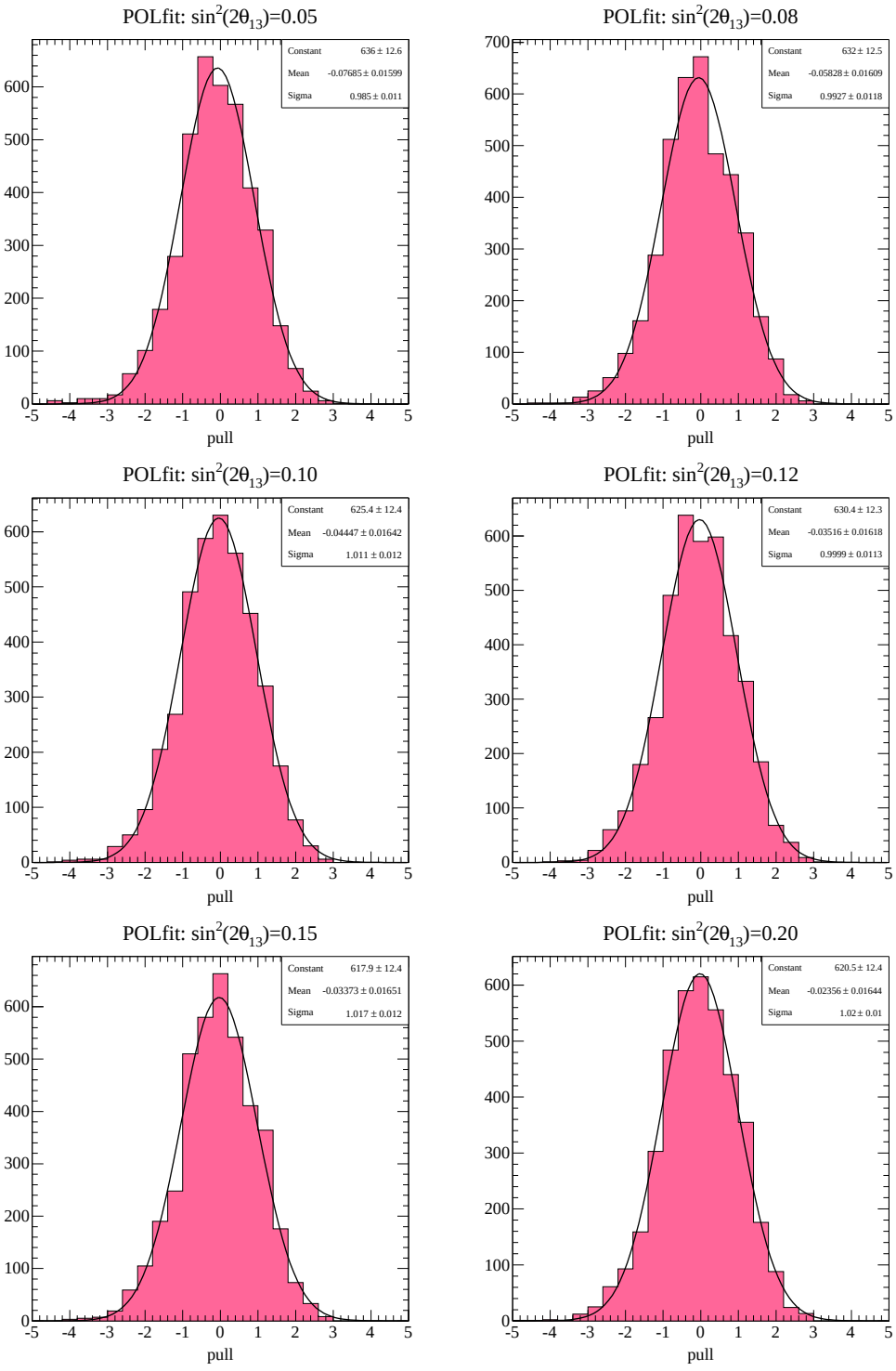

Figure 7.3: The pull distributions for the $\sin^2 2\theta_{13}$ measurement using POLfit for the π^0 rejection. 4000 toy experiments were performed with the Run1-4 POT.

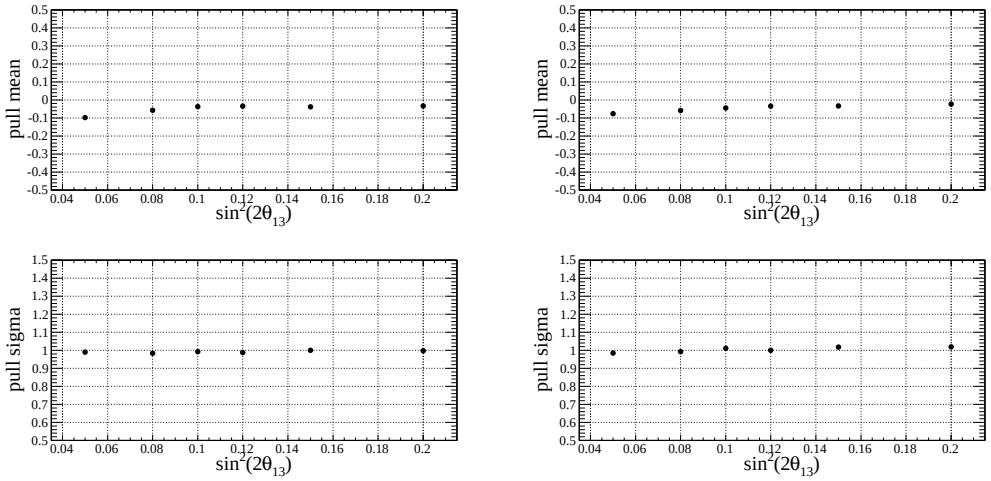

Figure 7.4: Summary of the pull mean (top) and sigma (bottom) values for several $\sin^2 2\theta_{13}$ assumptions using the fiTQun π^0 rejection (left) and POLfit π^0 rejection (right). The current Run1-4 POT (6.57×10^{20}) is used.

Chapter 8

Sensitivity

To estimate the expected allowed regions of $\sin^2 2\theta_{13}$ and the significance with respect to the $\theta_{13} = 0$ hypothesis for various conditions, the toy experiment method described in the previous section is utilized again. Just a $-2\ln\mathcal{L}$ (not $-2\Delta\ln\mathcal{L}$) curve as a function of $\sin^2 2\theta_{13}$ is obtained by a fit for each toy data set assuming a certain oscillation parameter set in true values. Then, the averaged $-2\ln\mathcal{L}$ curve is produced from a total of 4000 toy experiments. Finally, the minimum point of the averaged $-2\ln\mathcal{L}$ curve is searched for and the difference from the minimum value is obtained in $\sin^2 2\theta_{13}$.

The truth value of $\sin^2 2\theta_{13} = 0.1$ is assumed in this study. The 68 % (90 %) C.L. allowed region is defined by $\Delta\langle -2\ln\mathcal{L}\rangle < 1.00$ (2.71). The significance at $\theta_{13} = 0$ is defined as the square root of the difference between the averaged $-2\ln\mathcal{L}$ value at $\theta_{13} = 0$ and that at the minimum point, i.e. $\sqrt{\Delta\langle -2\ln\mathcal{L}\rangle_{\theta_{13}=0}}$ assuming a two-sided Gaussian probability. These numbers can be used for sensitivity comparisons in this sensitivity study.

8.1 Improvement with E^{rec} shape

First, the performance of this oscillation analysis with a reconstructed neutrino energy spectrum fit is compared with that of an analysis using only number of events. The postfit parameter values are used as prior values in the oscillation fit. Figure 8.1 shows the result of the comparison in the normal hierarchy case. The precision of the $\sin^2 2\theta_{13}$ measurement is improved if the spectrum information is added. The significance is 5.6 (5.3) for the spectrum fit (normalization only) analysis in case of fiTQun π^0 and 5.1 (4.8) for the spectrum fit (normalization only) analysis in case of POLfit π^0 with the Run1-4 POT.

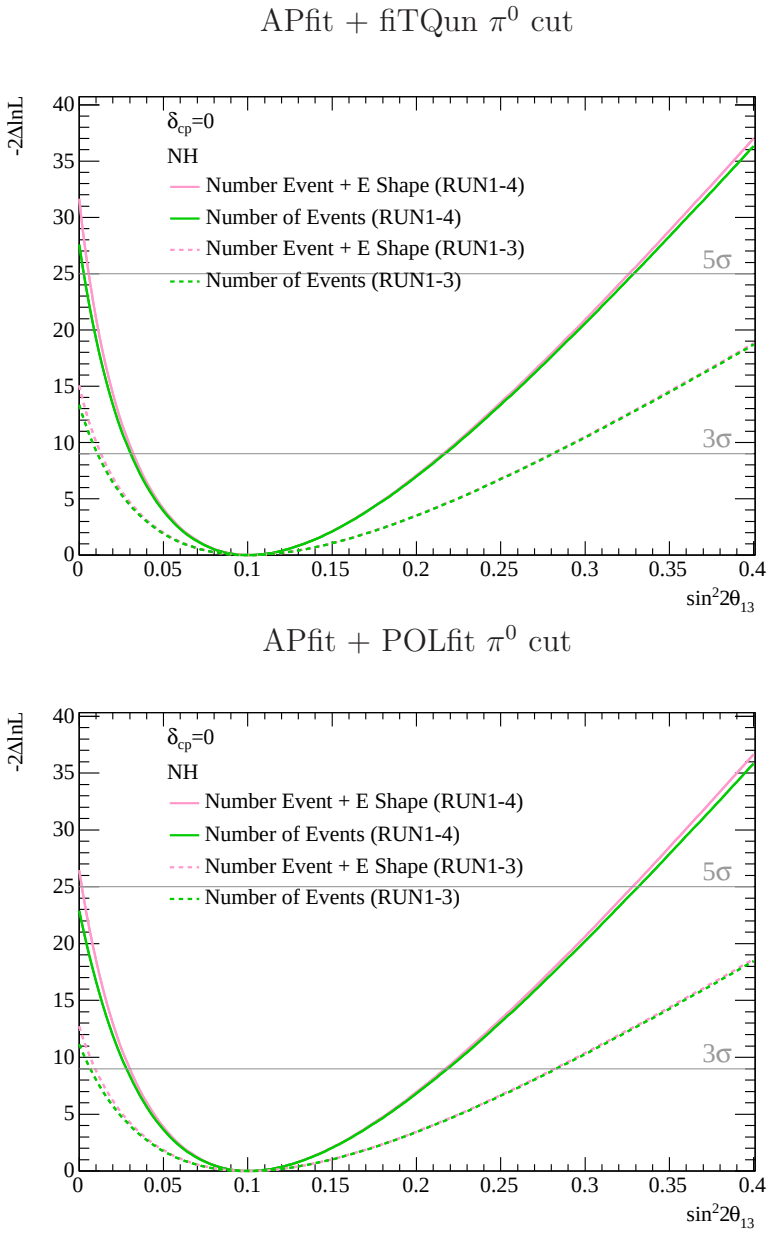

Figure 8.1: The $\Delta\langle -2\ln\mathcal{L}\rangle$ curve with the normalization analysis (green) and the reconstructed energy spectrum fit analysis (red) for fiTQun π^0 cut (top) and POLfit π^0 cut (bottom). The true value of $\sin^2 2\theta_{13}$ is assumed to be 0.1. The solid lines are for the Run1-4 (6.57×10^{20} POT) case, while the dashed lines are for the Run1-3 (3.01×10^{20} POT) case. The POT increase still brings a significant improvement compared with the E^{rec} shape information.

8.2 Improvement with fiTQun π^0 rejection

Figure 8.2 compares a $-2\Delta \ln \mathcal{L}$ curve of fiTQun π^0 with that of POLfit π^0. The ν_e candidate cut utilizing the fiTQun π^0 rejection shows better sensitivity than POLfit's π^0 rejection, therefore the fiTQun π^0 cut is determined to use for this analysis.

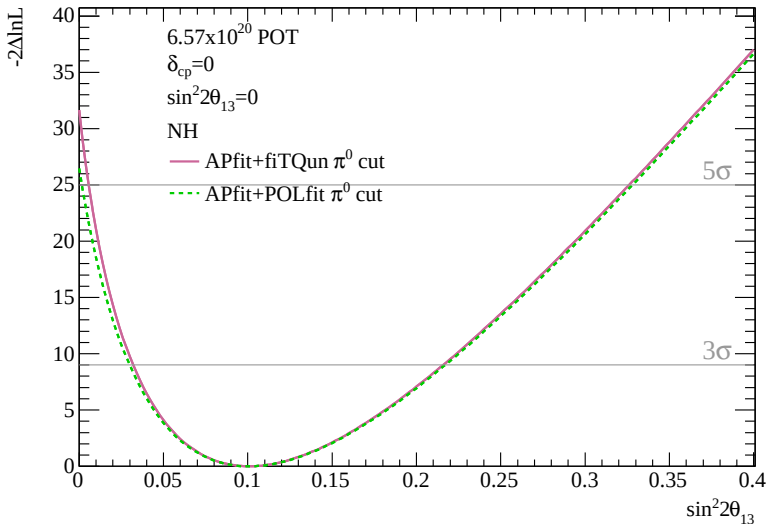

Figure 8.2: The $\Delta\langle -2 \ln \mathcal{L} \rangle$ curve of APfit+fiTQunπ^0 (Red, solid line) compared with APfit+POLfit (Green, dotted line) in Run1-4 (6.57×10^{20} POT).

8.3 Improvement with ND280 fit

Figure 8.3 shows the effect of the systematic errors. Again, the postfit parameter values are used as prior values in the oscillation fit. It can be seen that the sensitivity is slightly improved thanks to the constraint on the BANFF systematic parameters by the ND280 data fit. The significance is 5.6 (5.0) with the post (pre) fit errors in the Run1-4 POT by fiTQun π^0 cut.

8.4 Summary of the sensitivity study

Table 8.1 shows the significance at $\theta_{13} = 0$, the 68 % and 90 % C.L. allowed regions of $\sin^2 2\theta_{13}$ estimated from averaged log likelihood curves for the APfit+fiTQun π^0 cut and the APfit+POLfit π^0 in Run1-4 or Run1-3 POT. In

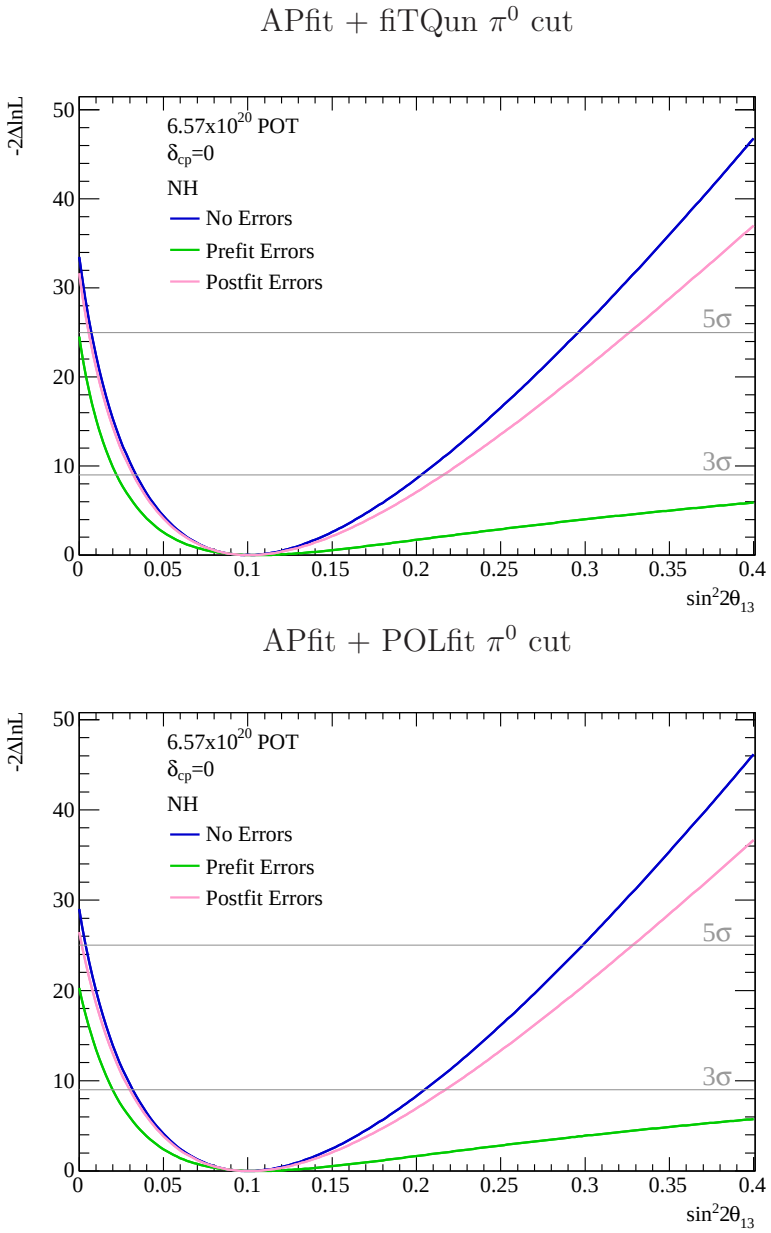

Figure 8.3: The $\Delta\langle -2\ln\mathcal{L}\rangle$ curve with no systematic errors (navy), pre ND280 fit systematic errors (green), and post ND280 fit systematic errors (red). The dashed lines are for the Run1-3 POT, while the solid lines are for the Run1-4 POT.

each condition, the post or pre ND280 fit values and errors are compared and the likelihood without E^{rec} shape and no systematic cases are also shown.

Table 8.1: Summary of sensitivity studies: the best fit, 68 % and 90 % C.L. allowed regions of $\sin^2 2\theta_{13}$ estimated from averaged log likelihood curves of 4000 toy MC. The true value of $\sin^2 2\theta_{13} = 0.1$, $\delta_{CP} = 0$, $|\Delta m^2_{32}| = 2.4 \times 10^{-3}\mathrm{eV}^2$, and normal mass hierarchy are assumed. The significance at $\theta_{13} = 0$ in this table is defined as $\sqrt{\Delta\langle -2\ln\mathcal{L}\rangle_{\theta_{13}=0}}$ assuming a two-sided Gaussian probability. The first line (Post ND280 fit using fiTQun π^0 cut) is adopted as a primary analysis in 2013a.

	π^0 cut	POT [$\times 10^{20}$]	Significance	C.L. (68%)	C.L. (90%)
Post ND280 fit	fiTQun	6.57 (Run1-4)	5.62	0.073 - 0.133	0.058 - 0.157
Pre ND280 fit	fiTQun	6.57 (Run1-4)	4.95	0.067 - 0.170	0.049 - 0.241
No systematics	fiTQun	6.57 (Run1-4)	5.79	0.074 - 0.130	0.059 - 0.151
Rate only	fiTQun	6.57 (Run1-4)	5.25	0.073 - 0.133	0.057 - 0.158
Post ND280 fit	fiTQun	3.01 (Run1-3)	3.88	0.063 - 0.149	0.043 - 0.186
Pre ND280 fit	fiTQun	3.01 (Run1-3)	3.58	0.057 - 0.180	0.037 - 0.267
No systematics	fiTQun	3.01 (Run1-3)	3.93	0.063 - 0.145	0.044 - 0.180
Rate only	fiTQun	3.01 (Run1-3)	3.65	0.062 - 0.149	0.042 - 0.186
Post ND280 fit	POLfit	6.57 (Run1-4)	5.14	0.073 - 0.134	0.057 - 0.158
Pre ND280 fit	POLfit	6.57 (Run1-4)	4.50	0.066 - 0.172	0.048 - 0.245
No systematics	POLfit	6.57 (Run1-4)	5.39	0.073 - 0.130	0.058 - 0.153
Rate only	POLfit	6.57 (Run1-4)	4.78	0.072 - 0.134	0.056 - 0.159
Post ND280 fit	POLfit	3.01 (Run1-3)	3.56	0.062 - 0.149	0.041 - 0.186
Pre ND280 fit	POLfit	3.01 (Run1-3)	3.29	0.056 - 0.186	0.035 - 0.272
No systematics	POLfit	3.01 (Run1-3)	3.64	0.062 - 0.146	0.042 - 0.182
Rate only	POLfit	3.01 (Run1-3)	3.34	0.061 - 0.149	0.040 - 0.187

By each true value of $\sin^2 2\theta_{13}$, Table 8.2 shows the best fit points, the significance, the 68 % and 90 % C.L. allowed regions of $\sin^2 2\theta_{13}$ estimated from averaged log likelihood curves for the APfit+fiTQun π^0 cut and the APfit+POLfit π^0 in Run1-4 POT. The post ND280 fit values and errors are used as prior values and errors of the systematic parameters in the oscillation fit.

Table 8.2: Sensitivity studies with different $\sin^2 2\theta_{13}$ values in Run1-4 POT (6.57×10^{20} POT): the best fit, 68 % and 90 % C.L. allowed regions of $\sin^2 2\theta_{13}$ estimated from averaged log likelihood curves of 4000 toy MC. In addition to the true value of $\sin^2 2\theta_{13}$, $\delta_{\mathrm{CP}} = 0$, $|\Delta m^2_{32}| = 2.4 \times 10^{-3}\mathrm{eV}^2$, and normal mass hierarchy are also assumed. The significance at $\theta_{13} = 0$ in this table is defined as $\sqrt{\Delta\langle -2 \ln \mathcal{L}\rangle_{\theta_{13}=0}}$ assuming a two-sided Gaussian probability.

True		fiTQun	POLfit
0.05	best-fit	0.050	0.050
	68 % C.L.	$0.030 - 0.075$	$0.029 - 0.076$
	90 % C.L.	$0.019 - 0.094$	$0.018 - 0.095$
	significance	3.24	2.92
0.08	best-fit	0.080	0.080
	68 % C.L.	$0.056 - 0.110$	$0.055 - 0.111$
	90 % C.L.	$0.042 - 0.132$	$0.041 - 0.133$
	significance	4.73	4.30
0.10	best-fit	0.100	0.100
	68 % C.L.	$0.073 - 0.133$	$0.073 - 0.134$
	90 % C.L.	$0.058 - 0.157$	$0.057 - 0.158$
	significance	5.62	5.14
0.12	best-fit	0.120	0.120
	68 % C.L.	$0.091 - 0.156$	$0.091 - 0.157$
	90 % C.L.	$0.074 - 0.182$	$0.073 - 0.183$
	significance	6.45	5.93
0.15	best-fit	0.152	0.150
	68 % C.L.	$0.118 - 0.190$	$0.117 - 0.190$
	90 % C.L.	$0.098 - 0.219$	$0.097 - 0.219$
	significance	7.60	6.99
0.20	best-fit	0.200	0.200
	68 % C.L.	$0.162 - 0.246$	$0.161 - 0.246$
	90 % C.L.	$0.139 - 0.278$	$0.139 - 0.278$
	significance	9.30	8.59

Chapter 9

Results

T2K has observed a total of 28 ν_e candidate events by APfit+fiQTun π^0 cut and 31 ν_e candidate events by APfit+POLfit π^0 cut in the Run1+2+3b+3c+4 data until May 8^{th}, 2013 (6.57×10^{20} POT).

These events with reconstructed neutrino energy are listed in Table 9.1. These values are used as inputs to the oscillation fit.

9.0.1 Fit results of θ_{13} for $\delta_{\mathrm{CP}} = 0$

Figure 9.1 shows the $-2\Delta \ln \mathcal{L}$ curve obtained as a result of the Run1+2+3b+3c+4 data fit with an assumption of $\delta_{\mathrm{CP}} = 0$, $|\Delta m^2_{32}| = 2.4 \times 10^{-3}\mathrm{eV}^2$, normal mass hierarchy (top) and inverted mass hierarchy (bottom) comparing fiTQun π^0 (left) and POLfit π^0 (right). The best fit point and confidence intervals assuming $\delta_{\mathrm{CP}} = 0$ and $|\Delta m^2_{32}| = 2.4 \times 10^{-3}\mathrm{eV}^2$ are summarized in Table 9.2. The best fit E^{rec} distributions are shown in Figure 9.2. The best fit values and confidence intervals obtained by the fit using the E^{rec} spectrum in addition to the number of events are slightly larger than those by the rate only fit.

Table 9.1: The reconstructed neutrino energy of ν_e candidate events observed during the Run1+2+3b+3c+4 (until May 8^{th}, 2013) periods.

No. (fiTQun π^0)	No. (POLfit π^0)	T2K Run	Reconstructed ν energy (MeV)
1	1	Run1	482.681
2	2	Run2	829.162
3	3	Run2	716.247
4	4	Run2	1114.52
5	5	Run2	587.717
6	6	Run2	417.171
7	7	Run3b	431.869
8	8	Run3b	383.94
9	9	Run3c	600.69
10	10	Run3c	951.448
11	11	Run3c	937.303
12	12	Run4	751.45
13	13	Run4	146.307
14	14	Run4	611.946
15	15	Run4	366.776
16	16	Run4	601.586
17	17	Run4	772.451
18	18	Run4	523.487
19	19	Run4	532.47
	20	Run4	447.086
20	21	Run4	884.144
21	22	Run4	793.42
22	23	Run4	551.105
23	24	Run4	843.018
24	25	Run4	562.097
25	26	Run4	778.355
	27	Run4	673.245
	28	Run4	625.319
26	29	Run4	454.037
27	30	Run4	535.791
28	31	Run4	874.332

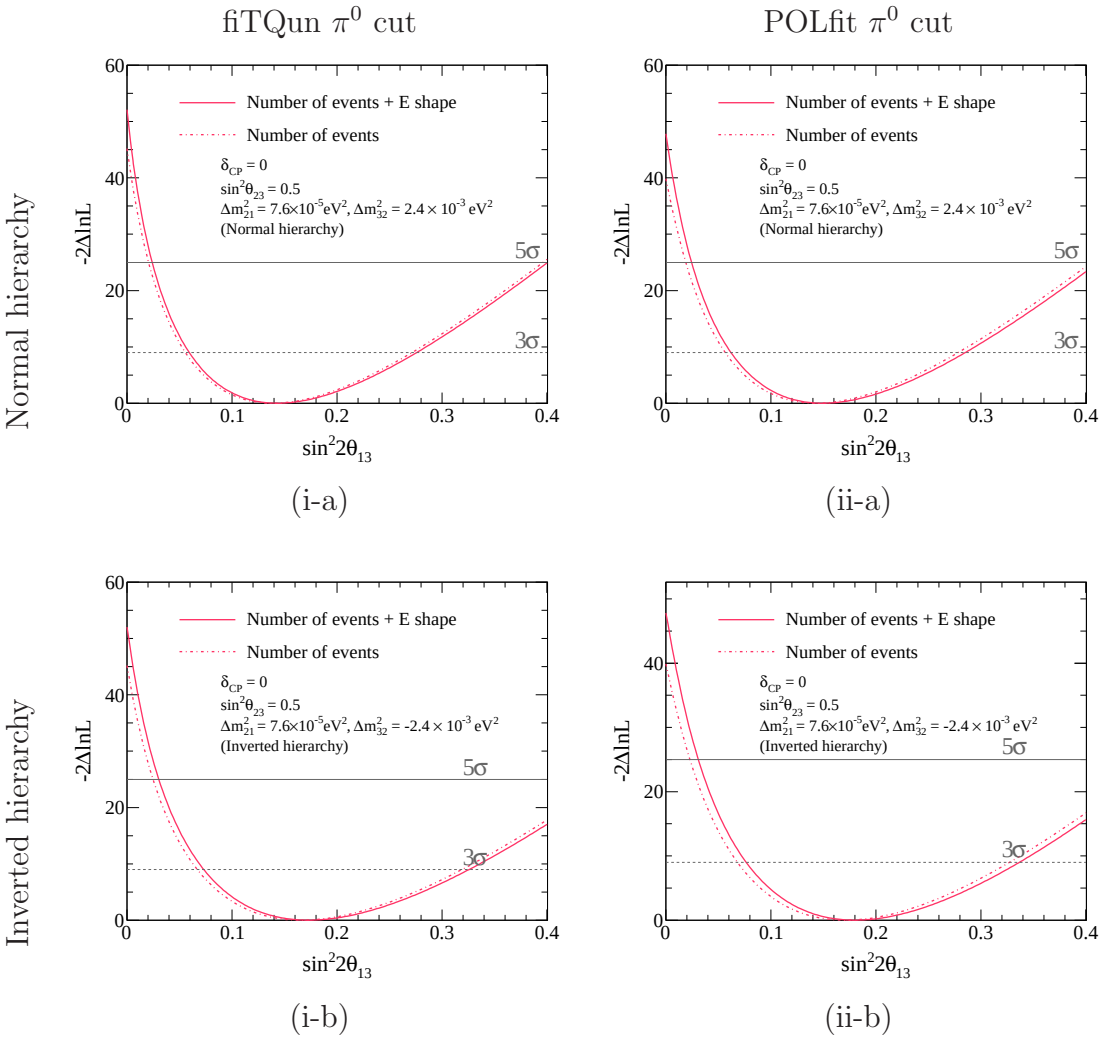

Figure 9.1: The $-2\Delta \ln \mathcal{L}$ curve as a result of the Run1+2+3b+3c+4 data fit with an assumption of normal mass hierarchy (top) and inverted mass hierarchy (bottom). Results by the prior analysis using fiTQun π^0 cut are shown in left and that using POLfit π^0 cut in right. $\delta_{\rm CP} = 0$ and $|\Delta m^2_{32}| = 2.4 \times 10^{-3}{\rm eV}^2$ are also assumed. The solid lines represent the results of the data fit using the E^{rec} spectrum information, while the dashed-dotted lines are obtained by the fit with only the number of events (1 bin analysis).

Table 9.2: The best fit points and confidence intervals for $\sin^2 2\theta_{13}$ as a result of the Run1+2+3b+3c+4 data fit assuming $\delta_{\rm CP} = 0$ and $|\Delta m^2_{32}| = 2.4 \times 10^{-3} {\rm eV}^2$. The primary result uses fiTQun π^0 cut with E^{rec} spectrum (i-a, b).

Number of events + E^{rec} spectrum

	fiTQun π^0 cut (i)		POLfit π^0 cut (ii)	
Hierarchy	(a) Normal	(b) Inverted	(a) Normal	(b) Inverted
Best fit	0.144	0.172	0.150	0.180
68 % C.L.	0.110 - 0.181	0.134 - 0.217	0.115 - 0.188	0.140 - 0.226
90 % C.L.	0.092 - 0.209	0.112 - 0.249	0.096 - 0.217	0.117 - 0.258

Number of events only (1 bin analysis)

	fiTQun π^0 cut (iii)		POLfit π^0 cut (iv)	
Hierarchy	(a) Normal	(b) Inverted	(a) Normal	(b) Inverted
Best fit	0.140	0.166	0.144	0.172
68 % C.L.	0.106 - 0.177	0.128 - 0.210	0.109 - 0.182	0.131 - 0.217
90 % C.L.	0.088 - 0.205	0.106 - 0.243	0.090 - 0.210	0.109 - 0.249

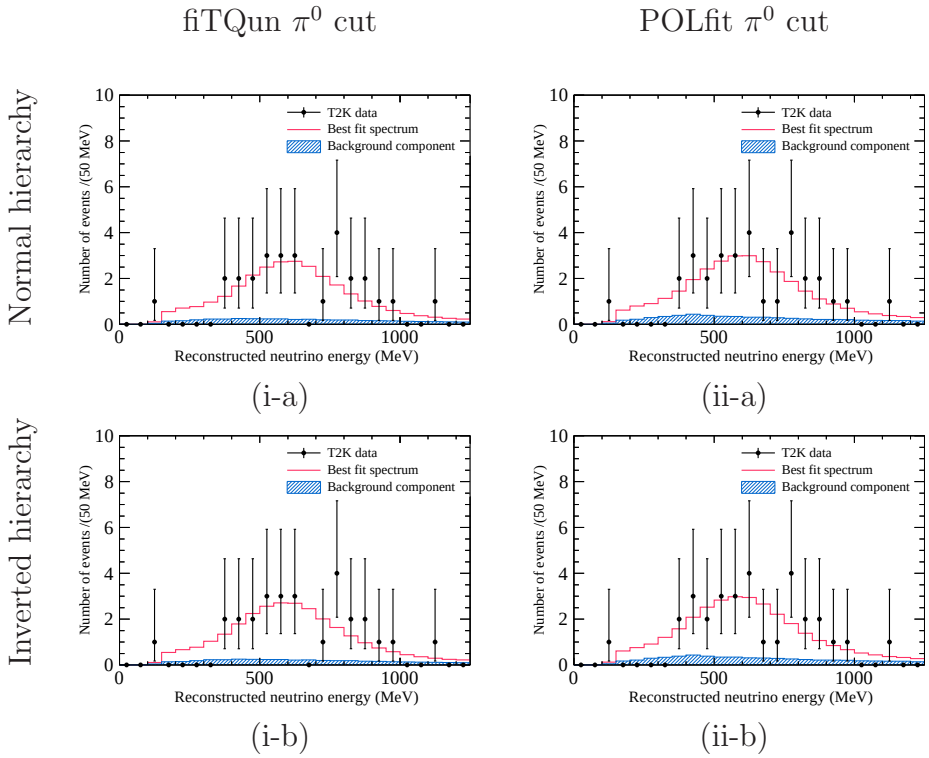

Figure 9.2: The observed E^{rec} distribution (black dots) and the predicted spectrum at the best fit point (blue histogram). The hatched portion represents the background component in the best fit prediction. The fit is performed assuming $\delta_{\mathrm{CP}} = 0$, $\sin^2 2\theta_{12} = 0.8495$, $\sin^2 2\theta_{23} = 1.0$, $\Delta m^2_{21} = 7.6 \times 10^{-5}$ eV^2 and $|\Delta m^2_{32}| = 2.4 \times 10^{-3}$eV^2.

9.1 Fit results of θ_{13} for various δ_{CP}

The 60 and 90 % C.L. (and also 68 % C.L.) regions by the Run1+2+3b+3c+4 data fit are determined using the constant $-2\Delta \ln \mathcal{L}$ method. A consistency with Feldman-Cousins method was confirmed in T2K-TN-109. Figures 9.3 and 9.4 show the 68 % and 90 % C.L. regions of $\sin^2 2\theta_{13}$ for each value of δ_{CP} measured by the Run1+2+3b+3c+4 data fit, for APfit+fiTQun π^0 and APfit+POLfit π^0 respectively.

Figures 9.5 and 9.6 show a comparison between the new results and the 2012a results, for APfit+fiTQun π^0 and APfit+POLfit π^0 respectively. The new results are consistent with our previous results and give a much better constraint on $\sin^2 2\theta_{13}$. Figures 9.7 and 9.8 show a comparison between the new results only with the Run1+2+3b+3c data and the 2012a analysis results, for APfit+fiTQun π^0 and APfit+POLfit π^0 respectively. The shift in APfit+POLfit π^0 between Run1+2+3b+3c and the 2012a result is due to the update of the ND280 fit.

Finally, the 68 % and 90 % allowed regions of the Run4 data are compared with the Run1+2+3b+3c data (Figure 9.9, 9.10). Both the results are still consistent within 1-σ with each other.

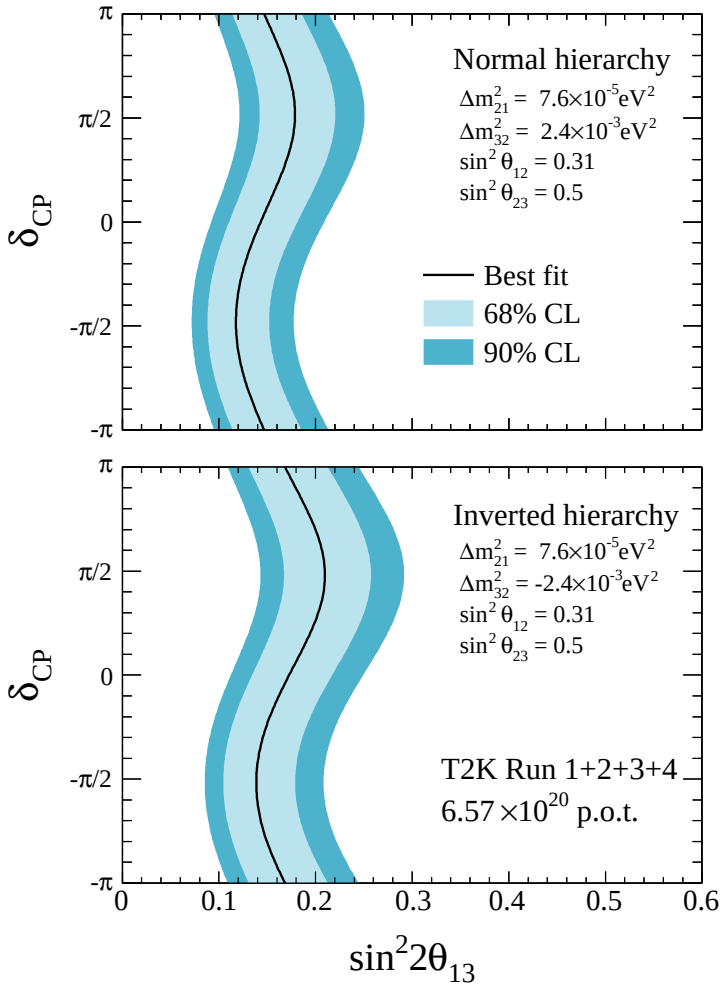

Figure 9.3: (APfit + fiTQun π^0) The 68 % and 90 % C.L. regions for $\sin^2 2\theta_{13}$ for each value of δ_{CP} measured by the Run1+2+3b+3c+4 data fit assuming normal mass hierarchy (top) and inverted mass hierarchy (bottom). The confidence intervals are determined by the constant $-2\Delta \ln \mathcal{L}$ method.

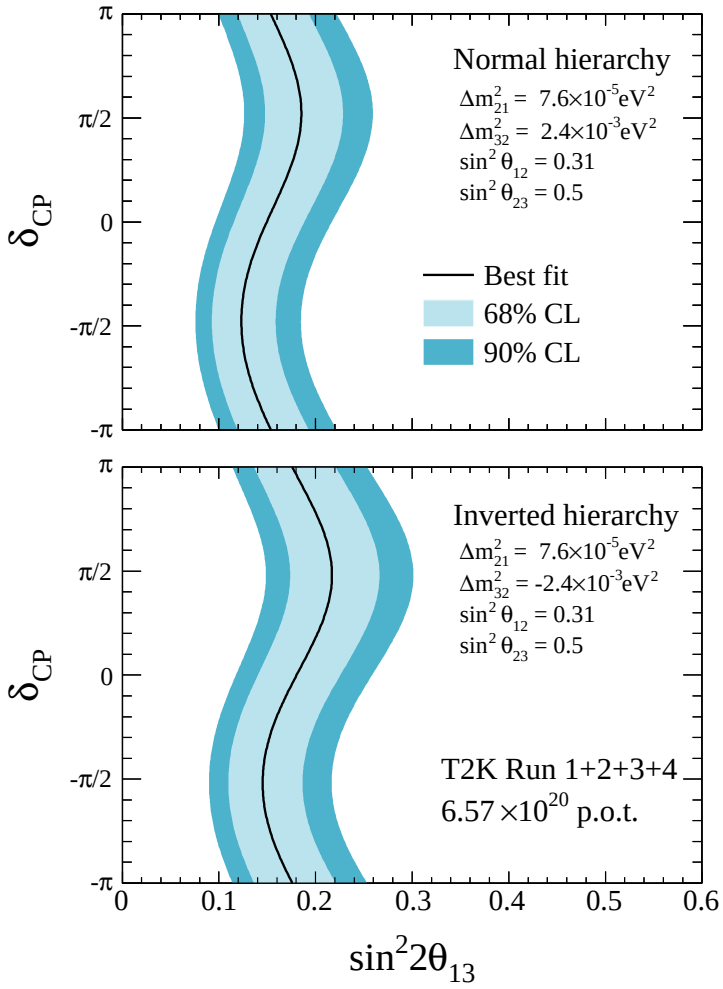

Figure 9.4: (APfit + POLfit π^0) The 68 % and 90 % C.L. regions for $\sin^2 2\theta_{13}$ for each value of δ_{CP} measured by the Run1+2+3b+3c+4 data fit assuming normal mass hierarchy (top) and inverted mass hierarchy (bottom). The confidence intervals are determined by the constant $-2\Delta \ln \mathcal{L}$ method.

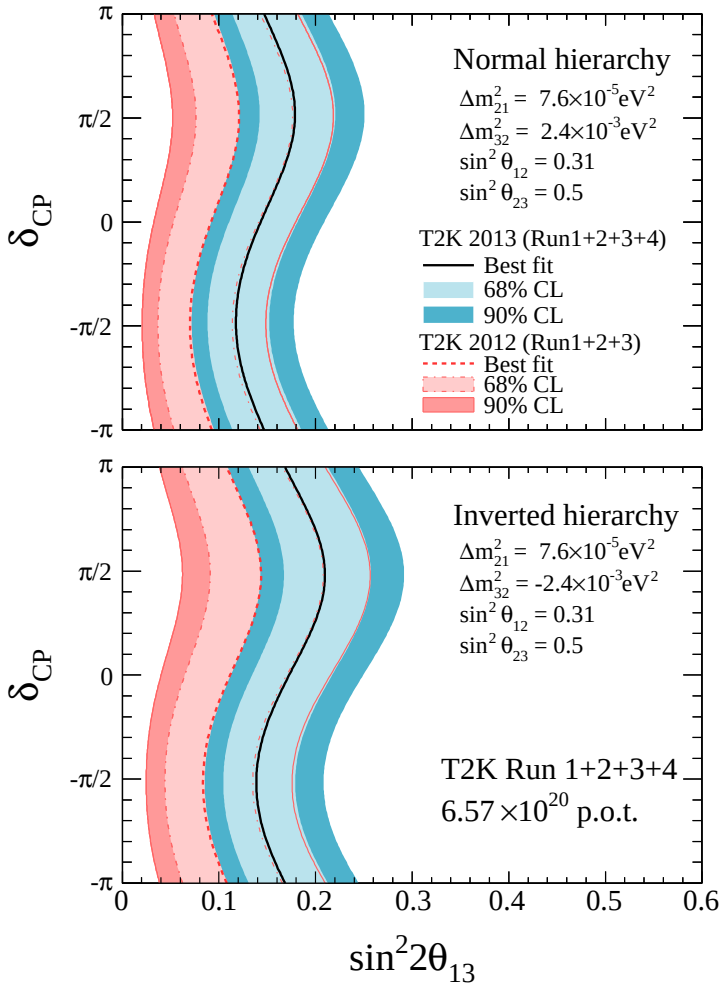

Figure 9.5: (APfit + fiTQun π^0) The 68 % and 90 % C.L. regions for $\sin^2 2\theta_{13}$ for each value of δ_{CP} measured by the Run1+2+3b+3c+4 data fit assuming normal mass hierarchy (top) and inverted mass hierarchy (bottom), along with the 2012a ν_e analysis results.

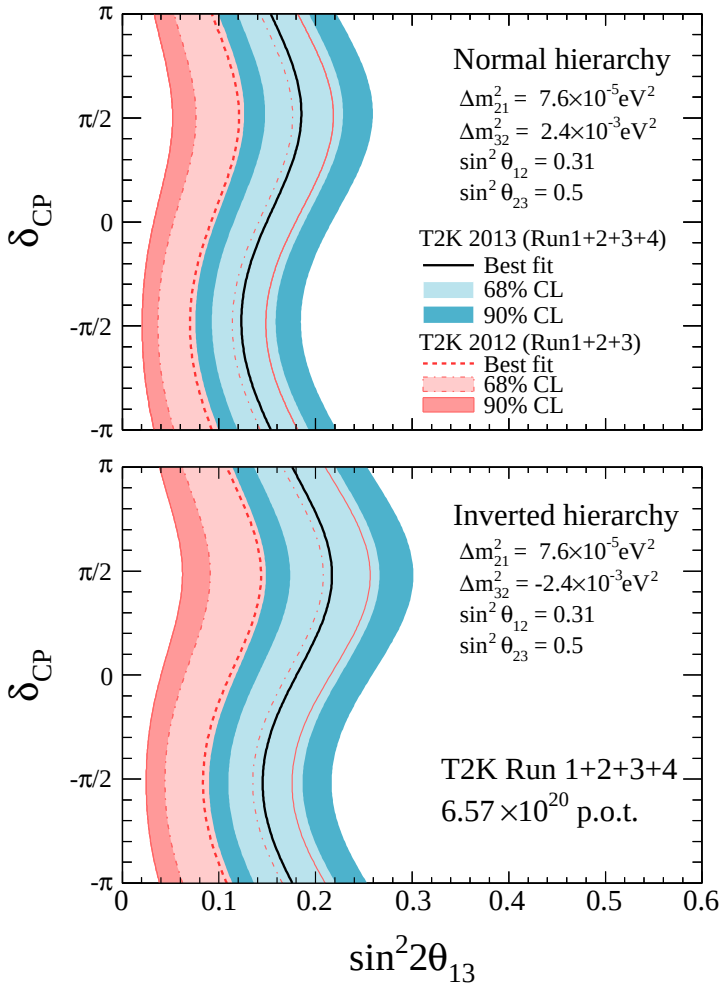

Figure 9.6: (APfit + POLfit π^0) The 68 % and 90 % C.L. regions for $\sin^2 2\theta_{13}$ for each value of δ_{CP} measured by the Run1+2+3b+3c+4 data fit assuming normal mass hierarchy (top) and inverted mass hierarchy (bottom), along with the 2012a ν_e analysis results.

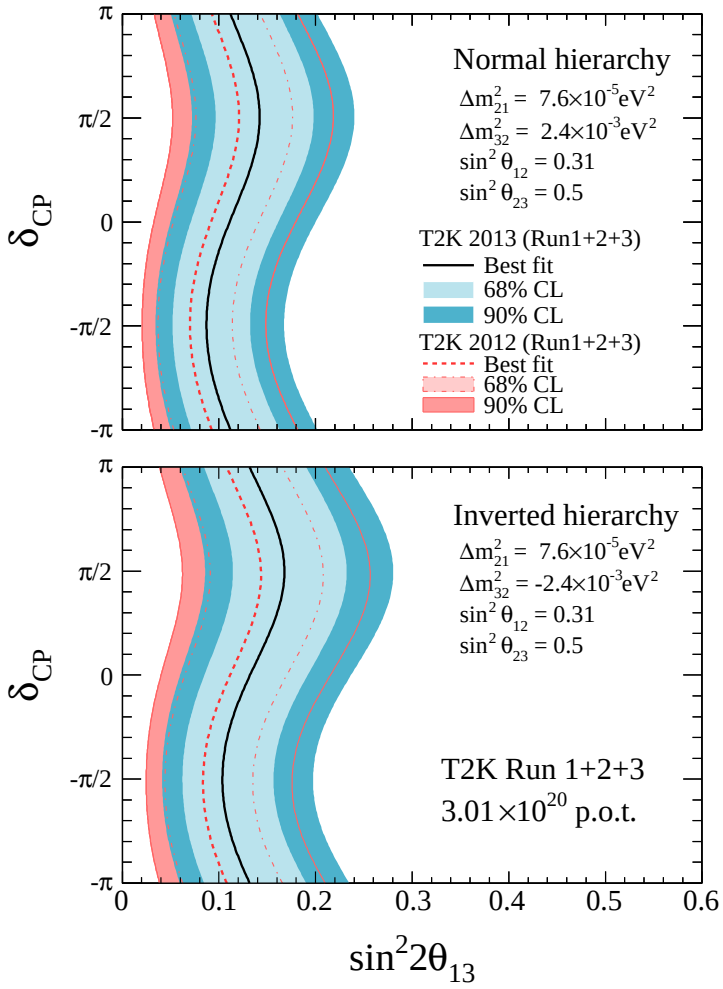

Figure 9.7: (APfit + fiTQun π^0) The 68 % and 90 % C.L. regions for $\sin^2 2\theta_{13}$ for each value of δ_{CP} measured by the Run1+2+3b+3c data fit assuming normal mass hierarchy (top) and inverted mass hierarchy (bottom), along with the 2012a ν_e analysis results by red regions.

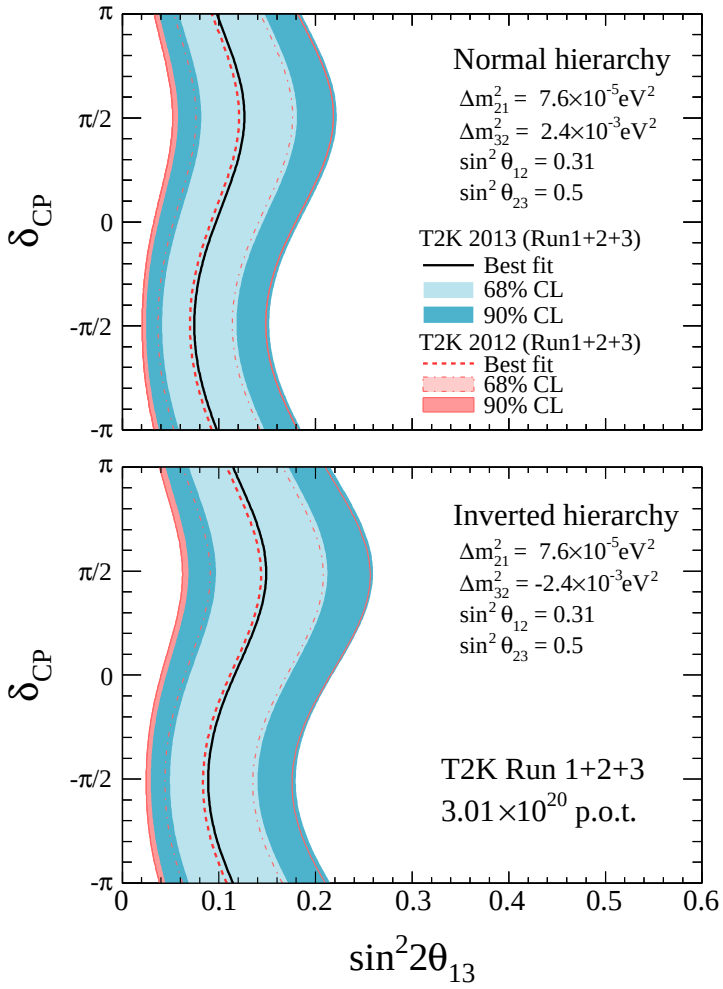

Figure 9.8: (APfit + POLfit π^0) The 68 % and 90 % C.L. regions for $\sin^2 2\theta_{13}$ for each value of δ_{CP} measured by the Run1+2+3b+3c data fit assuming normal mass hierarchy (top) and inverted mass hierarchy (bottom), along with the 2012a ν_e analysis results by red regions.

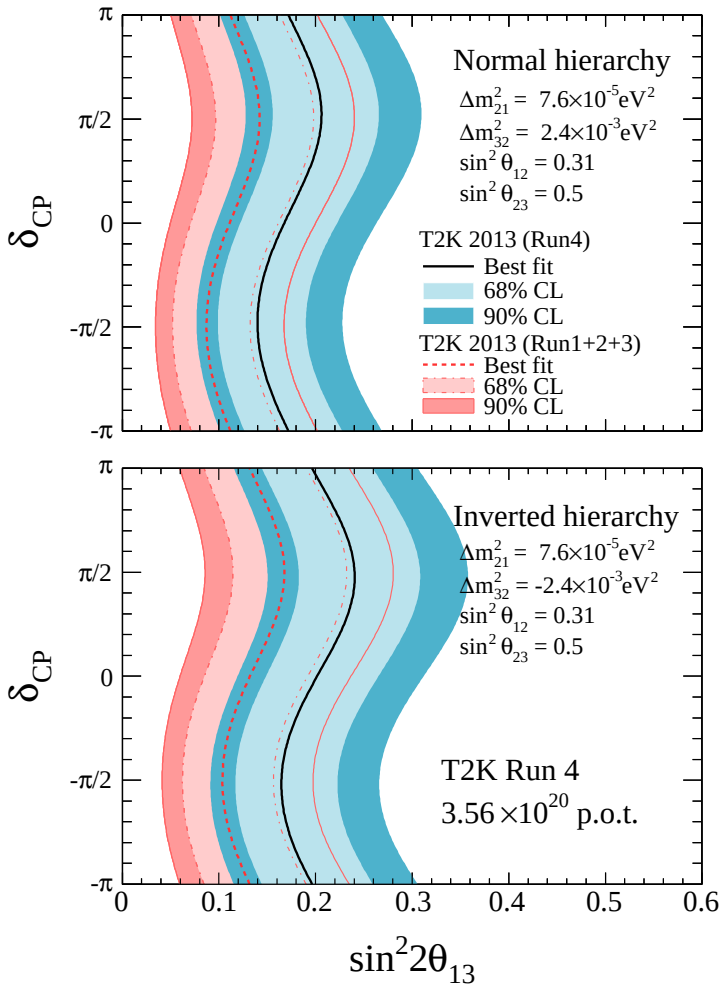

Figure 9.9: (APfit + fiTQun π^0) The 68 % and 90 % C.L. regions for $\sin^2 2\theta_{13}$ for each value of δ_{CP} measured by the Run4 data fit (blue regions) and by the Run1+2+3b+3c data fit (red hatched and lines) assuming normal mass hierarchy (top) and inverted mass hierarchy (bottom).

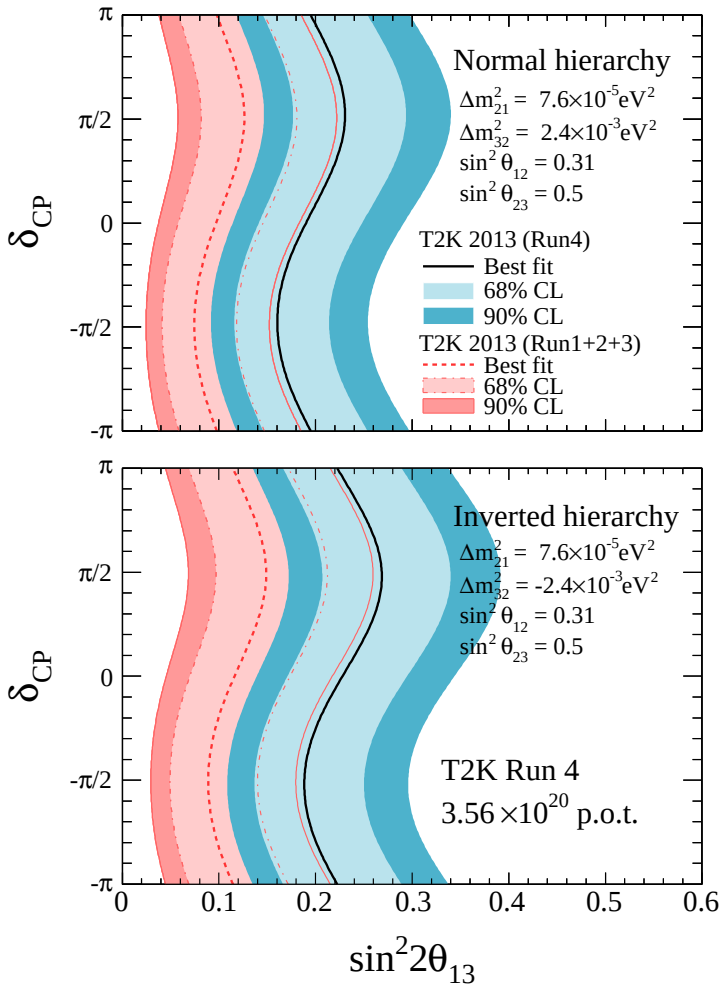

Figure 9.10: (APfit + POLfit π^0) The 68 % and 90 % C.L. regions for $\sin^2 2\theta_{13}$ for each value of δ_{CP} measured by the Run4 data fit (blue regions) and by the Run1+2+3b+3c data fit (red hatched and lines) assuming normal mass hierarchy (top) and inverted mass hierarchy (bottom).

9.2 Fit results with θ_{13} and Δm_{32}

Figures 9.11 (fiTQun π^0) and 9.12 (POLfit π^0) show the 68 % and 90 % C.L. regions for $\sin^2 2\theta_{13}$ and Δm^2_{32} measured by the Run1+2+3b+3c+4 data fit assuming $\delta_{\mathrm{CP}} = 0$. The best fit point is searched for in the two-dimensional plane (i.e. global scan), and the 68 % (90 %) C.L. region is determined by $-2\Delta \ln \mathcal{L} < 2.30$ (4.61).

Figure 9.13, shows a great improvement from the 2012a result as can be seen from the blue regions (2012a results) to the red lines (new results with fiTQun π^0).

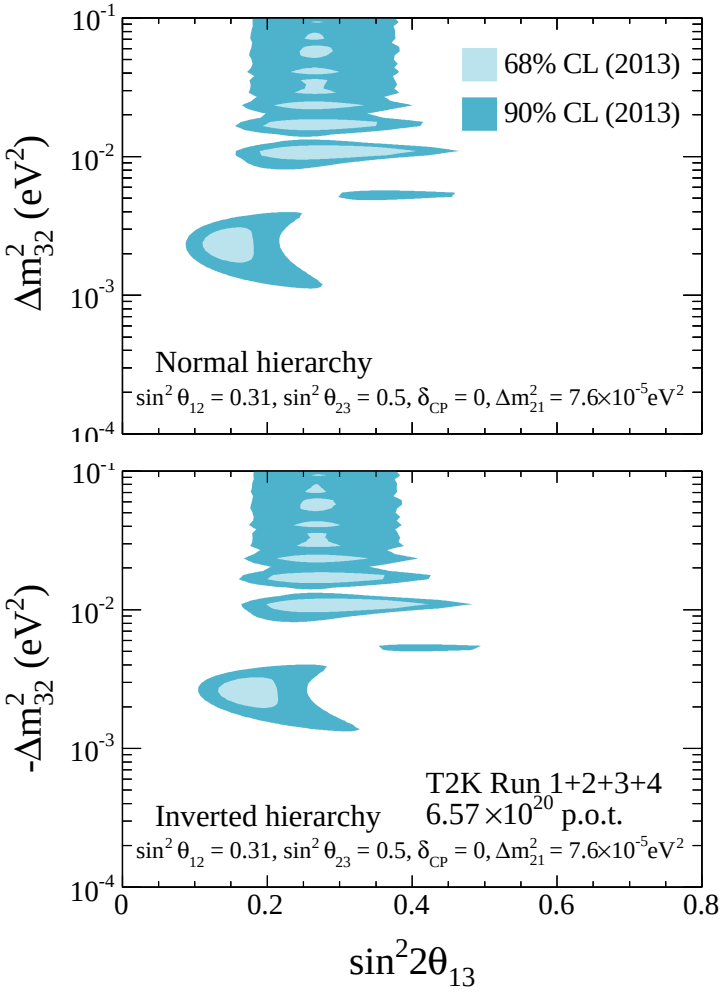

Figure 9.11: (APfit + fiTQun π^0) The 68 % and 90 % C.L. regions for $\sin^2 2\theta_{13}$ and Δm^2_{32} measured by the Run1+2+3b+3c+4 data fit assuming $\delta_{\mathrm{CP}} = 0$ and normal mass hierarchy (top) or inverted mass hierarchy (bottom). The regions are determined by a global scan in the two-dimensional plane.

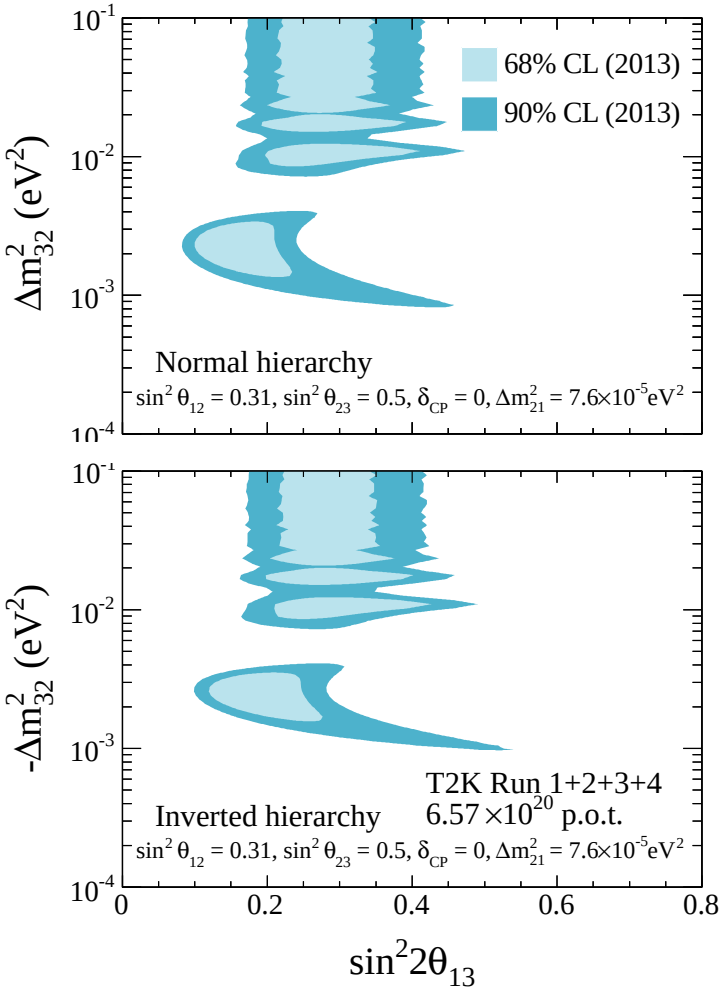

Figure 9.12: (APfit + POLfit π^0) The 68 % and 90 % C.L. regions for $\sin^2 2\theta_{13}$ and Δm^2_{32} measured by the Run1+2+3b+3c+4 data fit assuming $\delta_{\mathrm{CP}} = 0$ and normal mass hierarchy (top) or inverted mass hierarchy (bottom). The regions are determined by a global scan in the two-dimensional plane.

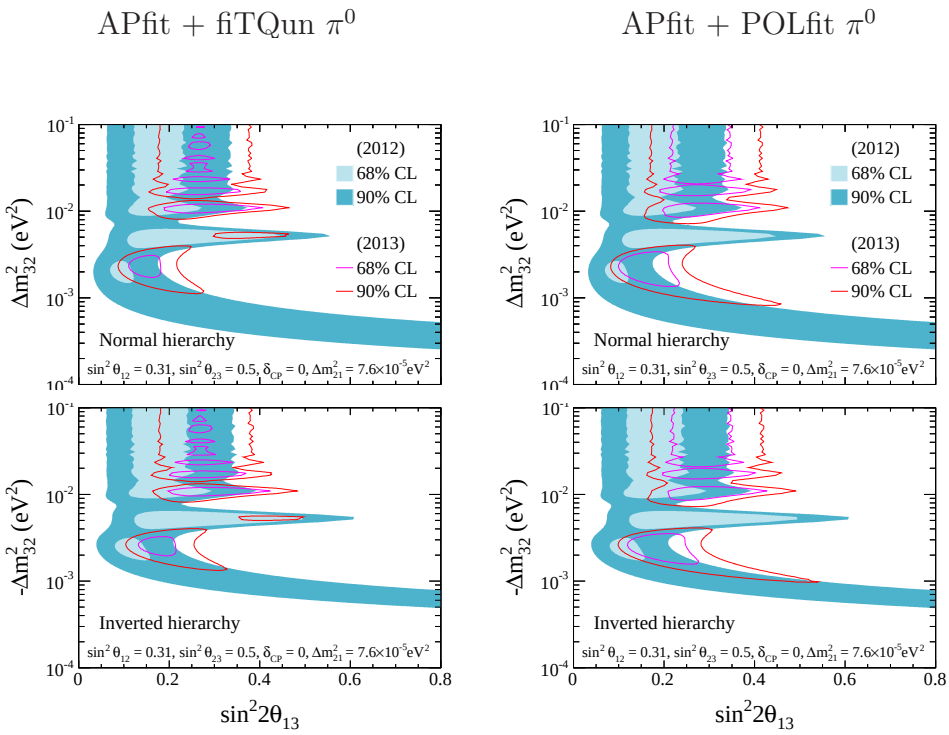

Figure 9.13: The 68 % and 90 % C.L. regions for $\sin^2 2\theta_{13}$ and Δm^2_{32} measured by the Run1+2+3b+3c+4 data (red lines) compared with the 2012a result in blue regions. The fit assumes $\delta_{\rm CP} = 0$ and normal mass hierarchy (top) or inverted mass hierarchy (bottom) for APfit + fiTQun π^0 case (left) and APfit + POLfit π^0 case (right). The regions are determined by a global scan in the two-dimensional plane.

9.3 Fit results of θ_{13} for various θ_{23}

Because the best fit value of θ_{13} in T2K Run1-4 shows a large value compared to reactor experiments, an effect of the fixed values of θ_{23} is evaluated as well as δ_{CP}. Figure 9.14 shows the best fit and the 68 % and 90 % C.L. regions of $\sin^2\theta_{13}$ for each value of $\sin^2\theta_{23}$ in APfit + fiTQun π^0 case measured by the Run1+2+3b+3c+4 data. The top part shows normal mass hierarchy while the bottom assumes inverted mass hierarchy. Here, δ_{CP} is fixed to zero.

Figures 9.15 and 9.16 show the best fit and 68 % C.L. regions of $\sin^2 2\theta_{13}$ for each value of δ_{CP} by a certain $\sin^2\theta_{23}$ measured by the Run1+2+3b+3c+4 data fit for APfit+fiTQun π^0, respectively. In other sections, $\sin^2\theta_{23}$ is fixed to 0.5 ($\sin^2 2\theta_{23} = 1$).

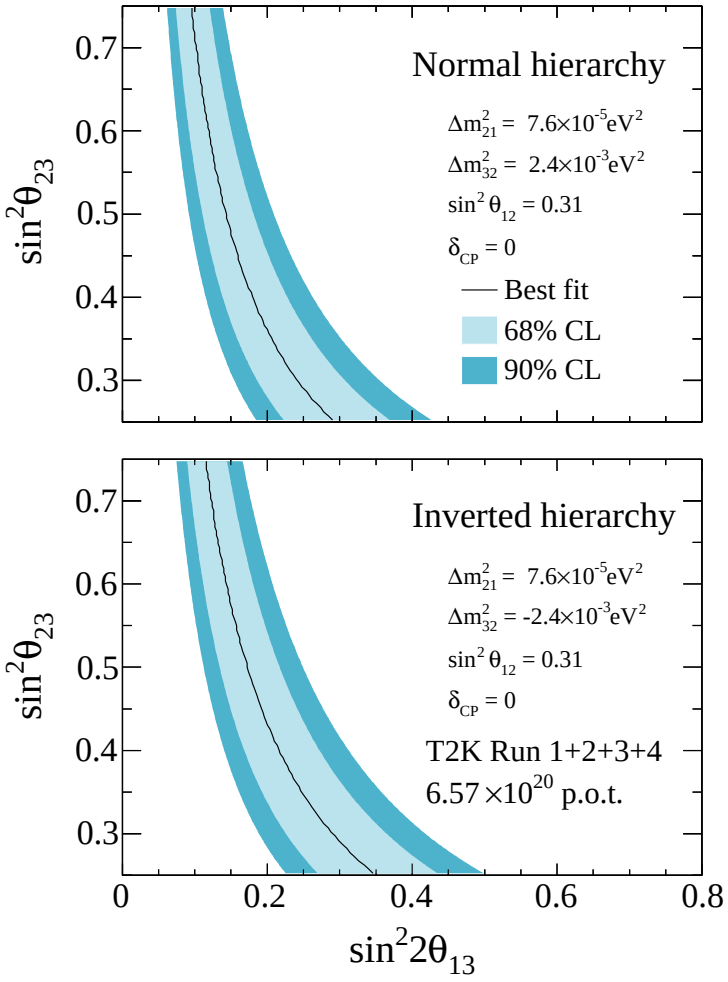

Figure 9.14: (APfit + fiTQun π^0) The 68 % and 90 % C.L. regions for $\sin^2 2\theta_{13}$ for each value of $\sin^2 \theta_{23}$ measured by the Run1+2+3b+3c+4 data fit assuming normal mass hierarchy (top) or inverted mass hierarchy (bottom). The value of $\sin^2 \theta_{23}$ is fixed to 0.5 ($\sin^2 2\theta_{23} = 1$) in other sections.

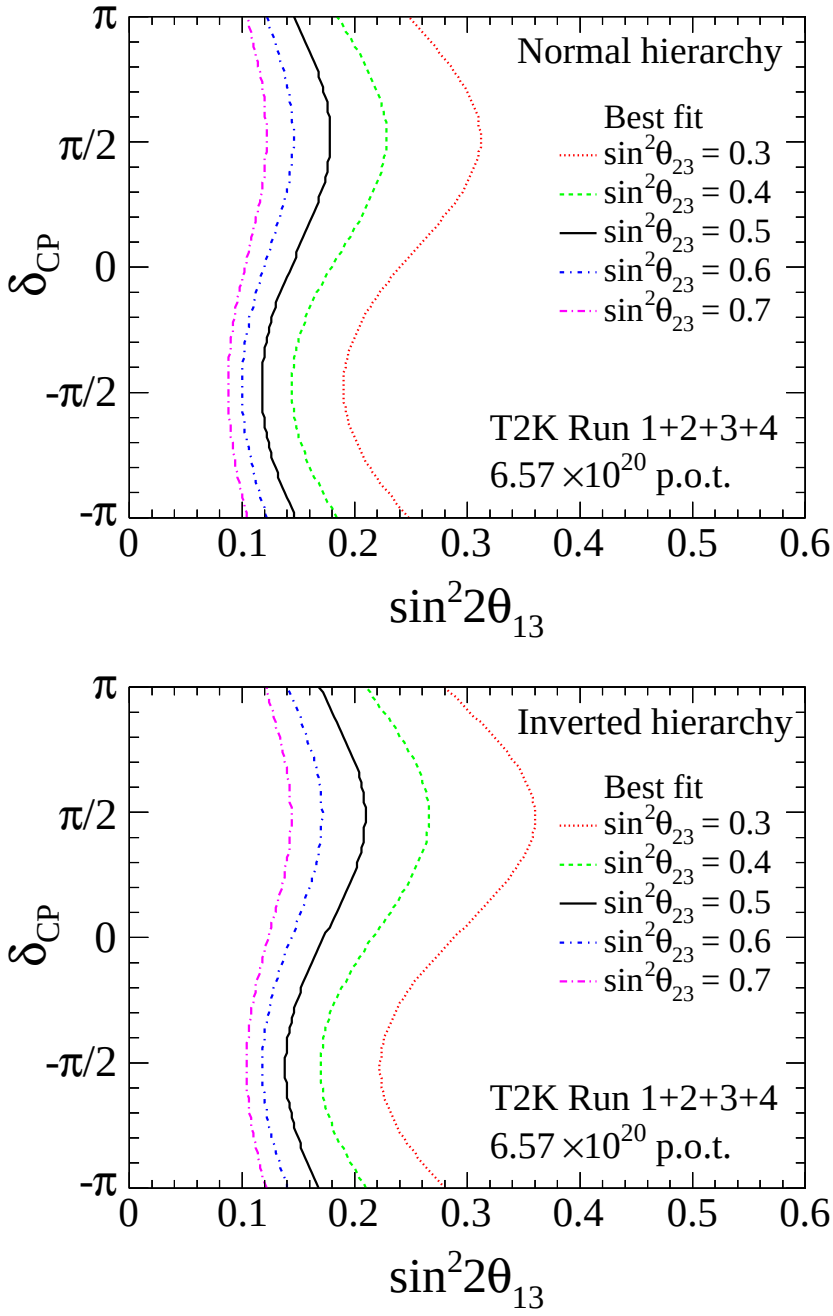

Figure 9.15: (APfit + fiTQun π^0) The best-fit line of $\sin^2 2\theta_{13}$ for each value of $\delta_{\rm CP}$ by the Run1+2+3b+3c+4 data fit, where $\sin^2\theta_{23}$ is varied from 0.3 to 0.7 ($\sin^2\theta_{23} = 0.5$ in default). Normal mass hierarchy is assumed in the top figure and inverted mass hierarchy in bottom.

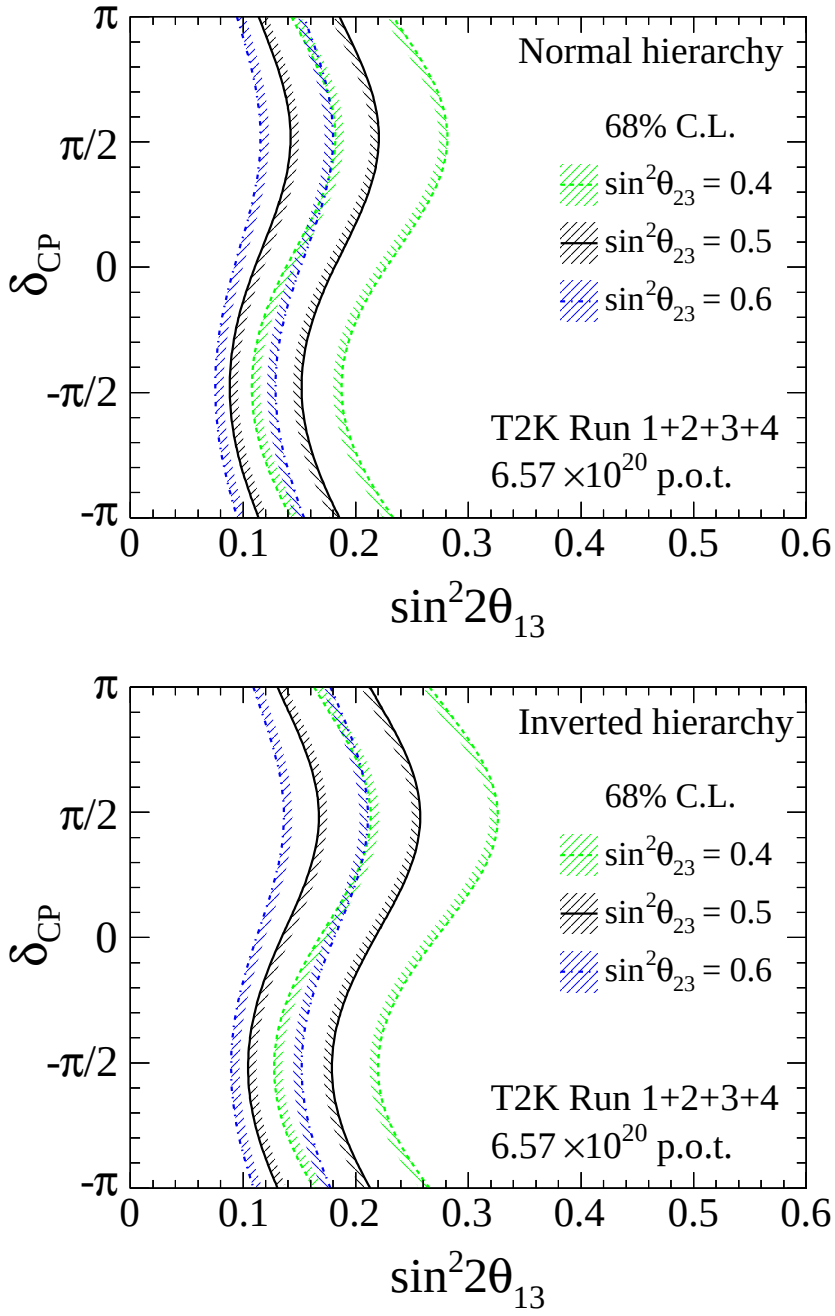

Figure 9.16: (APfit + fiTQun π^0) The 68 % C.L. regions of $\sin^2 2\theta_{13}$ for each value of δ_{CP} drawn between two lines by the Run1+2+3b+3c data fit, where $\sin^2\theta_{23}$ is varied from 0.4 to 0.6 ($\sin^2\theta_{23} = 0.5$ in default). Normal mass hierarchy is assumed in the top figure and inverted mass hierarchy in bottom.

Chapter 10

Constraints on δ_{CP}

As seen in Section 9.3, our dependence on $\sin^2\theta_{23}$ can clearly be seen. Because of this, it was decided to marginalize over the parameters we are least sensitive to: $\sin^2\theta_{23}$ and Δm^2_{32}. We can also marginalize over $\sin^2 2\theta_{13}$ using the more accurate results on θ_{13} from the reactor experiments. This section discusses the method used for marginalization and the results from doing so.

10.1 Method

For marginalization, we add in an extra likelihood term to equation 5.2 to give us a new likelihood defined as:

$$\mathcal{L}(N_{obs}, \boldsymbol{E}^{rec}_{obs}; \boldsymbol{\theta}, \boldsymbol{f}, \boldsymbol{\theta_o}) = \mathcal{L}_{norm}(N_{obs}; \boldsymbol{\theta}, \boldsymbol{f}) \times \mathcal{L}_{shape}(\boldsymbol{E}^{rec}_{obs}; \boldsymbol{\theta}, \boldsymbol{f}) \times \mathcal{L}_{syst}(\boldsymbol{f}) \times \mathcal{L}_{const}(\boldsymbol{\theta_o}), \tag{10.1}$$

where the new term θ_o represents the parameters we are constraining and $\mathcal{L}_{const}$ is the likelihood of the external constraints. All other terms are the same as described in Section 5.

When marginalizing over $\sin^2\theta_{23}$ and Δm^2_{32}, the T2K Run1-3 ν_μ disappearance results are used. Figure 10.1 shows the $-2\Delta\ln\mathcal{L}$ map of Δm^2_{32} vs $\sin^2\theta_{23}$ that is used to calculate $\mathcal{L}_{const}$. This makes the extra likelihood term:

$$\mathcal{L}(\boldsymbol{\theta_o}) = e^{\frac{\chi^2(\sin^2\theta_{23}, \Delta m^2_{32})}{-2}} \tag{10.2}$$

where $\chi^2(\sin^2\theta_{23}, \Delta m^2_{32})$ is the χ^2 value from the map at point $\sin^2\theta_{23}$ and Δm^2_{32}. At the moment, the correlation of systematic errors between the ν_μ disappearance and ν_e appearance are ignored. This is done because the effects of the systematic error correlation is negligibly small compared to the statistical error in this analysis.

To further constrain our results and see possible sensitivity to δ_{cp}, we can also marginalize over $\sin^2 2\theta_{13}$. We have chosen to use the 2012 PDG best fit results to all reactor experiments for this where $\sin^2 2\theta_{13} = 0.098 \pm 0.013$ [12]. This makes the total $\mathcal{L}_{const}$:

$$\mathcal{L}(\boldsymbol{\theta_o}) = e^{\frac{\chi^2(\sin^2\theta_{23}, \Delta m^2_{32})}{-2}} \times e^{\frac{(\sin^2 2\theta_{13} - 0.098)^2}{-2\times 0.013^2}} \tag{10.3}$$

where the first term is the same as in Equation 10.2 and the second term is a simple Gaussian with a mean of 0.098 and a standard deviation of 0.013.

For fitting, this analysis is using a profiling method for marginalization over a numerical integration method. This choice was natural for us as the systematic terms are also profiled. Please be aware that this is different from what the ν_e appearance group does, as they integrate over both their systematics and constraint terms to get rid of the nuisance parameters, and those were the official results published in [2].

In practice, the profiling of our constraint terms is done in a two-step procedure. First, for every oscillation point we are interested in fitting, we calculate the total likelihood for it and all constraint terms. Then, we scan

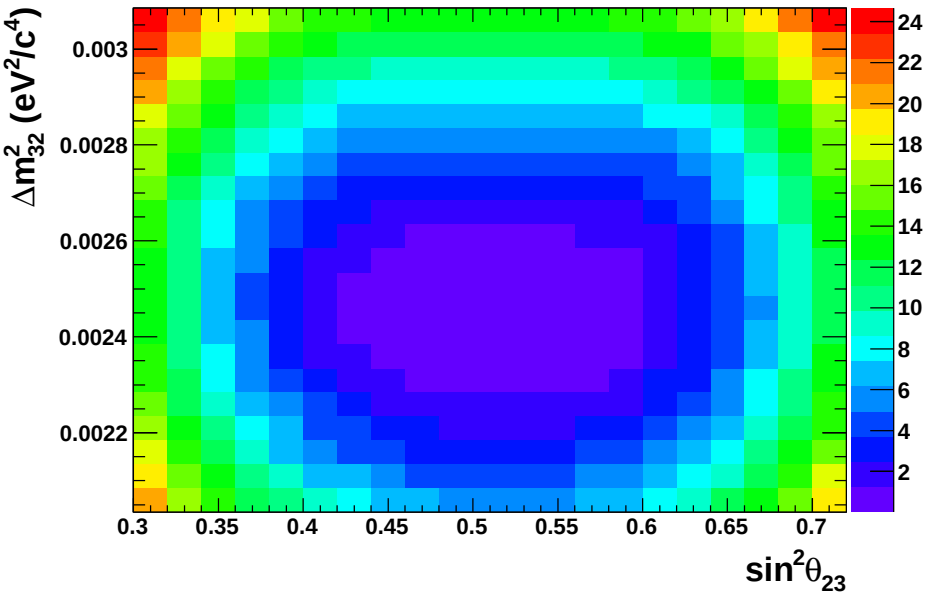

Figure 10.1: The $-2\Delta \ln \mathcal{L}$ map of Δm^2_{32} vs $\sin^2\theta_{23}$ from the T2K Run1-3 ν_μ disappearance results. This map is used to calculate the $\mathcal{L}_{const}$ term when marginalizing over $\sin^2\theta_{23}$ and Δm^2_{32}.

Table 10.1: The best fit points and confidence intervals for the sensitivity curves shown in Figure 10.2. For the truth information, $\sin^2 2\theta_{13} = 0.1$, $\delta_{cp} = 0$ and 6.57×10^{20} POT are assumed with all other oscillation parameters set to nominal. Sensitivity is taken as the $\sqrt{-2\Delta ln(\mathcal{L})}$ at $\sin^2 2\theta_{13} = 0.0$

	$\sin^2\theta_{23}$ and Δm^2_{32} Fixed		$\sin^2\theta_{23}$ and Δm^2_{32} Constrained	
Hierarchy	Normal	Inverted	Normal	Inverted
Best fit	0.100	0.100	0.100	0.100
68 % C.L.	0.073 - 0.133	0.071 - 0.136	0.070 - 0.136	0.067 - 0.139
90 % C.L.	0.058 - 0.157	0.054 - 0.162	0.055 - 0.166	0.051 - 0.170
Sensitivity (σ)	5.62	4.85	5.61	4.87

over the constraint terms and pick the one that maximizes the likelihood of our oscillation point. This procedure of stopping on a single oscillation point and then scanning over all the constraint terms is repeated for every fitted oscillation point. The grid size used for this procedure can change for the fitted parameters depending on the plot being produced, however the grid for constraining $\sin^2\theta_{23}$ and Δm^2_{32} is fixed to that shown in Figure 10.1.

10.2 Results with Constraint on $\sin^2\theta_{23}$ and Δm^2_{32}

A sensitivity study on $\sin^2\theta_{13} = 0.1$ with and without Equation 10.2 added to the likelihood was performed over many toy experiments. For this study, except when explicitly noted, all other oscillation parameters are held to their nominal value as shown in Table 5.1. Figure 10.2 shows the results from this study, with the figure on the left (right) showing the NH (IH) case. The black curves correspond to $sin^2\theta_{23}$ and Δm^2_{32} marginalized and is averaged over 500 toy experiments. The red curves correspond to $sin^2\theta_{23}$ and Δm^2_{32} fixed to their nominal values and is averaged over 4000 toy experiments. Due to the increase in processing time needed for marginalization, we were only able to run over 500 toy experiments when marginalization was added. Table 10.1 summarizes the results and clearly shows the contours of $\sin^2 2\theta_{13}$ are wider when marginalization is used due to the extra uncertainty from $sin^2\theta_{23}$ and Δm^2_{32}. However, marginalization has little to no effect on the best-fit point and the overall sensitivity to $\sin^2 2\theta_{13} = 0.0$ is virtually unchanged.

The fit to Run1-4 data (6.57×10^{20} POT) with and without marginalization

Table 10.2: The best fit points and confidence intervals for the fit to the Run1-4 data (6.57×10^{20} POT) in Figure 10.3. For these plots $\delta_{cp} = 0$ and all other oscillation parameters set to nominal. Sensitivity is taken as the $\sqrt{-2\Delta ln(\mathcal{L})}$ at $\sin^2 2\theta_{13} = 0.0$

	$\sin^2\theta_{23}$ and Δm^2_{32} Fixed		$\sin^2\theta_{23}$ and Δm^2_{32} Constrained	
Hierarchy	Normal	Inverted	Normal	Inverted
Best fit	0.144	0.172	0.140	0.168
68 % C.L.	0.110 - 0.181	0.134 - 0.217	0.102 - 0.187	0.121 - 0.222
90 % C.L.	0.092 - 0.209	0.112 - 0.249	0.083 - 0.223	0.100 - 0.264
Sensitivity (σ)	7.22	7.21	7.22	7.22

can be seen in Figure 10.3 and the results are summarized in Table 10.2. The left (right) hand side of Figure 10.3 shows the NH (IH) results with $\delta_{cp} = 0$. The black curves correspond to $\sin^2\theta_{23}$ and Δm^2_{32} marginalized while the red curves show the results with $\sin^2\theta_{23}$ and Δm^2_{32} fixed. Figure 10.4 shows the 1D scans in $\sin^2 2\theta_{13}$ for all values of δ_{cp} with $\sin^2\theta_{23}$ and Δm^2_{32} marginalized. The left (right) side show the fit for NH (IH). The dotted lines show the best fit points, while the green (blue) show the 68% (90%) CL. After adding in the constraints on $\sin^2\theta_{23}$ and Δm^2_{32}, the contours widen as expected. It also causes the best fit points to become smaller while the sensitivity at $\sin^2 2\theta_{13} = 0.0$ stays the same.

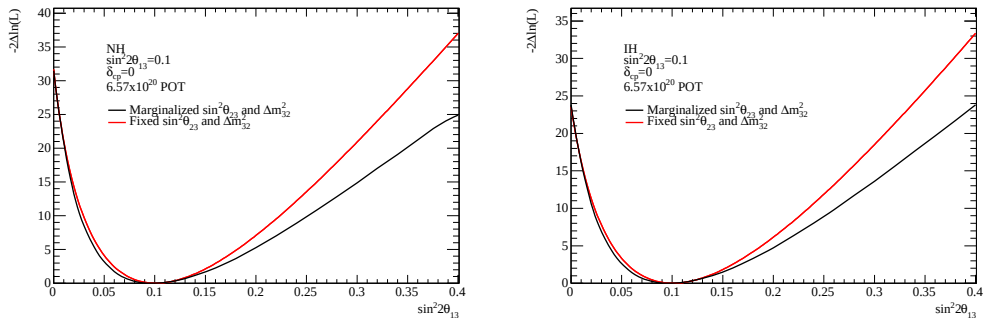

Figure 10.2: The sensitivity curves averaged over many MC toys for $\sin^2 2\theta_{13} = 0.1$ with $\sin^2\theta_{23}$ and Δm^2_{32} constrained (500 toys, black) and with no constraint (4000 toys, red), for NH (left) and IH (right). Here, $\delta_{cp} = 0$ and 6.57×10^{20} POT are assumed with all other oscillation parameters set to nominal.

10.3 Results with Reactor Constraints

To obtain our sensitivity to δ_{cp} and possibly the mass hierarchy, we now include the reactor constraint along with our constraints on $\sin^2\theta_{23}$ and Δm^2_{32} as described in Equation 10.3. Figure 10.5 shows the results to our fit with the

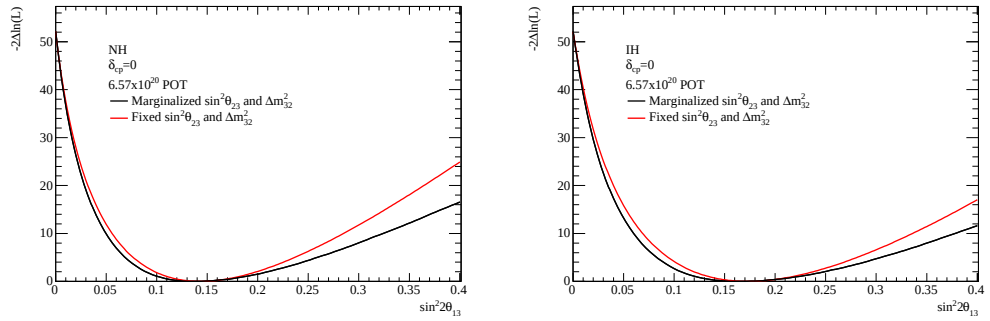

Figure 10.3: The sensitivity curves for Run1-4 data (6.57×10^{20} POT) with $\sin^2\theta_{23}$ and Δm^2_{32} constrained (black) and with no constraint (red), for NH (left) and IH (right). Here, $\delta_{cp} = 0$ and all other oscillation parameters are set to their nominal values.

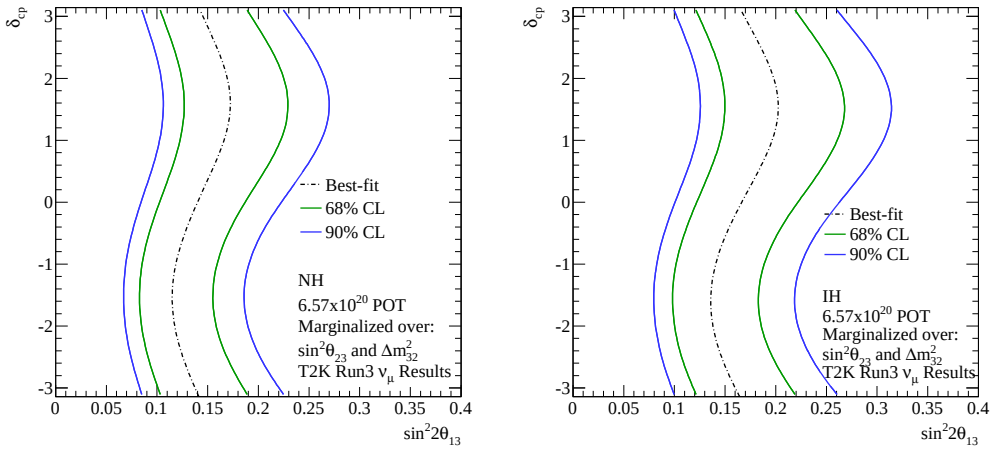

Figure 10.4: The 1D scans of $\sin^2\theta_{13}$ for all values in δ_{cp} of the Run1-4 data with 6.57×10^{20} POT. Here $\sin^2\theta_{23}$ and Δm^2_{32} are both constrained. The left (right) side show the fit for NH (IH). The dotted lines show the best fit points, while the green (blue) show the 68% (90%) CL.

Table 10.3: The 68% and 90% exclusion regions of δ_{cp} after constraints on $\sin^2\theta_{23}$, Δm^2_{32} and $\sin^2 2\theta_{13}$ are applied according to Equation 10.3. These numbers are based off of Figure 10.5.

	$\sin^2\theta_{23}$, Δm^2_{32} and $\sin^2 2\theta_{13}$ Constrained	
Hierarchy	Normal	Inverted
90 % C.L. Exclusion	$0.17\pi \sim 0.86\pi$	$-\pi \sim -0.91, -0.10\pi \sim \pi$

Run1-4 data (6.57×10^{20} POT) for NH (IH) in black (red). This figure shows the results where the local minimum in NH and IH are taken separately, that is to say that the minimum $-2\Delta ln(\mathcal{L})$ for both is set to 0. This is used to calculate our 68% and 90% exclusion region in δ_{cp}. These exclusion regions are summarized in Table 10.3 and uses the Feldman-Cousins method for the calculations [29]. As can be seen, with all the constraints added, we show a slight preference for normal mass hierarchy. Also, about a third of δ_{cp} is excluded at the 90% CL for the IH case.

To check the consistency of these results, a sensitivity study was also completed on δ_{cp}. For this, the truth point was set at $\delta_{cp} = -\pi/2$ and $\sin^2 2\theta_{13} = 0.1$, with all other values set to nominal. These values where chosen as $\delta_{cp} = -\pi/2$ is our best fit in both NH and IH, while $\sin^2 2\theta_{13} = 0.1$ is very close to the reactor best fit. Figure 10.6 shows the results of this study. The $-2\Delta ln(\mathcal{L})$ curve is averaged over 500 toy experiments, and has a best fit point at -1.57 radians. The maximum $-2\Delta ln(\mathcal{L})$ value for NH and IH occurs at 1.57 radians and the NH case has a value of 1.83. The maximum $-2\Delta ln(\mathcal{L})$ value for the data was at 2.53. To see how likely this higher $-2\Delta ln(\mathcal{L})$ value in the data is, a projection of all toy experiments at $\delta_{cp} = \pi/2$ is made and the integral for all values above 2.53 is taken. This showed 38.9% of all the toy experiments had a value at or higher than 2.53 in $-2\Delta ln(\mathcal{L})$ and is shown in Figure 10.7.

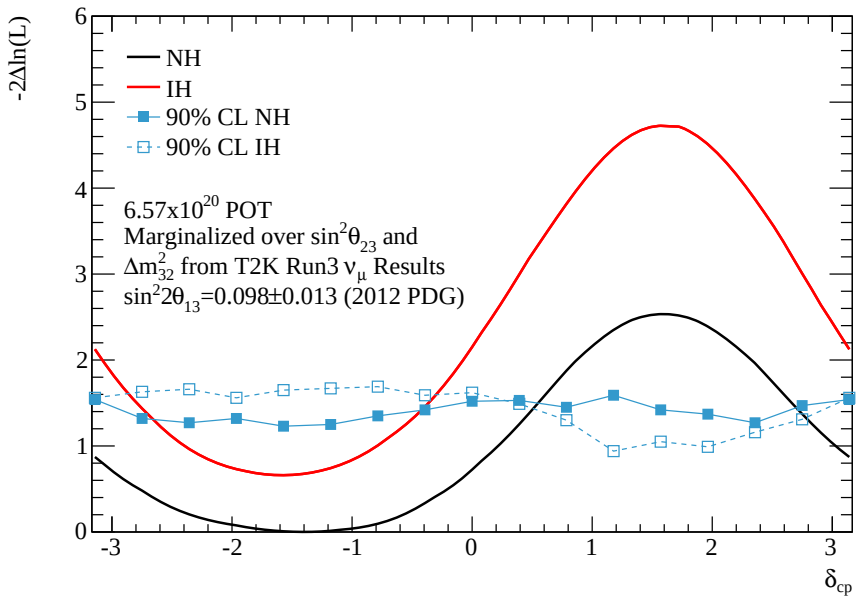

Figure 10.5: The $-2\Delta ln(\mathcal{L})$ curves of δ_{cp} for the Run1-4 data (6.57×10^{20} POT) constrained over $\sin^2\theta_{23}$, Δm^2_{32}, and $\sin^2 2\theta_{13}$ as described in Equation 10.3. The black line shows the NH fit while the red shows the IH. The figure shows the fit when the local minima is taken and is used to extract the 90% exclusion regions with the Feldman-Cousins method. Here, the solid blue squares are the 90% CL assuming the NH case and the hollow blue squared are the 90% CL assuming IH.

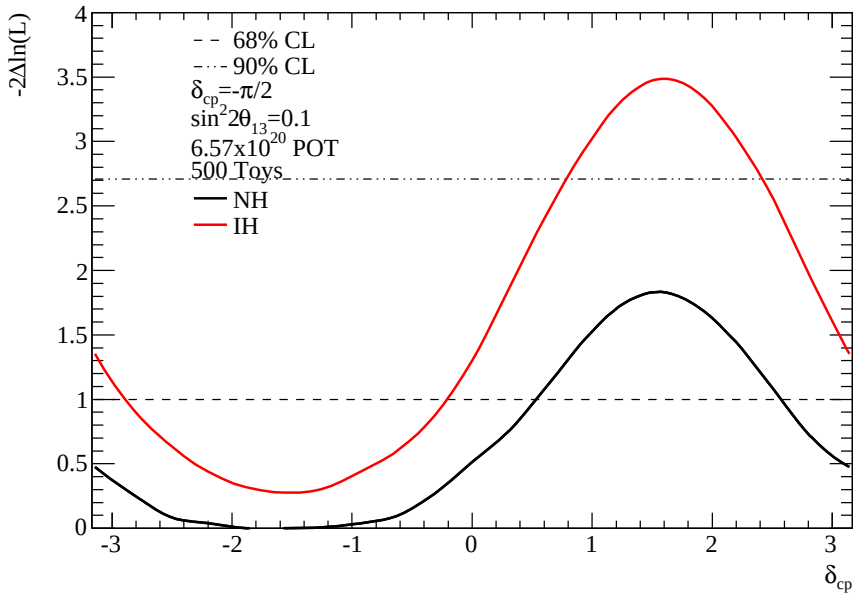

Figure 10.6: The $-2\Delta ln(\mathcal{L})$ curves of δ_{cp} averaged over 500 toy experiments and constrained by $\sin^2\theta_{23}$, Δm^2_{32}, and $\sin^2 2\theta_{13}$ as described in Equation 10.3. Using 6.57×10^{20} POT, a truth point of $\delta_{cp} = -\pi/2$ and $\sin^2 2\theta_{13} = 0.1$ is set, with all other oscillation parameters at their nominal values. The best fit value in δ_{cp} occurs at -1.57 radians for both NH and IH with a maximum $-2\Delta ln(\mathcal{L})$ value of 1.83 found at 1.57 radians for NH.

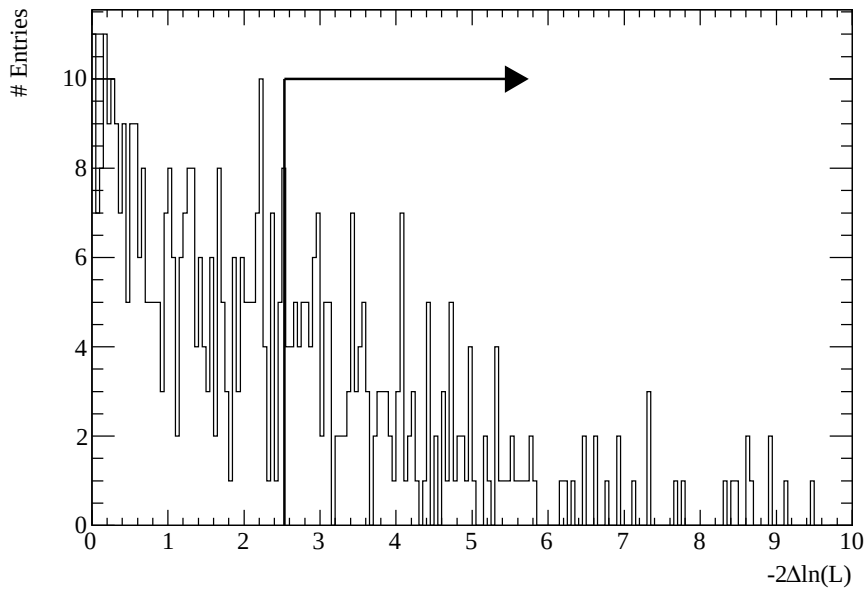

Figure 10.7: The projection of $-2\Delta ln(\mathcal{L})$ values at $\delta_{cp} = \pi/2$ for all NH toy experiments used in Figure 10.6. The vertical line corresponds to 2.53 in $-2\Delta ln(\mathcal{L})$, the maximum $-2\Delta ln(\mathcal{L})$ from the data. The integral over all points greater than 2.53, shown by the arrow, shows 38.9% of all toy experiments had a value at or greater than that of the data.

Chapter 11

Summary

An update of the ν_e appearance analysis using E^{rec} shape was performed with a new Super-K reconstruction alogrithm (fiTQun) for the π^0 rejection and new error estimates of BANFF and Super-K detector uncertainties. The quantity of data increased substantially from 3.01×10^{20} POT to 6.57×10^{20} POT in Run1+2+3b+3c+4 (until 8^{th} of May, 2013). As a primary analysis, ν_e candidates are selected by fiTQun π^0 cut instead of the POLfit π^0 cut used in 2012a and both of the two data sets are analyzed and shown in this dissertation. This analysis uses an extended maximum likelihood fit to the reconstructed neutrino energy distributions of the observed ν_e candidate events. The ND280 data is used to constrain the flux and some cross section systematic parameters. The cross section uncertainties are more closely parameterized to better predict the energy spectrum.

Validation checks show that the analysis can provide a reliable result on the ν_e appearance search for both fiTQun π^0 and POLfit π^0 cut in 2013a. The primary analysis method using the fiTQun π^0 cut was determined by a sensitivity study before analyzing data. Under the $\theta_{13} = 0$ hypothesis, the probability for observing 28 or more ν_e candidate events is 5.2×10^{-13}, equivalent to a $7.2\,\sigma$ significance. For $\delta_{\rm CP} = 0$, $|\Delta m^2_{32}| = 2.4 \times 10^{-3}{\rm eV}^2$ and normal (inverted) mass hierarchy, a confidence interval at 90 % C.L. is $0.092 < \sin^2 2\theta_{13} < 0.209$ ($0.112 < \sin^2 2\theta_{13} < 0.249$). Under the same assumptions, the best fit values with 1σ errors are $\sin^2 2\theta_{13} = 0.144^{+0.037}_{-0.034}$ for normal hierarchy and $\sin^2 2\theta_{13} = 0.172^{+0.045}_{-0.038}$ for inverted hierarchy. If we use the much stronger world average of θ_{13} along with the T2K ν_μ disappearance results, values for δ_{CP} from 0.17π $\sim 0.86\pi$ ($-\pi \sim -0.91, -0.10\pi \sim \pi$) can be excluded at the 90% CL for normal (inverted) hierarchy.

Bibliography

[1] K. Abe *et al.* [T2K Collaboration], Phys. Rev. D 88, 032002 (2013), "Evidence of Electron Neutrino Appearance in a Muon Neutrino Beam"

[2] K. Abe *et al.* [T2K Collaboration], Phys. Rev. Lett. 112, 061802, (2014) "Observation of Electron Neutrino Appearance in a Muon Neutrino Beam"

[3] L. Brown, Physics Today 31(9) (1978), "The idea of the neutrino"

[4] F. Reines and C. L. Cowan, Phys. Rev., 92 (1953), "Detection of the free neutrino"

[5] C. L. Cowan, F. Reines, F. B. Harrison, H. W. Kruse, and A. D. McGuire, Science, 124 (1956), "Detection of the free neutrino: a confirmation"

[6] R. Davis and D. Harmer, Bull. Am. Phys. Soc., 4 (1959), "Attempt to observe the ^{36}Cl(ν,e^-)^{37}Ar reaction induced by reactor antineutrinos"

[7] B. Pontecorvo, Chalk River Report PD-205, (1946)

[8] Y. Fukuda, *et al.* [T2K Collaboration], Phys. Rev. Lett. 81 (1998), "Evidence for oscillation of atmospheric neutrinos"

[9] Q. R. Ahmed, *et al.* [SNO Collaboration], Phys. Rev. Lett. 89 (2002), "Direct evidence for neutrino flavor transformation from neutral current interactions in the Sudbury Neutrino Observatory"

[10] L. Wolfenstein, Phys. Rev. D 17 (1978), "Neutrino oscillations in matter"

[11] I. Taylor, T2K Dissertation, "Development of T2K 280m Near Detector Software for Muon and Photon Reconstruction"

[12] J. Beringer *et al.*, (Particle Data Group), Phys. Rev. D 86, 010001 (2012), "Review of Particle Physics"

[13] Y. Itow *et al.*, hep-ex/0106019 (2001), "The JHF-Kamioka neutrino project"

[14] K. Abe *et al.* [T2K Collaboration], Nucl. Instrum. Meth. A **659**, 106 (2011) "The T2K Experiment"

[15] D. Beavis *et al.*, Physics Design Report, BNL 52459, (1995) "Long Baseline Neutrino Oscillation Experiment at the AGS (Proposal E889)"

[16] A. Pla-Dalmau *et al.*, Nucl. Instrum. Meth. A **466**, (2001) "Low-cost extruded plastic scintillator"

[17] D. Renker and E. Lerenz, JINST 4 (2009), P04004 "Advances in solid state photon detectors"

[18] M. Yokoyama, Nucl. Instrum. Meth. A **610**, (2009) "Application of Hamamatsu MPPC to T2K neutrino detectors"

[19] S. Assylbekov *et al.*, Nucl. Instrum. Meth. A **686**, (2012) "The T2K ND280 Off-Axis Pi-Zero Detector"

[20] G. Charpak, J Derre, Y. Giomataris, P. Rebourgeard Nucl. Instrum. Meth. A **478**, (2002) "MICROMEGA, a mutlipurpose gaseous detector"

[21] S. Fukuda *et al.* [Super-Kamiokande Collaboration], Nucl. Instrum. Meth. A **501**, (2003) "The Super-Kamiokande detector"

[22] Y. Ashie *et al.* [Super-Kamiokande Collaboration] Phys. Rev. D 71 112005, (2005) "A measurement of atmospheric neutrino oscillation paramters by Super-Kamiokande I"

[23] M. Shiozawa, Nucl. Instrum. Meth. A **433**, (1999) "Reconstruction algorithms in the Super-Kamiokande large water Cherenkov detector"

[24] E. R. Davies. "Maching Vision: Theory, Algorithms, Practicalities" Morgan Kaufmann Publishers Inc., San Francisco, CA, USA, 2004

[25] L. Michel. *Proc. Phys. Soc.*, A63 (1950) "Interaction between four half spin particles and the decay of the mu meason"

[26] P. Hanggi *et al.*, Nucl. Phys. Lett. B 51 (1974) 119. "Muon decay in orbit"

[27] M. Yamada *et al.* [Kamiokande Collaboration] Phys. Rev. D 44, (1991) "Measurement of the charge ratio and polarization of 1.2 TeV/x cosmic-ray muons with the Kamiokande II detector"

[28] J. Beringer *et al.*, (Particle Data Group), Phys. Rev. D 86, 010001 (2012), "Passage of particles through matter"

[29] G. Feldman and R. Cousins, Phys. Rev. D57, 3873, (1998) "A Unified Approach to the Classical Statistical Analysis of Small Signals"

[30] G.L. Fogli *et al.*, Phys. Rev. D 84, 053007 (2011), "Evidence of $\theta_{13} > 0$ from global neutrino data analysis"

[31] (T2K-TN-109), "ν_e appearance analysis with maximum likelihood fit to neutrino energy spectrum"

[32] (T2K-TN-114), "Electron neutrino appearance analysis with electron momentum and angle distribution"

[33] (T2K-TN-115), "Updated ν_e appearance analysis with the Feldman-Cousins method"

[34] G. L. Fogli1, E. Lisi, A. Marrone, D. Montanino, A. Palazzo, and A. M. Rotunno1, Phys. Rev. D 86, 013012 (2012), "Global analysis of neutrino masses, mixings, and phases: Entering the era of leptonic CP violation searches"

[35] Prob3++, http://www.phy.duke.edu/~raw22/public/Prob3++/

[36] (T2K-TN-106), "Constraining the Flux and Cross Section Models with Data from the ND280 Detector for 2012a Oscillation Analysis"

[37] (T2K-TN-166), "ND280 Flux and Cross Section Constraint for 2013"

[38] (T2K-TN-099), "Flux Inputs for the 2012a Oscillation Analysis"

[39] (T2K-TN-108), "Cross section parameters for the 2012a oscillation analysis"

[40] A. A. Aguilar-Arevalo *et al.* [MiniBooBE Collaboration], Phys. Lett. B, 664, (2008) "First Observation of Coherent π^0 Production in Neutrino-nucleus Interactions with E$_\nu$¡2 GeV"

[41] (T2K-TN-156), "SK π^0 systematic errors for 2013 oscillation analysis"

[42] (T2K-TN-157), "Super-K systematic uncertainty for the ν_e analysis with T2K 6.393×10^{20} POT (RUN1-4) data"

[43] H. A. Tanaka, Photonuclear interactions, http://www.t2k.org/asg/oagroup/meeting/20120301/photonuke/.

Appendix A

Fake Data Sets

After the fit validation check and sensitivity studies are finished, fake data fits are performed as a rehearsal of the real data fit and also for a preparation of scripts to make figures and tables for the final results. The fake data includes four true oscillation parameter sets (set D, set E, set F, and set G), which are secret from the oscillation analyzers. Additionally, there are fake data sets made for two different beam exposures (6.4×10^{20} and 8.5×10^{20} POT) Therefore a total of 8 fake data sets are tested. The truth information that created these fake data sets are listed in Table A.1.

Figures A.1, A.3, A.5, and A.7 show the $-2\Delta \ln \mathcal{L}$ curve, the observed E^{rec} distribution, and the predicted spectrum at the best fit point obtained by the fake data fits of set D, E, F, and G respectively. These figures are fitted assuming NH. Figures A.2, A.4, A.6, and A.8 show the same data sets but assumed IH instead.

For easy comparison, the results of both the E^{rec} and $p-\theta$ at $6.4{\times}10^{20}$ POT are shown in Table A.2 (Table A.3) and at $8.5{\times}10^{20}$ POT in Table A.4

Table A.1: Truth information to generate the fake data samples.

Parameter	Set D	Set E	Set F	Set G
$\Delta m^2_{21}\text{eV}^2$	7.6×10^{-5}	7.6×10^{-5}	7.6×10^{-5}	7.6×10^{-5}
$\Delta m^{32}\text{eV}^2$	-2.5×10^{-3}	2.5×10^{-3}	-2.7×10^{-3}	2.4×10^{-3}
$\sin^2\theta_{12}$	0.35	0.32	0.32	0.32
$\sin^2\theta_{23}$	0.42	0.62	0.5	0.5
$\sin^2\theta_{13}$	0.018	0.039	0.01	0.0251
$\sin^2 2\theta_{13}$	0.0707	0.15	0.0396	0.098
δ_{cp} radians	$-\frac{\pi}{2}$	0.0	π	0.0

(Table A.5) for normal (inverted) mass hierarchy

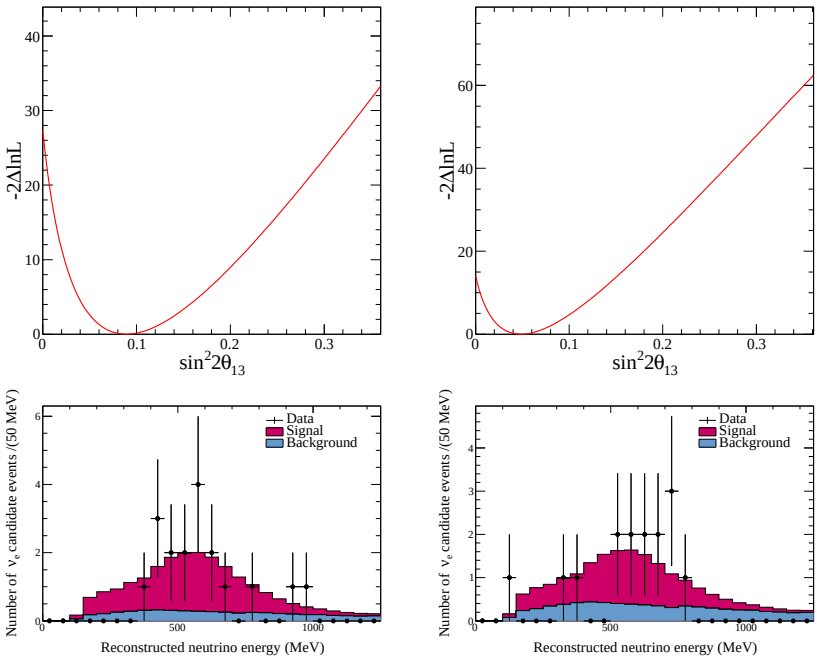

Figure A.1: The $-2\Delta \ln \mathcal{L}$ curve (top), the observed E^{rec} distribution (black dots), and the predicted spectrum at the best fit point (filled, red for signal and blue for background) for the 6.4×10^{20} (left) and 8.5×10^{20} (right) fake data in set D, assuming $\delta_{\rm CP} = 0$, $|\Delta m^2_{32}| = 2.4 \times 10^{-3}{\rm eV}^2$, and normal mass hierarchy.

Table A.2: Summary of the best fit, 68 % and 90 % C.L. allowed ranges of $\sin^2 2\theta_{13}$ for both the E^{rec} and $p-\theta$ fake data results from the fake data set, assuming assuming 6.4×10^{20} POT, $\delta_{\rm CP} = 0$, $|\Delta m^2_{32}| = 2.4 \times 10^{-3}\text{eV}^2$, and normal mass hierarchy. The final column shows the true $\sin^2 2\theta_{13}$ value. Please refer to Table A.1 for the other truth parameters.

6.4×10^{20} POT, Normal hierarchy

set		E^{rec}	$p-\theta$	true $\sin^2 2\theta_{13}$
set D	best-fit	0.090	0.090	0.071
	68 % C.L.	$0.063-0.120$	$0.063-0.121$	
	90 % C.L.	$0.049-0.143$	$0.048-0.145$	
set E	best-fit	0.190	0.174	0.150
	68 % C.L.	$0.152-0.235$	$0.139-0.216$	
	90 % C.L.	$0.130-0.267$	$0.118-0.247$	
set F	best-fit	0.024	0.026	0.040
	68 % C.L.	$0.009-0.045$	$0.010-0.046$	
	90 % C.L.	$0.002-0.061$	$0.002-0.062$	
set G	best-fit	0.144	0.140	0.098
	68 % C.L.	$0.111-0.183$	$0.107-0.178$	
	90 % C.L.	$0.092-0.211$	$0.089-0.206$	

Table A.3: Summary of the best fit, 68 % and 90 % C.L. allowed ranges of $\sin^2 2\theta_{13}$ for both the E^{rec} and $p-\theta$ fake data results assuming 6.4×10^{20} POT, $\delta_{\rm CP} = 0$, $|\Delta m^2_{32}| = 2.4 \times 10^{-3}{\rm eV}^2$, and inverted mass hierarchy. The final column shows the true $\sin^2 2\theta_{13}$ value. Please refer to Table A.1 for the other truth parameters.

6.4×10^{20} POT, Inverted hierarchy

set		E^{rec}	$p-\theta$	true $\sin^2 2\theta_{13}$
set D	best-fit	0.106	0.110	0.071
	68 % C.L.	$0.076-0.143$	$0.077-0.147$	
	90 % C.L.	$0.059-0.170$	$0.060-0.175$	
set E	best-fit	0.228	0.210	0.150
	68 % C.L.	$0.183-0.279$	$0.168-0.259$	
	90 % C.L.	$0.157-0.315$	$0.144-0.294$	
set F	best-fit	0.030	0.032	0.040
	68 % C.L.	$0.011-0.055$	$0.012-0.057$	
	90 % C.L.	< 0.075	$0.002-0.077$	
set G	best-fit	0.176	0.170	0.098
	68 % C.L.	$0.136-0.221$	$0.132-0.216$	
	90 % C.L.	$0.113-0.253$	$0.110-0.249$	

Table A.4: Summary of the best fit, 68 % and 90 % C.L. allowed ranges of $\sin^2 2\theta_{13}$ for both the E^{rec} and $p-\theta$ fake data results from the fake data set, assuming assuming 8.5×10^{20} POT, $\delta_{\rm CP} = 0$, $|\Delta m^2_{32}| = 2.4 \times 10^{-3}{\rm eV}^2$, and normal mass hierarchy. The final column shows the true $\sin^2 2\theta_{13}$ value. Please refer to Table A.1 for the other truth parameters.

8.5×10^{20} POT, Normal hierarchy

set		E^{rec}	$p-\theta$	true $\sin^2 2\theta_{13}$
set D	best-fit	0.048	0.048	0.071
	68 % C.L.	$0.031-0.070$	$0.031-0.069$	
	90 % C.L.	$0.022-0.086$	$0.022-0.085$	
set E	best-fit	0.138	0.138	0.150
	68 % C.L.	$0.109-0.171$	$0.110-0.171$	
	90 % C.L.	$0.093-0.196$	$0.093-0.195$	
set F	best-fit	0.044	0.052	0.040
	68 % C.L.	$0.026-0.066$	$0.033-0.074$	
	90 % C.L.	$0.016-0.082$	$0.023-0.091$	
set G	best-fit	0.094	0.098	0.098
	68 % C.L.	$0.069-0.122$	$0.074-0.128$	
	90 % C.L.	$0.056-0.142$	$0.060-0.149$	

Table A.5: Summary of the best fit, 68 % and 90 % C.L. allowed ranges of $\sin^2 2\theta_{13}$ for both the E^{rec} and $p-\theta$ fake data results assuming 6.4×10^{20} POT, $\delta_{\rm CP} = 0$, $|\Delta m^2_{32}| = 2.4 \times 10^{-3}{\rm eV}^2$, and inverted mass hierarchy. The final column shows the true $\sin^2 2\theta_{13}$ value. Please refer to Table A.1 for the other truth parameters.

8.5×10^{20} POT, Inverted hierarchy

set		E^{rec}	$p-\theta$	true $\sin^2 2\theta_{13}$
set D	best-fit	0.060	0.060	0.071
	68 % C.L.	$0.039-0.086$	$0.040-0.086$	
	90 % C.L.	$0.028-0.105$	$0.029-0.105$	
set E	best-fit	0.168	0.170	0.150
	68 % C.L.	$0.134-0.207$	$0.135-0.208$	
	90 % C.L.	$0.114-0.235$	$0.116-0.236$	
set F	best-fit	0.054	0.064	0.040
	68 % C.L.	$0.032-0.081$	$0.041-0.091$	
	90 % C.L.	$0.020-0.101$	$0.028-0.111$	
set G	best-fit	0.114	0.122	0.098
	68 % C.L.	$0.085-0.147$	$0.092-0.156$	
	90 % C.L.	$0.069-0.172$	$0.075-0.181$	

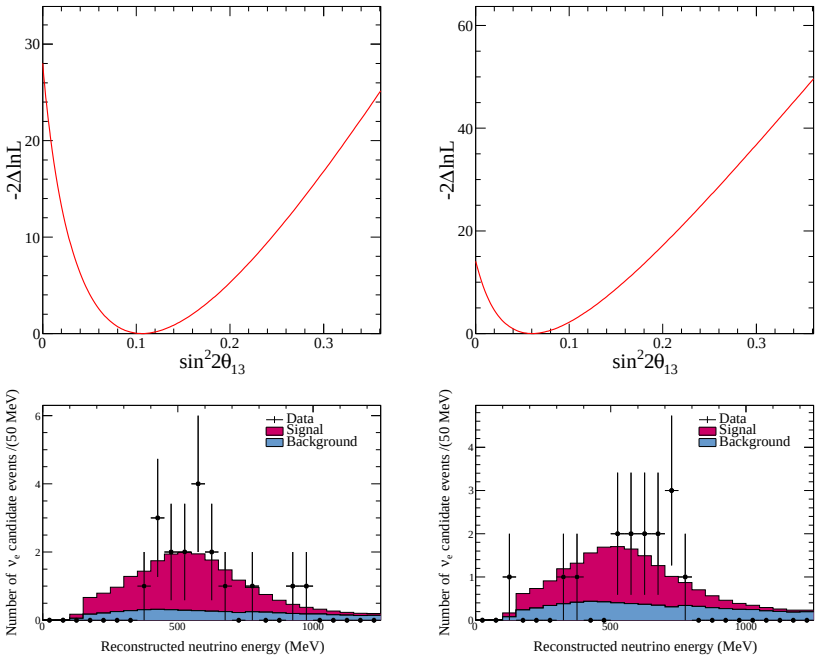

Figure A.2: The $-2\Delta \ln \mathcal{L}$ curve (top), the observed E^{rec} distribution (black dots), and the predicted spectrum at the best fit point (filled, red for signal and blue for background) for the 6.4×10^{20} (left) and 8.5×10^{20} (right) fake data in set D, assuming $\delta_{\rm CP} = 0$, $|\Delta m^2_{32}| = 2.4 \times 10^{-3}{\rm eV}^2$, and inverted mass hierarchy.

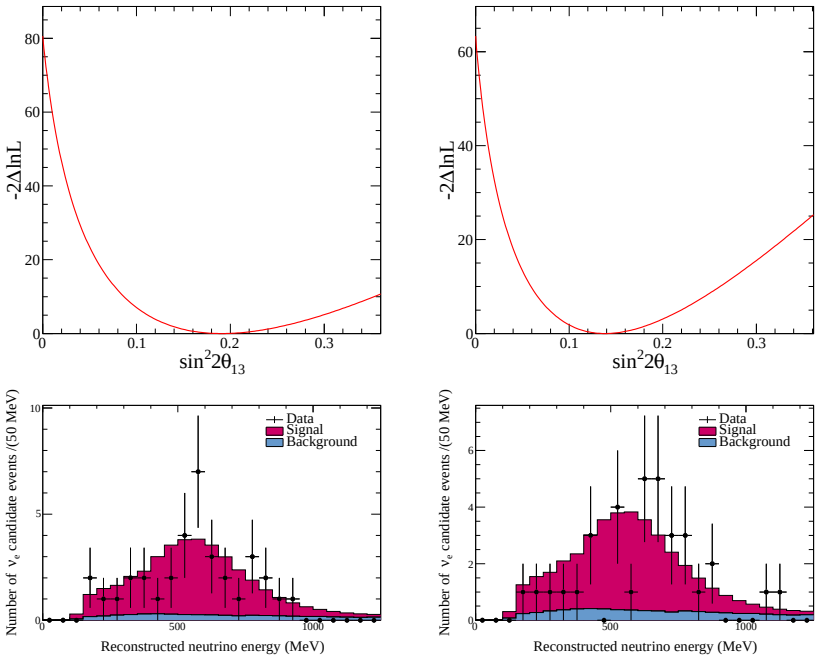

Figure A.3: The $-2\Delta \ln \mathcal{L}$ curve (top), the observed E^{rec} distribution (black dots), and the predicted spectrum at the best fit point (filled, red for signal and blue for background) for the 6.4×10^{20} (left) and 8.5×10^{20} (right) fake data in set E, assuming $\delta_{\rm CP} = 0$, $|\Delta m^2_{32}| = 2.4 \times 10^{-3}{\rm eV}^2$, and normal mass hierarchy.

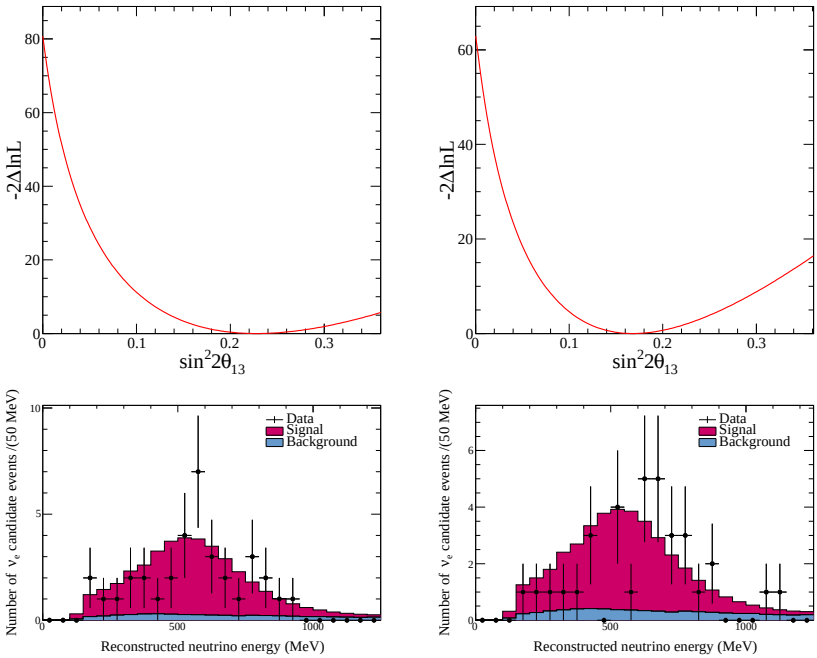

Figure A.4: The $-2\Delta \ln \mathcal{L}$ curve (top), the observed E^{rec} distribution (black dots), and the predicted spectrum at the best fit point (filled, red for signal and blue for background) for the 6.4×10^{20} (left) and 8.5×10^{20} (right) fake data in set E, assuming $\delta_{\rm CP} = 0$, $|\Delta m^2_{32}| = 2.4 \times 10^{-3}{\rm eV}^2$, and inverted mass hierarchy.

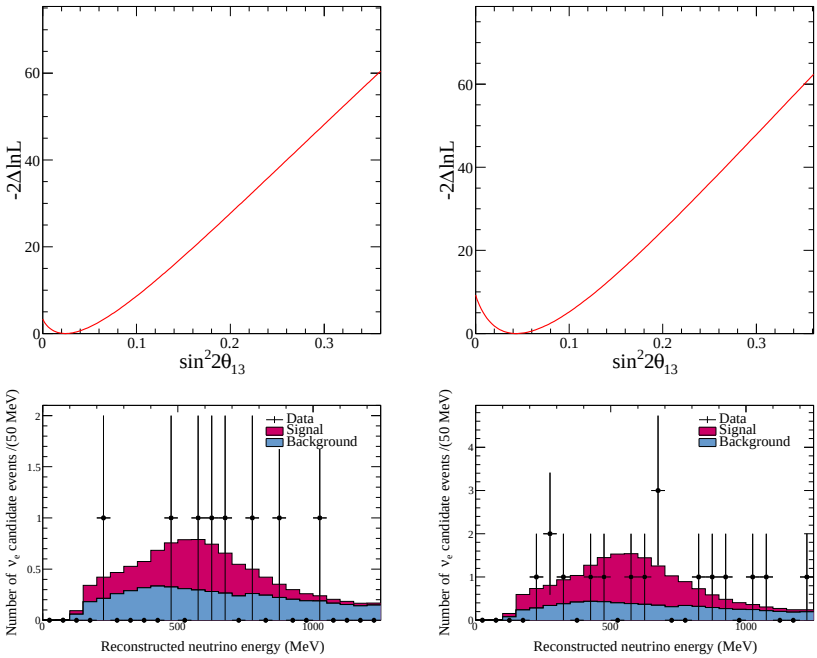

Figure A.5: The $-2\Delta \ln \mathcal{L}$ curve (top), the observed E^{rec} distribution (black dots), and the predicted spectrum at the best fit point (filled, red for signal and blue for background) for the 6.4×10^{20} (left) and 8.5×10^{20} (right) fake data in set F, assuming $\delta_{\rm CP} = 0$, $|\Delta m^2_{32}| = 2.4 \times 10^{-3}{\rm eV}^2$, and normal mass hierarchy.

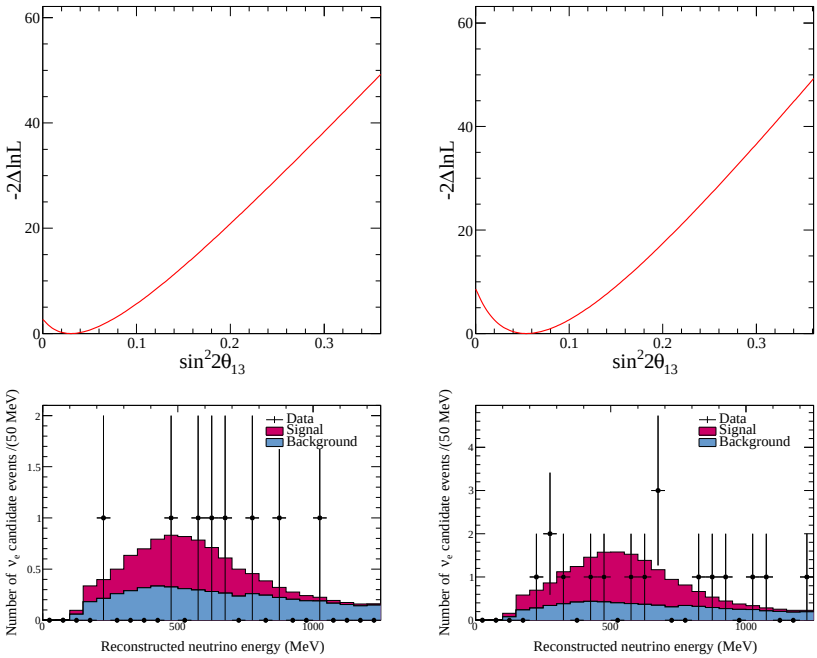

Figure A.6: The $-2\Delta \ln \mathcal{L}$ curve (top), the observed E^{rec} distribution (black dots), and the predicted spectrum at the best fit point (filled, red for signal and blue for background) for the 6.4×10^{20} (left) and 8.5×10^{20} (right) fake data in set F, assuming $\delta_{\rm CP} = 0$, $|\Delta m^2_{32}| = 2.4 \times 10^{-3}{\rm eV}^2$, and inverted mass hierarchy.

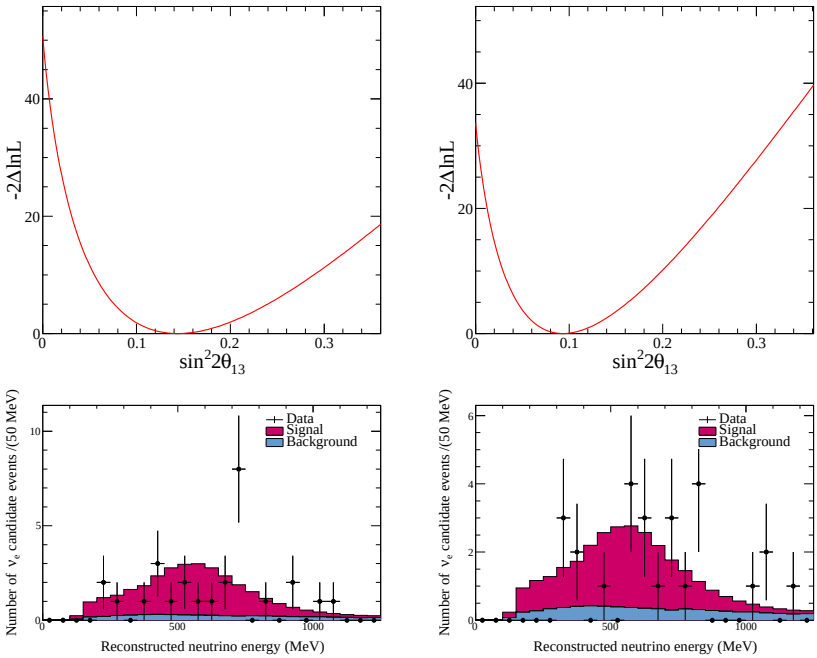

Figure A.7: The $-2\Delta \ln \mathcal{L}$ curve (top), the observed E^{rec} distribution (black dots), and the predicted spectrum at the best fit point (filled, red for signal and blue for background) for the 6.4×10^{20} (left) and 8.5×10^{20} (right) fake data in set G, assuming $\delta_{\rm CP} = 0$, $|\Delta m^2_{32}| = 2.4 \times 10^{-3}{\rm eV}^2$, and normal mass hierarchy.

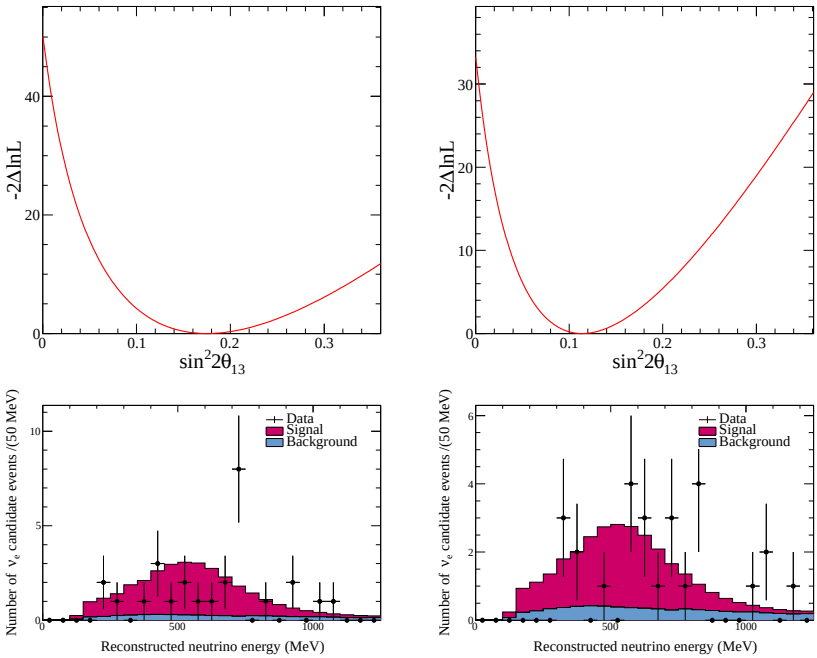

Figure A.8: The $-2\Delta \ln \mathcal{L}$ curve (top), the observed E^{rec} distribution (black dots), and the predicted spectrum at the best fit point (filled, red for signal and blue for background) for the 6.4×10^{20} (left) and 8.5×10^{20} (right) fake data in set G, assuming $\delta_{\rm CP} = 0$, $|\Delta m^2_{32}| = 2.4 \times 10^{-3}{\rm eV}^2$, and inverted mass hierarchy.